

**Local Earthquake Tomography of Central America:
Structural Variations and Fluid Transport in the
Nicaragua-Costa Rica Subduction Zone**

Dissertation
zur Erlangung des Doktorgrades
der Mathematischen-Naturwissenschaftlichen Fakultät
der Christian-Albrechts-Universität zu Kiel

vorgelegt von

Aysun Nilay Dinc

Kiel, 2008

Referent:

Koreferent:

Tag der mündlichen Prüfung:

Zum Druck genehmigt:

Prof. Dr. Wolfgang Rabbel

Prof. Dr. Ernst Flüh

24. April 2008

Kiel, den 24. April 2008

Der Dekan

Contents

ABSTRACT	5
ZUSAMMENFASSUNG	7
1 Introduction	9
2 Geology and Tectonic Settings	13
2.1 Central Costa Rica	15
2.2 Southern Nicaragua / Northern Costa Rica	16
3 Method	19
3.1 Introduction	19
3.2 Inversion for Vp and Vs	20
3.3 Inversion for Vp and Vp/Vs	23
3.4 Inversion for P-wave Anisotropy	24
4 Central Costa Rica	29
4.1 Introduction	29
4.2 Data Base	30
4.3 Resolution Tests	33
4.3.1 Test with a random selection of events	34
4.3.2 Tests with synthetic data	35
4.4 Results of Tomographic Inversion	38
4.4.1 Seismicity	40

4.4.2	Seismic velocity model	42
4.5	Discussion and Conclusion	45
4.5.1	The seismogenic zone and slab geometry	45
4.5.2	Lateral change in the slab geometry	46
4.5.3	Evidence of fluid transport	47
4.5.4	Costa Rica Deformation Belt	50
5	Southern Nicaragua/Northern Costa Rica	51
5.1	Introduction	51
5.2	Data Base	52
5.3	Resolution Tests	56
5.3.1	Test with random selection of events	56
5.3.2	Tests with synthetic data	56
5.4	Results of Tomographic Inversion	59
5.5	Discussion and Conclusion	61
5.5.1	Effect of overriding plate on the system	61
5.5.2	Geophysical evidences of mantle wedge hydration	65
5.5.3	Fluid source for the hydrated mantle wedge	66
6	P-wave Anisotropy	69
6.1	Introduction	69
6.2	Data Base and Method of Interpretation	73
6.3	Results	81
6.4	Discussion and Conclusion	84
7	Conclusions	87
	Acknowledgement	89
	Bibliography	91
	List of Figures	101

List of Tables	105
A Station Lists	107
A.1 QUEPOS Station List	107
A.2 JACO Station List	109
A.3 RSN Station List	111
A.4 TOMO Station List	112
Curriculum Vitae	115

ABSTRACT

The Central American convergent margin is characterized by pronounced lateral changes from north to south such as a decreasing dip of the slab, a decreasing magma production and a shift in the volcanic front. To investigate this transition in terms of seismicity and tectonics, a joint on- and offshore local earthquake tomography and P-wave anisotropy studies were performed in central Costa Rica and in S Nicaragua/N Costa Rica respectively.

In central Costa Rica, seismic travel time data sets of three on- and off-shore seismic networks were combined for a simultaneous inversion of hypocenter locations, 3-D structure of P-wave velocity and V_p/V_s ratio. The tomographic inversion was performed using about 2000 high quality events. The seismicity and slab geometry as well as V_p and V_p/V_s show significant lateral variation along the subduction zone corresponding to the changes of the incoming plate which consists of serpentized oceanic lithosphere in the NW, a seamount province in the center and the subducting Coscos Ridge in the SE of the investigation area. Three prominent features can be identified in the V_p and V_p/V_s tomograms: a high velocity zone with a perturbation of 4-10 % representing the subducting slab, a low velocity zone (10-20 %) in the forearc probably caused by deformation, fluid release and hydration, and a low-velocity zone below the volcanic arc related to upwelling fluids and magma. Unlike previously suggested, the dip of the subducting slab does not decrease to the south. Instead, an average steepening of the plate interface from 30° to 45° is observed from north to south and a transition from a plane to a stair-shape plate interface. This is connected with a change in the deformation style of the overriding plate where roughly planar, partly conjugated, clusters of seismicity of regionally varying dip are observed. It could be shown that the Costa Rica Deformation Belt represents a deep crustal transition zone extending from the surface down to 40 km depth. This transition zone indicates the lateral termination of the active part of the volcanic chain and seems to be connected with the changing structure of the incoming plate as well.

In S Nicaragua/N Costa Rica, the same inversion procedure was performed using 860

events. The analysis shows low S-wave velocities (~ 4 km/s), high V_p/V_s ratios (~ 2.0) and an aseismic gap in the upper mantle along the Sandino Basin. These findings are interpreted as an indication of mantle wedge hydration. The existence of a hydrated forearc upper-mantle wedge in southern Nicaragua and the absence of it in northern Costa Rica is important to understand the variations in the tectonic structures along the margin and provides an improved view of the deep dehydration process in subduction zones. The sharp transition between the Nicaraguan and northern Costa Rican margins is explained by the dominating extensional forces in the southern Nicaraguan overriding plate.

In addition to the velocity inversion, a P-wave anisotropy study was performed to have a better understanding in the mantle dynamics and tectonics of the Earth's interior. P-wave anisotropy results show two main structures: 1) Trench-perpendicular seismically fast directions in the incoming plate which can be explained either by the initial mineral orientation at the mid-oceanic ridge or by the deformation parallel to the subduction direction. 2) Trench-parallel seismically fast directions and abrupt rotations to trench-parallel anisotropy in the forearc which support the mantle escape towards to northwest. These patterns of seismic anisotropy may be caused by the olivine fabric transition from A-type to B-type or three dimensional flow associated with along-strike variations in slab geometry.

ZUSAMMENFASSUNG

Der aktive Kontinentalrand von Mittelamerika ist im Bereich von Nicaragua und Costa Rica von Nord nach Süd durch signifikante laterale Änderungen charakterisiert, zum Beispiel durch eine Abnahme des Abtauchwinkels der subduzierten Platte, eine abnehmende Magmenproduktion und einen Versatz in der vulkanischen Front. Um diesen Übergang seismologisch und tektonisch zu untersuchen, wurden in Zentral-Costa Rica und in Süd-Nicaragua/Nord-Costa Rica tomographische Messungen mit lokalen Erdbeben vor der Küste und an Land durchgeführt. Dabei wurden Ausbreitungsgeschwindigkeiten von P- und S-Wellen sowie die Anisotropie der P-Wellengeschwindigkeit studiert.

In Zentral-Costa Rica wurden Datensätze seismischer Laufzeiten von drei am Meeresboden bzw. an Land installierten seismischen Netzwerken kombiniert für eine gemeinsame Inversion zur Bestimmung der Hypozentren und der 3D-Struktur der P-Wellengeschwindigkeit und des V_p/V_s -Verhältnisses. Die tomographische Inversion beruht auf gut identifizierbaren Einsätzen von 2000 lokalen Erdbeben. Die Seismizitätsverteilung, die Geometrie der Plattengrenze ebenso wie V_p und V_p/V_s weisen signifikante laterale Variationen entlang der Subduktionszone auf, die mit Änderungen der hereinkommenden ozeanischen Platte korrespondieren. Im Nordwesten des Untersuchungsgebietes besteht die ozeanische Platte aus serpentinierter ozeanischer Lithosphäre, in Zentrum aus einer Seamount-Provinz und im Südosten aus dem ebenfalls subduzierenden Cocos-Rücken. In den V_p - und V_p/V_s -Tomogrammen können drei Besonderheiten beobachtet werden: Eine Zone erhöhter Geschwindigkeiten (4-10 %), die die subduzierte Platte repräsentiert, eine Zone erniedrigter Geschwindigkeit (10-20 %) im Fore-Arc-Bereich, wahrscheinlich verursacht durch Deformation, Entwässerung bzw. Hydratisierung, und eine Zone erniedrigter Geschwindigkeiten unter dem Vulkanbogen, bedingt durch aufsteigende Fluide und Magma. Im Gegensatz zu früheren Vorstellungen nimmt der Neigungswinkel der Plattengrenze nicht von Nord nach Süd ab. Stattdessen werden eine mittlere Verteilung von 30° auf 45° beobachtet und ein Übergang von einer ebenen zu einer stufenartigen Form der Plattengrenze. Dies ist verbunden mit einem Wechsel im Deformationsstil der überlagernden Platte, in der näherungsweise planare, teilweise konjugierte Seismizitäts-Cluster unterschiedlichen Einfallswinkels beobachtet werden. Es konnte gezeigt werden, dass der sog. Costa Rica Deformation Belt eine tief in die Kruste

reichende Übergangszone darstellt, die von der Erdoberfläche bis ca. 40 km Tiefe reicht. Diese Übergangszone stellt zugleich die laterale Begrenzung des heute aktiven Teils der vulkanischen Kette dar und korrespondiert auch mit einem Wechsel in der Struktur der ozeanischen Platte.

In Süd-Nicaragua / Nord-Costa Rica wurde dasselbe tomographische Inversionsverfahren auf 860 Lokalbeben angewandt. Die Tomogramme zeigen großräumige Anomalien erniedrigter S-Wellen-Geschwindigkeiten, erhöhte V_p/V_s -Verhältnisse und eine aseismische Lücke im oberen Mantel entlang des Sandino-Beckens, die als Anzeichen für eine Hydratisierung des Mantelkeils gewertet wird. Die Existenz eines hydratisierten Mantelkeils in Süd-Nicaragua und das Fehlen der Hydratisierung in Nord-Costa Rica stellt einen wichtigen Hinweis für das Verständnis der Variation der tektonischen Strukturen entlang des Kontinentalrandes dar und liefert einen verbesserten Blick auf den tiefen Entwässerung an Subduktionszonen. Der scharfe Übergang zwischen den Kontinentalrändern von Nicaragua und Nord-Costa Rica kann durch die dominierende Extension der überlagernden Platte in Süd-Nicaragua erklärt werden.

Zusätzlich zur seismischen Geschwindigkeitsinversion wurde eine Studie zur P-Wellen-Anisotropie durchgeführt, um das Verständnis der Manteldynamik zu verbessern. Die Ergebnisse zur P-Wellen-Anisotropie zeigen, dass die horizontalen Achsen hoher P-Wellengeschwindigkeit im Bereich der subduzierten Platte senkrecht zum Tiefsee graben ausgerichtet sind. Dies kann durch eine initiale Mineralausrichtung am mittelozeanischen Rücken oder auch durch Deformation parallel zur Subduktionsrichtung erklärt werden. Die Anisotropie zeigt weiterhin, dass die horizontalen Achsen hoher P-Wellengeschwindigkeit im Bereich des Fore-Arc parallel zum Tiefsee graben ausgerichtet sind, wobei der Übergang abrupt erfolgt. Dieses Muster kann einerseits durch das Fließen von Mantelmaterial in nordwestlicher Richtung gedeutet werden, andererseits lässt es sich jedoch auch durch den Übergang vom A- zum B-Typ der Mineralausrichtung in Peridotiten oder durch dreidimensionale Fließgeometrien erklären.

Chapter 1

Introduction

Central America is tectonically characterized by the subduction of the Cocos Plate beneath the Caribbean plate along the Middle America Trench (MAT). It shows strong lateral variations at relatively short distances regarding the structure of the incoming plate, overriding plate, seismicity and arc volcanism. Considering these aspects, Central America is an excellent site to study the subduction zone processes. Therefore, the collaborative research center SFB 574 has been focused on Central America, mainly Costa Rica and Nicaragua in two phases from 2001-2008. The aim of the project is to investigate the flow of volatiles and fluids into and out of a subduction system which have a major influence on the long- and short-term development of the Earth's climate, the geochemical evolution of the hydrosphere and atmosphere, and the causes of natural disasters. The SFB 574 pursues an integrated investigation of the fluxes and effects of fluids from the incoming plate through the forearc and the volcanic arc back into the hydrosphere and atmosphere (Fig. 1.1).

The Central America subduction zone is being investigated by a seismological research subproject of the SFB 574 conducted by Costa Rican and German partners. It intends to constitute the structural and seismotectonical framework of these investigations. Since 2002, several seismological network installations had already been accomplished (Fig.1.2). Three temporary amphibious seismological networks, named JACO (April 2002 to October 2002), QUEPOS (September 2002 to May 2003) (Chapter 4) and TOMO (December 2005 to June 2006) (Chapter 5) were deployed along the Pacific coast of central Costa Rican and S Nicaraguan/N Costa Rican margins, respectively. The P-wave and S-wave arrival time of the earthquakes recorded by these networks were used to perform simultaneous inversion of earthquake location, origin time, V_p , V_p/V_s , station corrections and P-wave anisotropy. By these seismic properties, I aimed to get detailed and reliable seismic images of the geologic structures at the Central America Subduction Zone and evidences for the underlying processes. Understanding the composition and phys-

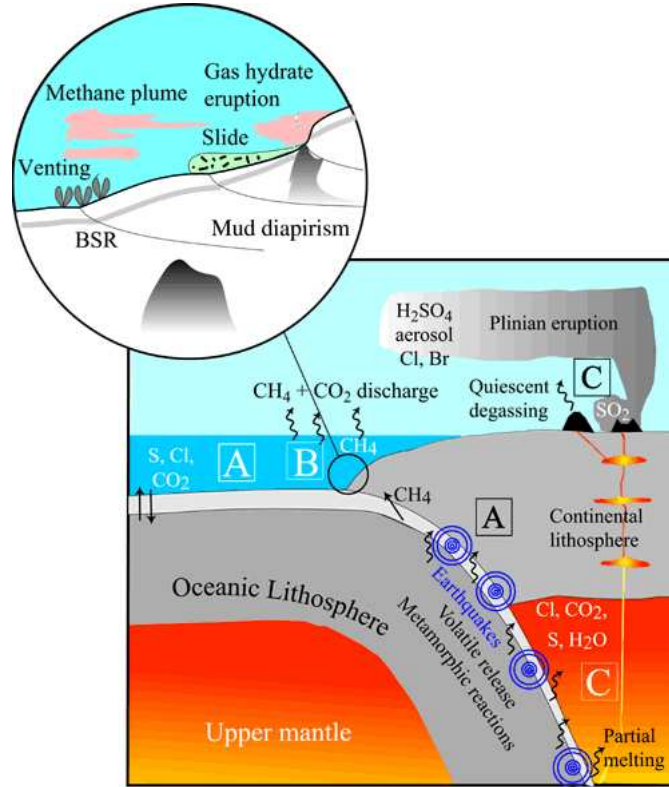


Figure 1.1: Material transport and transformation in subduction zones: Long- and short-term trends of the Earth's climate, geochemical evolution of the exosphere, and the causes of certain natural hazards are related to the reactions of volatiles and fluids in subduction zones. Partial return flux is through dewatering at the deformation front of accretionary complexes, through mud diapirism (incl. gas hydrates formation and destabilization; enlarged inset), and through volcanic arc magmas. The process of volatile return encompasses different material reservoirs, transport loops, and reactions for H₂O and the S-, C-, and Cl-compounds.

ical states of the materials and the dynamics of the tectonic features will have further importance in accurate seismic hazard assessment.

The thesis is organized as follows:

Chapter 2 summarizes the relevant geological and geophysical background information from central Costa Rica and S Nicaragua/N Costa Rica. In order to understand seismogenesis and velocity information along the subduction zone it is necessary to define incoming and overriding plate characteristics (composition, bathymetry, thermal history), mechanical processes occurring prior to seismogenesis and the chemistry of materials transported through the subduction system.

Chapter 3 provides the basic steps of the inversion algorithms. The 3D seismic velocity structure, hypocenter locations and station corrections are calculated iteratively and simultaneously by using the LOTOS (Local TOMography Software) of Koulakov et al.

(2007). The inherent matrix inversion was performed by an iterative least squares method (Paige and Saunders, 1982; Van der Sluis and van der Vorst, 1987). The underlying ray tracing is based on the bending method (Um and Thurber, 1987). In addition to isotropic inversion, P-wave anisotropy is calculated by the ANITA algorithm (ANIsotropic Tomography Algorithm) which is an iterative non-linear inversion of local earthquake data in orthorhombic anisotropic media with one predefined vertical orientation.

Chapter 4 focuses on the results of the simultaneous isotropic inversion of V_p , V_p/V_s and hypocenters in central Costa Rica by merging three data sets from independently recorded networks. Therefore, special attention is paid to the resolution in the overlapping areas. Resolution tests confirm the reliability of the results. The seismogenic zone and slab geometry of central Costa Rica show a significant transition from seamount province to Cocos Ridge province. This transition corresponds with the central Costa Rica Deforming Belt (CCRDB). In addition, I found evidence of mantle wedge hydration in the northern part of the region. It is assumed that the fluid input into the mantle wedge is higher in the fractured seamount province than the area of Cocos Ridge. Contrary to the previous studies, the subduction in Cocos Ridge continues to deeper levels with a steeper angle causing a thickening of the overriding plate and transferring a smaller amount of water into the mantle wedge beneath the Talamanca range.

Chapter 5 presents the results of the simultaneous isotropic inversion of V_p , V_p/V_s and hypocenters in S Nicaragua/N Costa Rica. Results and synthetic tests confirm that forearc mantle wedge in southern Nicaragua is broadly hydrated and serpentinized while northern Costa Rica is almost dry. In addition, low V_p/V_s beneath the southern Nicaraguan volcanoes suggests a larger magma volume beneath southern Nicaraguan volcanoes than beneath northern Costa Rican volcanoes which is in agreement with Kutterolf et al. (2007) and Carr et al. (2007). These variations over a relatively short distance are a significant finding that demonstrates the importance of tectonic characteristics of the overriding plate while the incoming plate does not show significant lateral variations along the margin. Summarizing the chapter 4 and chapter 5, the seismogenic zone and slab geometry exhibit significant spatial variation due to the spatial change of the incoming plate in central Costa Rica while the observed variation in the seismicity and slab geometry is explained by the geologic and tectonic variations along the overriding plate in S Nicaragua/N Costa Rica.

Chapter 6 describes the P-wave anisotropic inversion for both regions, central Costa Rica and S Nicaragua/N Costa Rica, respectively. The results indicate a strong evidence of trench parallel mantle flow in Central America which correlates well with the shear wave splitting analysis (Hoernle et al., 2008). This observation explains why lead isotope signatures that are typical for Costa Rican lavas can be observed also in Nicaragua, though with decreasing concentration. These findings suggest trench parallel material

transport to the northwest.

Consequently, the results of the study contribute in understanding the tectonic structures, influence of the incoming plate and the overriding plate on the system, dehydration and hydration processes at the active continental margins. This study also links the seismic properties and the earthquake activity to subduction processes and active volcanism.

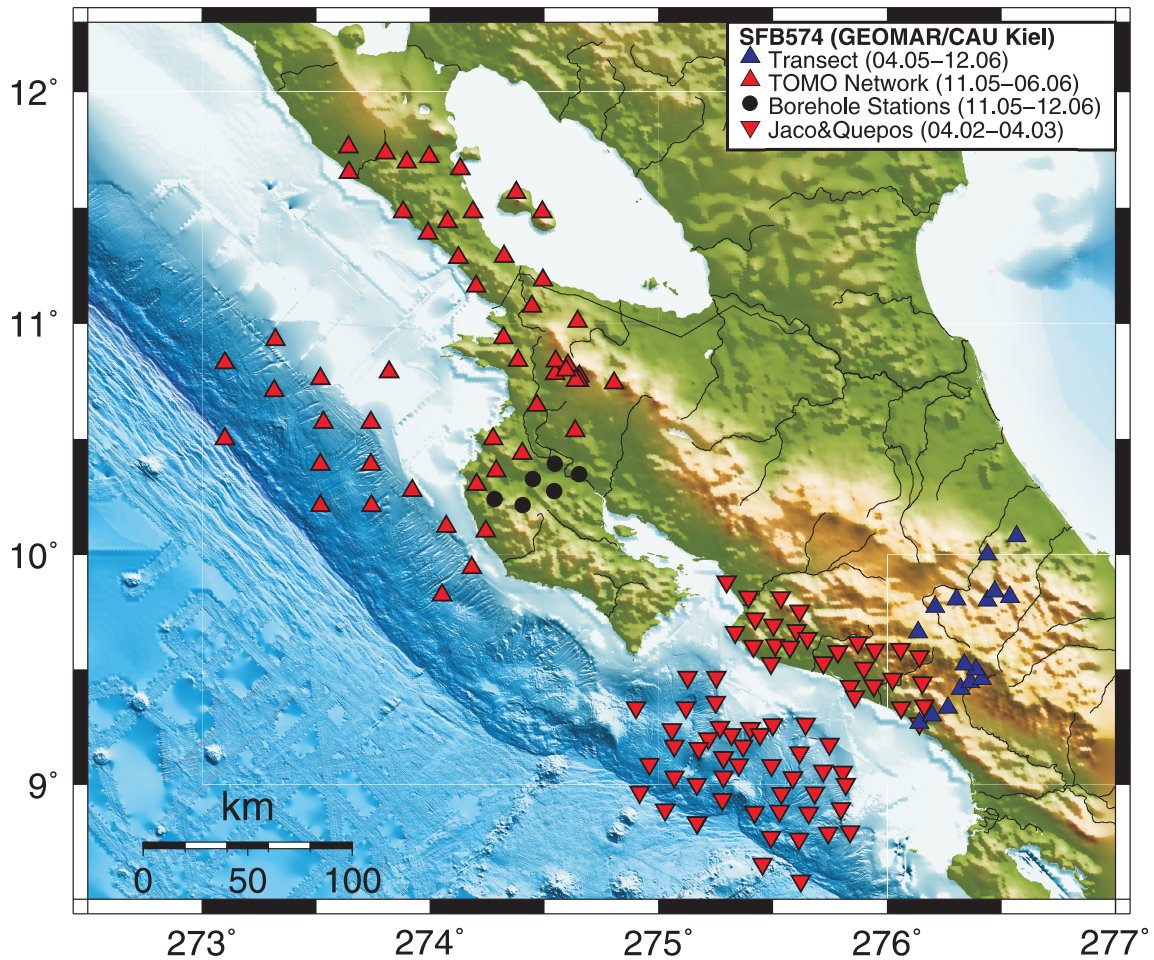


Figure 1.2: Seismological stations in Central America, being operated between 2002 and 2007 by SFB574. The red triangles indicate the three networks of central Costa Rica and S Nicaragua/N Costa Rica. The data from these networks are used to perform Local Earthquake Tomography and P-wave anisotropy calculations.

Chapter 2

Geology and Tectonic Settings

The tectonic setting of Central America is characterized by the subduction of the Cocos Plate beneath the Caribbean Plate. Cocos Plate shows strong lateral variations in relatively short distances. Lateral changes along the volcanic arc of the overriding Caribbean plate have been understood as a consequence of lateral changes in the structure, age and composition of the incoming oceanic Cocos plate (Carr et al., 2007; Hoernle and Hauff, 2007; Barckhausen et al., 2001; Werner et al., 1999). The incoming plate has been divided into three segments based on their morphology (von Huene, 1995): 1) A rather smooth segment of regular oceanic lithosphere with long trench parallel fractures off northern Costa Rica (Nicoya Peninsula segment) continuing to Nicaragua, 2) a topographically rough segment covered with seamounts off central Costa Rica (Jaco-Quepos segment), and 3) the thickened and rough oceanic lithosphere of the Cocos Ridge (Walther, 2003) subducting beneath southern Costa Rica (Osa Peninsula segment). A corresponding segmentation is found along the arc of the overriding plate: It is volcanically active along the projection of sections 1 and 2 but shows major geochemical differences in the magmas between 1 and 2 (Carr et al., 2003). Above the subducting Cocos Ridge the Talamanca mountain range formed where the active volcanism stopped in the Late Miocene (Gräfe, 1998), showing a recent uplift rate of up to 4.7 mm/yr (Gardner and Verdonck, 1992).

The composition and the segmentation of the Cocos Plate have been defined by magnetic anomalies (Barckhausen et al., 2001), multibeam bathymetry (von Huene, 1995; von Huene et al., 2000), seismic studies (Walther, 2003; Walther and Flueh, 2002; Wilson et al., 2003; Sallares and Charvis, 2003; Sallares et al., 2005) and geological sampling (Hauff et al., 1997; Werner et al., 1999; Hoernle and Hauff, 2007; Wilson et al., 2003). Following these studies, the Cocos Plate is generated at two different zones, the East Pacific Rise (EPR) in the west and the Galapagos Spreading Center (GSC) in the south. The part of the Cocos Plate generated along the EPR subducts beneath Nicaragua and northern Costa Rica. At the trench it is 20-24 Myr old. The part of the Cocos Plate

generated at the GSC is 20-22 Myr old where subducting beneath central Costa Rica, and 14-19 Myr old where subducting under southern Costa Rica (Barckhausen et al., 2001) (Fig. 2.1).

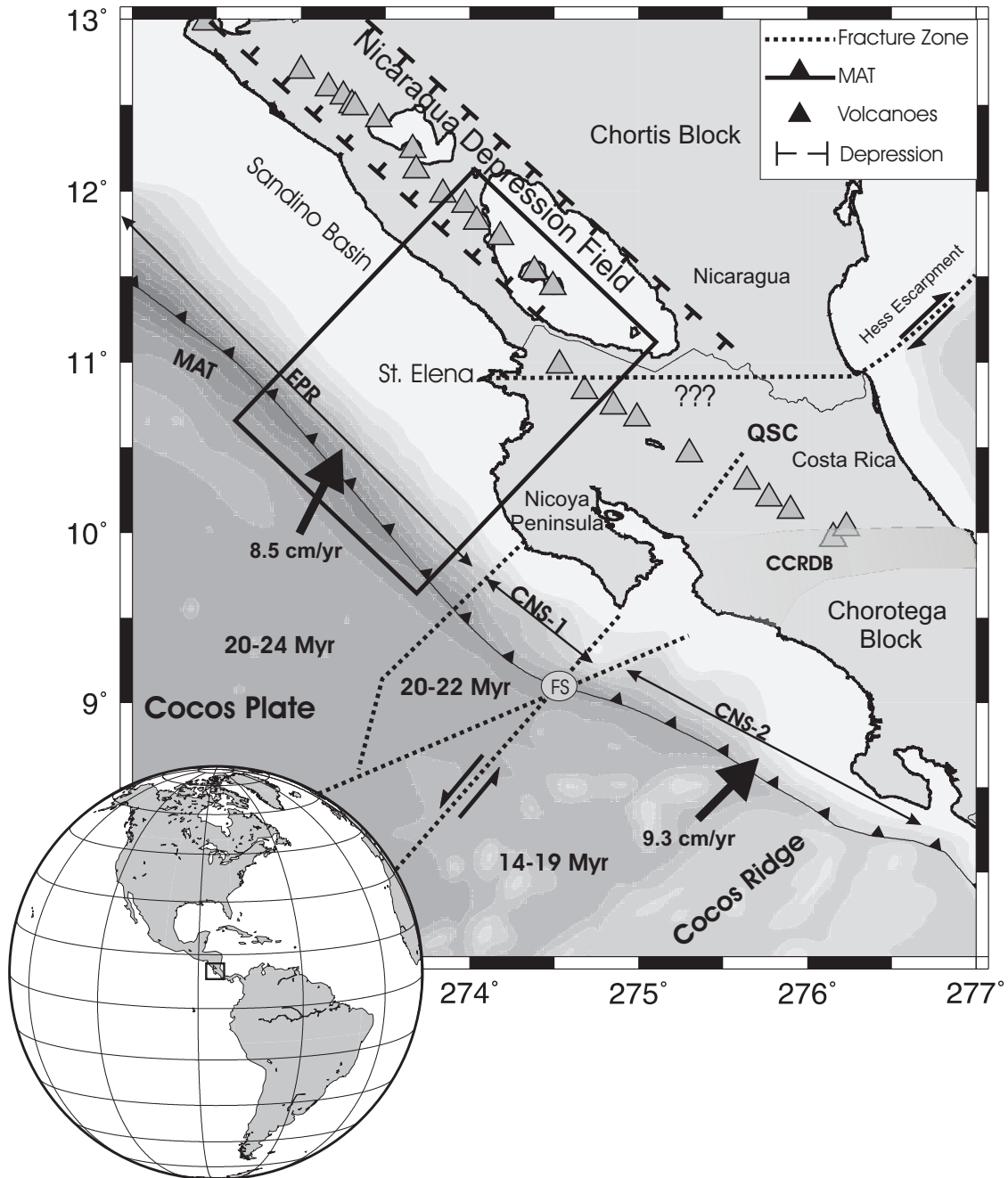


Figure 2.1: Tectonic features of Costa Rica and Nicaragua. The offshore tectonic structures are from Barckhausen et al. (2001). MAT: Mid-America Trench, EPR: East Pacific Rise, CNS-1: Cocos Nazca Spreading Center 1, CNS-2: Cocos Nazca Spreading Center 2, FS: Fisher Seamount. The onshore tectonics structures are from Protti et al. (1994) and McIntosh et al. (2007). CCRDB: Central Costa Rica Deforming Belt, QSC: Quesada Sharp Contortion.

2.1 Central Costa Rica

Numerous seismic marine multichannel reflection and onshore-offshore wide-angle refraction surveys have been carried out in the past decade to characterize the Pacific Costa Rican margin (Flueh and von Huene, 2007; Sallares et al., 2001; Christeson et al., 1999; Stavenhagen, 1998; Ye et al., 1996; Hinz et al., 1996). These studies show that the margin is currently eroding. The top of the wedge has only a thin sedimentary cover and is composed of oceanic crust similar to the ophiolitic outcrops found along the Costa Rican coast. The plate boundary is highly reflective along the whole Costa Rican margin. Seismic wide-angle studies suggest the presence of a thin low velocity layer of subducted sediment along the plate boundary. Offshore, close to the shoreline, the plate boundary is generally found at 12 to 15 km depth. The dip of the plate boundary is decreasing from NW to SE, and the margin wedge is thinnest in central Costa Rica where numerous seamounts are subducted.

This observation is also in agreement with seismological investigations, showing that the dip of the seismogenic zone and the Wadati Benioff Zone seismicity is decreasing from Nicaragua to southern Costa Rica. Also the maximum depth of the Wadati Benioff Zone (WBZ) seismicity decreases from 200 km in Nicaragua to 80 km in southern Costa Rica (Protti et al., 1995). Central Costa Rica is characterized by a higher seismicity compared to northern Costa Rica (Nicoya Peninsula) and southern Costa Rica (Osa peninsula). However, large events with magnitudes > 7 are only known from the Nicoya and the Osa segments, while in central Costa Rica no historical earthquake larger than magnitude 7.0 has been recorded. This suggests weaker seismic coupling in central Costa Rica, perhaps as a consequence of seamount subduction (Protti et al., 1994, 1995).

Most of our knowledge about Costa Rican seismicity results from the regional networks in Costa Rica, which have been in operation since the early 1980s. Sallares et al. (2000) and Quintero and Kissling (2001) compiled these data and presented a P-wave velocity model for Costa Rica. Their model shows that the average velocity is generally low and does not exceed 8.0 km/s in the upper 50 km of the mantle. In their studies the accuracy of hypocenter determination is limited by the application of a 1-D seismic velocity model and, more importantly, the lack of stations in the offshore area where most of the seismogenic zone earthquakes occur. Husen et al. (2002, 2003) used this data set for a tomographic 3-D inversion, and demonstrated the complexity and large lateral variability of the crustal and lithospheric structure. They find evidence for a subducted seamounts at 30 km depth beneath the shoreline (Husen et al., 2002). However, the seismogenic zone is not well resolved because of an unfavourable ray geometry of offshore earthquakes and onshore stations.

The seismogenic zone was investigated in more detail using local amphibious networks

near Osa pensinsula (DeShon et al., 2003) and off Nicoya peninsula (Newman et al., 2002; DeShon et al., 2006). These data enabled to distinguish plate interface earthquakes from intra-plate earthquakes. The authors also found evidence for mantle wedge serpentinization. Based on on-shore GPS data also locked and free slip areas of the seismogenic zone could be defined (Norabuena et al., 2004). Geographically, the data presented in our study form a bridge between these previous Nicoya and Osa seismic networks.

2.2 Southern Nicaragua / Northern Costa Rica

S Nicaragua/N Costa Rica is the transition from the oceanic Chorotega Block to the continental Chortis Block, although the exact boundary is not known. This transition probably occurs along a line connecting the Hess Escarpment in the Carribean Sea with the Santa Elena Peninsula at the Pacific coast (Bowland, 1993). Variations in the gravity field suggest that the crustal blocks have different thickness and composition (Mann et al., 2007; Elming and Rasmussen, 1997; Flueh and von Huene, 2007)

The Pacific margin of Nicaragua is characterised by a steepening slab dip and a seaward migration of the volcanic chain (McIntosh et al., 2007; Mann et al., 2007; Carr et al., 2003). The subduction direction is oblique to the margin causing the forearc terrane to move slowly northwest, parallel to the margin and to the volcanic arc. Relative to the interior of the Caribbean plate this motion is accommodated by faulting in the low-lying Nicaragua depression (Walther et al., 2000; McIntosh et al., 2007) leading to the formation of an extensional basin and arc parallel shearing (Fig. 2.1). The Sandino forearc basin off northern Nicaragua has a thickness of 14-22 km (McIntosh et al., 2007). The formation of the Sandino Basin is most probably associated with an extension of the underlying crust and mantle wedge and with a thinning of the overriding plate as such. This view is fostered by the observed steepening slab dip and the seaward migration of volcanic chain in Nicaragua over time. Regarding the hydration and dehydration processes, an extensional stress regime could be important mechanism which may favour the formation of fluid path ways within the overriding plate (Seno, 2005).

Numerous seismic marine multichannel reflection and onshore-offshore wide-angle refraction surveys have been carried out in the past decade to characterize the Nicaraguan convergent margin (McIntosh et al., 2007; Ranero et al., 2000; Walther et al., 2000). The following findings are of special relevance for the present study: Half-grabens filled with sediment form at the top of the Cocos Plate as it bends into the trench. High resolution bathymetric mapping of the incoming plate showed that bending-related faulting is pervasive across most of the ocean trench slope. Multi-channel seismic reflection data presented by Ranero et al. (2003) show that these faults cut ~ 20 km into the lithosphere.

Ranero et al. (2003) suggested that they promote fluid flow down to mantle depth and cause hydration of the mantle between the outer rise and the trench axis. Analyzing seismic velocities and offshore seismicity (Lefeldt et al., 2008; Grevemeyer et al., 2007) brought further evidence that the incoming Cocos plate is hydrated although much reduced in volume.

Additional evidence for an increased degree of hydration and hence serpentinization is perhaps provided by geochemical data from the volcanic arc, which suggests that mafic magmas in Nicaragua have water concentrations among the highest world-wide (Carr et al., 2003; Kutterolf et al., 2007). Also, seismological data suggest that regional P-waves from intraslab events at 100-150 km depth show high-frequency late arrivals, apparently trapped in a 2.5-6 km thick low-velocity waveguide at the top of the downgoing plate. Such low velocities can best be explained by > 5 wt.% of water in the subducted crust, 2-3 times the hydration inferred for other slabs (Abers et al., 2003).

Thus, it seems to be well established that the slab contains a high concentration of fluids in Nicaragua.

Chapter 3

Method

3.1 Introduction

Local Earthquake Tomography (LET) is an iterative algorithm to simultaneously invert the 3D velocity model and hypocentral parameters. Algorithms for LET have been developed since the seventies (Aki and Lee, 1976; Thurber, 1983; Thurber, 1986; Thurber and Aki, 1987; Kissling, 1988). The most common algorithm is the SIMULPS code, developed and used by many authors (e.g. Thurber, 1983; Eberhart-Phillips, 1986; Husen et.al., 2002).

However, the main goal of the LET is to improve the initial estimates of the model parameters (velocity and hypocenter) by perturbing them in order to minimize the misfit of the data. By its nature, LET is a non-linear process. In general, solutions are obtained by linearization with respect to a reference Earth model. The resulting tomographic images are dependent on the initial reference model and hypocentral locations. The only knowns in the LET problem are the receiver locations and observed arrival times. The source coordinates, origin times, ray paths and velocity field are unknown parameters. Therefore, the input data for every tomographic algorithm consist of the absolute arrival times from local seismic events and station coordinates. The algorithms may differ in the representation of the velocity structure (grid parametrization), travel time and ray-path calculation (ray tracing), inversion and assessment of the solution quality (Thurber, 1993).

In this study, we used the tomographic algorithm LOTOS (LOcal TOMography Software), designed for simultaneous inversion for P and S velocity structure and source coordinates (Koulakov et al., 2007). The inversion technique used by this code is based on the LSQR technique (Paige and Saunders, 1982; Van der Sluis and van der Vorst, 1987) and uses the bending method (Um and Thurber, 1987) for ray tracing.

Algorithms for anisotropic seismic tomography are being developed since the sixties (Backus, 1965). Lately, Ishise and Oda (2005) presented a seismic tomography method incorporating lateral variations of isotropic and anisotropic velocity structures, modifying the method developed by Hirahara and Ishikawa (1984). A similar tomography technique was developed to infer lateral variation of the fast propagation direction of P-waves (Hearn, 1996; Eberhart-Phillips and Mark Henderson, 2004). In particular, Eberhart-Phillips and Mark Henderson (2004) improved Hearn (1996)'s technique that determines simultaneously both two dimensionally varying velocity and azimuthal anisotropy from Pn travel time data and estimated 3-D structure of isotropic and anisotropic velocity by analyzing P-wave travel time data through the improved Hearn's technique. In this study, we used the ANITA algorithm (ANIsotropic Tomography Algorithm) for anisotropic inversion, provided by I. Koulakov (by personal communication), for iterative non-linear inversion of local earthquake data in orthorhombic anisotropic media with one predefined vertical orientation.

3.2 Inversion for V_p and V_s

The arrival time (t) of a seismic wave at a station (r) is a non-linear function of the hypocentral parameters (\mathbf{h}^{src}), velocity field (\mathbf{V}) and the station coordinates (\mathbf{m}^{st}). The following equations are of the same form for P and/or S arrival time data.

$$t = f(\mathbf{h}^{src}, \mathbf{V}, \mathbf{m}^{st}) \quad (3.1)$$

Equation 3.1 is linearized by the Taylor Series expansion to obtain a linear relationship between the arrival time residuals and adjustments to the hypocentral, velocity and station parameters:

$$dt_{ir} = t_{ir}^{obs} - t_{ir}^{cal} \simeq W_i^{src} \frac{\partial t_{ir}}{\partial h_{ik}} dh_{ik} + \frac{\partial t_{ir}}{\partial V_j} dV_j + W_r^{st} dm_r^{st} \quad (3.2)$$

where dt_{ir} is the arrival time residual for one ray connecting source i ($i=1, n_{source}$) to receiver r ($r=1, n_{receiver}$). t_{ir}^{obs} represents the observed and t_{ir}^{cal} indicates the calculated arrival times in the reference velocity model. The residuals are related to the desired perturbations to the hypocentral (dh_{ik} , $k=1,4$ source coordinates and the origin time), velocity (dV_j , $j=1, n_{nodes}$) and station parameters (dm_r^{st}) by a linear approximation. W_i^{st} is the weight factor for station corrections and W_r^{src} is a weight factor for controlling the source parameters which is defined by $\partial t_{ir} / \partial h_{ik}$. The velocity model partial derivatives $\partial t_{ir} / \partial V_j$ are computed along the rays for the nodes in the 3D model grid.

Supplementary equations are defined for controlling the smoothness and amplitude of the velocity models:

$$S_m(dV_m - dV_n) = 0 \quad (3.3)$$

$$R_e dV_j = 0 \quad (3.4)$$

where S_m and R_e are constants. Equation 3.3 contain two non-zero elements with opposite signs, corresponding to neighboring parametrization nodes in the model. The data vector corresponding to this row is zero. Increasing the weight of this element (S_m), will have a smoothing effect upon the resulting anomalies. The amplitude of the model is controlled by the equation 3.4 where R_e is the coefficient for the amplitude adjustment (regularization parameter).

The iterative inversion algorithm of LOTOS (Koulakov and Sobolev, 2006; Koulakov et al., 2007) consists of the following steps (Fig. 3.1):

1. Rough positions of sources: are determined using a location algorithm based on a 1D velocity model. It is an algorithm of searching for an absolute extreme of a goal function (GF) which reflects the probability of the source position being at a point in 3D space. For this step, the travel times are calculated based on tabulated values computed once for the rays with different epicentral distances and source depths. In case of the 3D velocity starting model, the tabulated travel times are computed for the 1D velocity model which is closest to the reference model. The search of the GF extreme is performed starting from the position of the station with minimum arrival time using a coarse grid for rough location and finer grid for final solution. It was shown that this location method is very stable and depends weakly on the starting point. In particular, it provides the same resulting source position even if the starting points are located 200 km from each other.
2. Correction of the source coordinates: is performed according to another localization algorithm which is designed for an arbitrary 3D model and based on the ray tracing bending method (Um and Thurber, 1987). The source location is based on searching for a maximum gradient of the GF.
3. 3D representation of the velocity field: is constructed according to the ray density. The 3D velocity anomalies are computed in nodes distributed in the study volume. The velocity distribution between the nodes is interpolated linearly using subdivision of the study volume into tetrahedral blocks. In each vertical plane, nodes are distributed according to the ray density. In areas with less ray coverage, the distance between nodes is larger. To avoid an excessive concentration of nodes in areas with high ray density, the minimum spacing between nodes is fixed at 5 km, which is significantly smaller than a characteristic size of the expected anomalies. However, since the nodes are placed on planes having a predefined orientation, this can bring some artifacts to the result of the inversion. To reduce the effect of grid orientation the inversion is performed in four differently oriented grids (0° , 45° , 90° and 135°) and the results are stacked in one model.

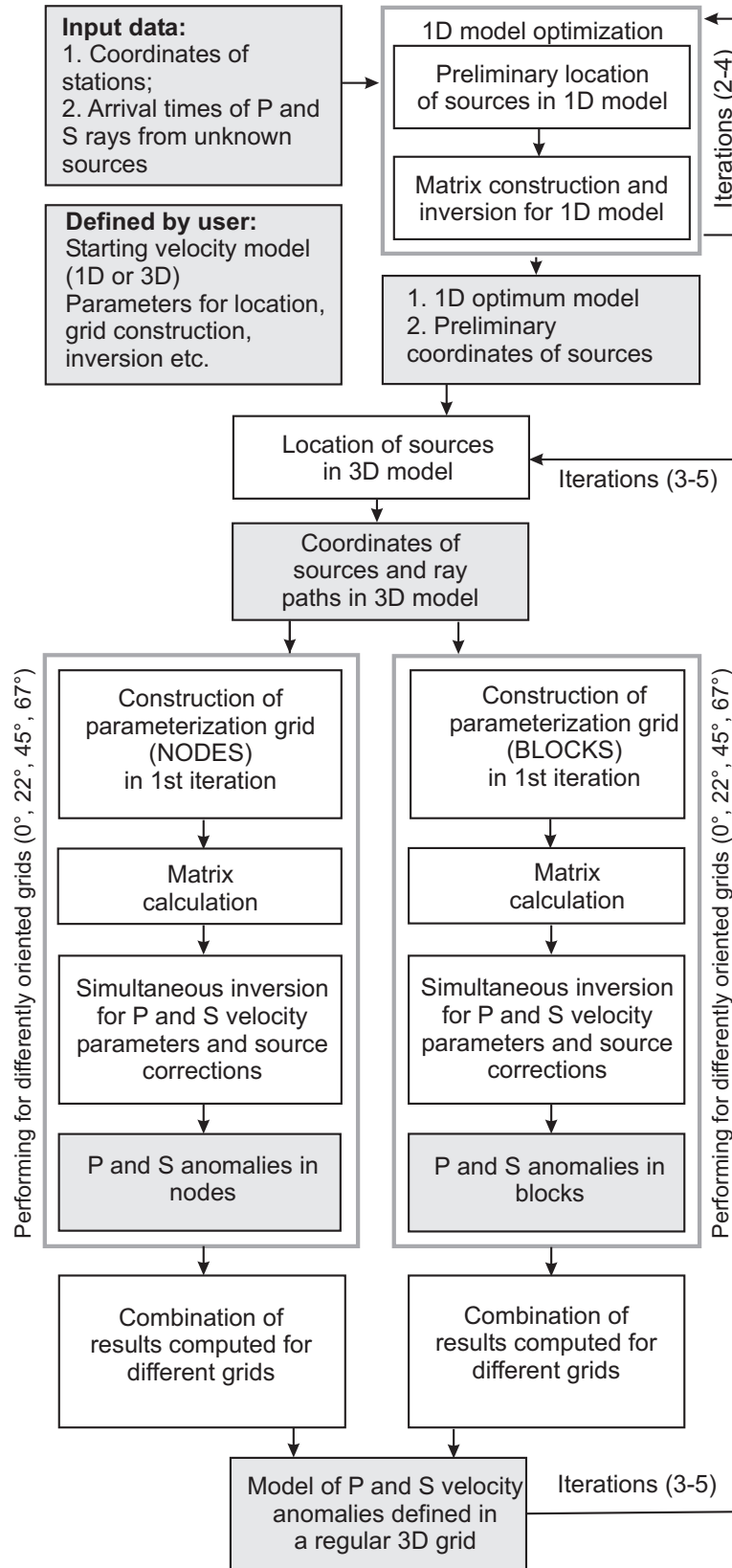


Figure 3.1: Block scheme of the LOTOS algorithm from Koulakov et al. (2007).

4. Calculation of matrix: is performed along the rays computed by the bending method after the Step 2. The effect of velocity variation at each node on the travel time of each ray ($\partial t/\partial V$) is computed numerically, as in Koulakov and Sobolev (2006). The data vector corresponding to this matrix consists of residuals obtained after the step of source location.
5. Inversion: is performed simultaneously for P and S velocity anomalies, source parameters (4 parameters for each source) and P and S station corrections using the LSQR method (Paige and Saunders, 1982; Van der Sluis and van der Vorst, 1987).
6. The P and S velocity models are updated and used for the next iteration which consist of the repetition of steps 2, 4, and 5.

3.3 Inversion for Vp and Vp/Vs

Vp/Vs ratio, or Poisson coefficient, is an important parameter in investigating the rocks' petrophysical state. We used the LOTOS program to perform the Vp/Vs inversion. The algorithm is designed using node parameterization, as for the case of Vp and Vs inversion described above. The grids for Vp and $X = Vp/Vs$ are constructed according to the density of P and S rays, respectively.

The arrival time residuals for Vp and Vs are of the same form as equation 3.2. For the variations of X the system of linear equation is:

$$dt_{ir}^{diff} = d(t_{ir}^S - t_{ir}^P) \simeq \left(\frac{1}{X_k} \frac{\partial t_{ir}^S}{\partial V_k^S} - \frac{\partial t_{ir}^P}{\partial V_k^P} \right) dV_k^P - \frac{V_m^S}{X_m} \frac{\partial t_{ir}^S}{\partial V_m^S} dX_m + \mathbf{F}dh \quad (3.5)$$

In equation 3.5, the data vector is represented by differential residuals, corresponding to P and S rays recorded at one station: $dt_{ir}^{diff} = dt_{ir}^S - dt_{ir}^P$. The derivatives $\partial t_{ir}^S/\partial V_k^S$ and $\partial t_{ir}^P/\partial V_k^P$ are computed along P and S rays for the nodes in the P-model grid. X_k is a reference value of Vp/Vs ratio at the k-th node of the P-model grid.

The derivative $\partial t_{ir}^S/\partial V_m^S$ is computed along the S-ray for the nodes in the S-model grid. X_m and V_m^S are reference values of Vp/Vs ratio and Vs at the m-th node of the S-model grid. Hypocentral parameter corrections $\mathbf{dh}(dx, dy, dz, dt)$ in equation 3.5 are associated with the matrix elements $\mathbf{F}(p_x^S - p_x^P, p_y^S - p_y^P, p_z^S - p_z^P, 0)$ (elements of the P and S rays slowness vector at the source point. After the inversion, the distribution of the Vp/Vs ratio is converted to a Vs model, and the relocation of sources is performed according to the algorithm described in the previous section.

3.4 Inversion for P-wave Anisotropy

The ANITA algorithm (ANIsotropic Tomography Algorithm) by I. Koulakov (personal communication), is an iterative non-linear inversion of local earthquake data in an orthorhombic anisotropic media. This algorithm considers only P-wave anisotropy. It presumes that the anisotropy of P velocity can be described by horizontally oriented ellipsoid. At each point, seismic P-wave velocities depend on the propagation direction and their distributions have three orthogonal main axes. One of them is oriented vertically and the other two are in the horizontal plane. As a result of the tomographic inversion, four parameters are determined for each point of the study volume. Three of them, $d\sigma_0$, $d\sigma_{60}$, $d\sigma_{120}$ are variations of slowness in the horizontal plane along three different azimuthal directions, 0° , 60° and 120° , respectively, as shown in figure 3.2. The fourth parameter, $d\sigma_{ver}$, is a slowness variation along the vertical axis. Using these four parameters, the slowness along a ray with the azimuth α and dipping angle β (measured upward from the vertical axis) can be represented as:

$$\sigma = \sigma_{ref} + (d\sigma_{hor} \sin\beta + d\sigma_{ver} \cos\beta) / (\sin\beta + \cos\beta) \quad (3.6)$$

where

$$\begin{aligned} d\sigma_{hor} &= d\sigma_1 + d\sigma_2 + d\sigma_3 \\ d\sigma_1 &= \frac{1}{3}[\cos 2\alpha + 1]d\sigma_0 \\ d\sigma_2 &= \frac{1}{3}[\cos 2(\alpha - \frac{\pi}{3}) + 1]d\sigma_{60} \\ d\sigma_3 &= \frac{1}{3}[\cos 2(\alpha + \frac{\pi}{3}) + 1]d\sigma_{120} \end{aligned} \quad (3.7)$$

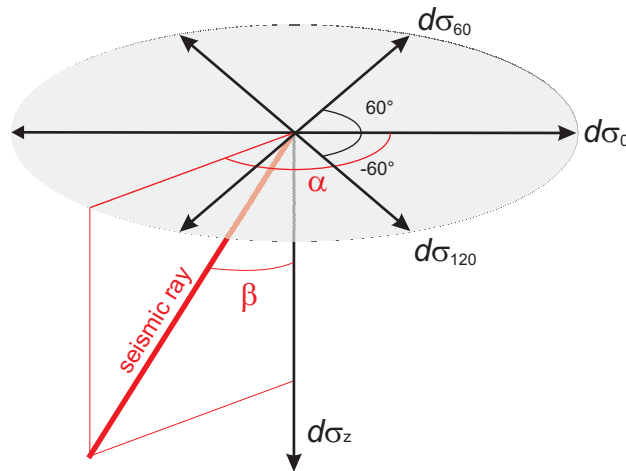


Figure 3.2: Sketch for definition of the anisotropic model from I. Koulakov (personal communication).

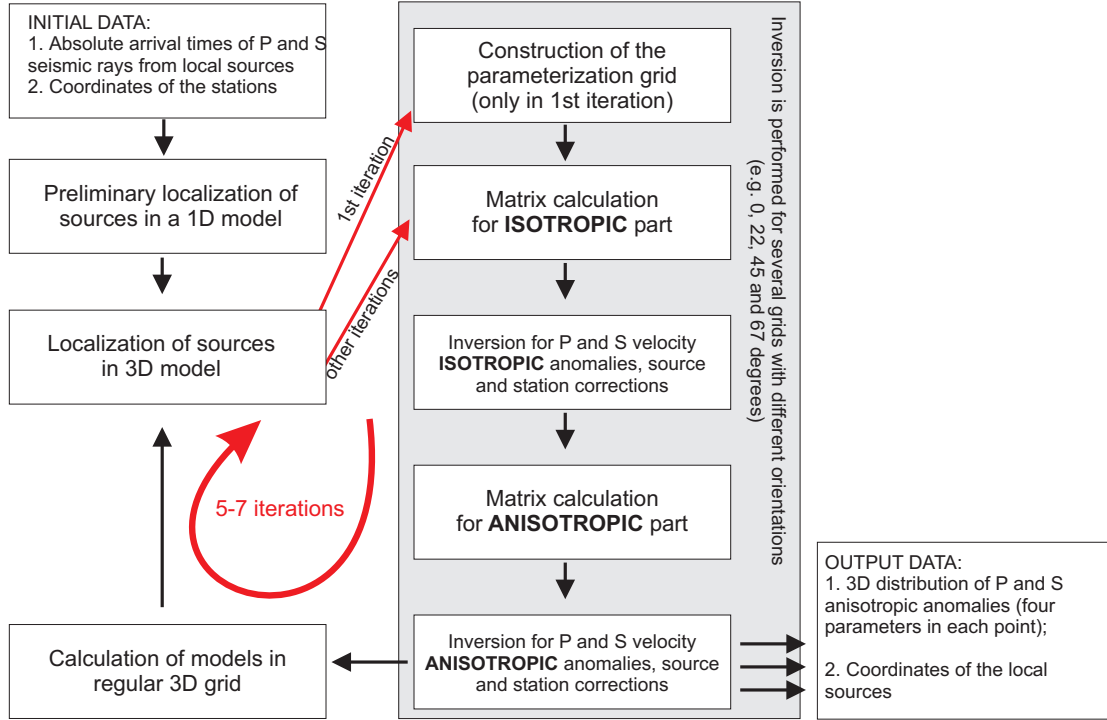


Figure 3.3: Block scheme of the ANITA algorithm from I. Koulakov (personal communication).

The general structure of the algorithm is shown in figure 3.3. The processing starts with the preliminary location of the sources using tabulated travel times of a 1D model. After that, the source parameters are adjusted using the location code designed for 3D heterogeneous anisotropic media.

The algorithm of source localization is based on the bending method of ray tracing which uses the general idea of minimization of travel time proposed in Um and Thurber (1987). The practical realization of this algorithm is described in Koulakov et al. (2007). The velocity in each point of the ray path is computed according to a predefined 3D velocity model. In case of anisotropy, the velocity depends on the ray direction in the current point and is determined according to the values of four parameters, $d\sigma_0$, $d\sigma_{60}$, $d\sigma_{120}$, $d\sigma_{ver}$, using formulas 3.6 & 3.7.

Grid parameterization in the algorithm is performed in Cartesian coordinates by subdividing the study volume into rectangular cells. The size of the cells vary size according to the ray density. The size of blocks becomes larger if the ray density is low. In each iteration, the subdivision of blocks is performed regarding to the total length of the rays inside the each block.

The calculation of the first derivative matrix is performed numerically along the rays. The elements of the matrix which are equal to the travel time variations of a ray due

to the unit variations of each of the four slowness components in each parameterization block are computed as:

$$dt_{ir} = S_{ijr}d\sigma_j(\alpha, \beta) \quad (3.8)$$

where S_{ijr} is the length of the i -th ray in the j -th cell and $d\sigma_j$ is the slowness variation along the ray (with azimuth α and dipping angle β) related to the unit variation of one of the four slowness components in the j -th cell, which is computed using formulas 3.6 & 3.7. The inversion is performed simultaneously for P anomalies (four components for each block) and the source corrections (four parameters for coordinates and origin time). The main system of equation is similar with equation 3.2:

$$dt_{ir}^P = \frac{\partial t_{ir}}{\partial \sigma_j^{P0}} d\sigma_j^{P0} + \frac{\partial t_{ir}}{\partial \sigma_j^{P60}} d\sigma_j^{P60} + \frac{\partial t_{ir}}{\partial \sigma_j^{P120}} d\sigma_j^{P120} + \frac{\partial t_{ir}}{\partial \sigma_j^{PZ}} d\sigma_j^{PZ} + W_i^{src} \frac{\partial t_{ir}}{\partial h_{ik}} dh_{ik} \quad (3.9)$$

$d\sigma_j^{Pk}$ is one of four components ($k = 1...4$) of the P-wave slowness perturbations in the j -th block, W_i^{src} is the weight for the source parameters and dt_{ir}^P is the observed P residual along the i -th ray. dh_{ik} is the source parameter corrections which describe source coordinates and origin time. The control of the amplitudes and smoothing parameters are defined by several supplementary matrix blocks. The first block controls the amplitude of the anomalies and consist of diagonal matrices with zero data vector:

$$R_e d\sigma_j = 0 \quad (3.10)$$

R_e is the coefficient that controls the amplitude levels of the P anomalies. The next blocks aim to smooth the slowness components in space. For two neighboring cells, m and n , the following equations are defined for the P model:

$$\begin{aligned} S_{m_hor}(d\sigma_m^{P0} - d\sigma_n^{P0}) &= 0 \\ S_{m_hor}(d\sigma_m^{P60} - d\sigma_n^{P60}) &= 0 \\ S_{m_hor}(d\sigma_m^{P120} - d\sigma_n^{P120}) &= 0 \\ S_{m_ver}(d\sigma_m^{PZ} - d\sigma_n^{PZ}) &= 0 \end{aligned} \quad (3.11)$$

where S_{m_hor} and S_{m_ver} are the coefficients which control the smoothing of the horizontal and vertical components of slowness. In addition, it is possible to control the anisotropy level within each parameterization cell using the following equations:

$$\begin{aligned} S_{m_an}(d\sigma_m^{P0} - d\sigma_m^{P60}) &= 0 \\ S_{m_an}(d\sigma_m^{P0} - d\sigma_m^{P120}) &= 0 \\ S_{m_an}(d\sigma_m^{P0} - d\sigma_m^{PZ}) &= 0 \end{aligned} \quad (3.12)$$

where S_{max} is the coefficient which controls the anisotropy amplitude (difference between maximum and minimum velocity perturbations) within each cell. Increasing these coefficients forces the model to be more isotropic.

After calculating the slowness components for the differently oriented parameterization grids, the obtained results are averaged into one regular 3D grid. This model is used in the next iteration, which contains source location for new anisotropic P model, matrix calculation and inversion.

The inversion is performed using the LSQR method (Paige and Saunders, 1982; Van der Sluis and van der Vorst, 1987). The resulting anisotropy is illustrated by vector fields in horizontal sections. Orientations of vectors show the maximum velocity direction in the horizontal plane. The length of the vectors reflects the magnitude of the anisotropy, which is computed as:

$$A^{hor}(\%) = 100(dV_{max} - dV_{min})/V_{ref} \quad (3.13)$$

where dV_{max} and dV_{min} are the maximum and minimum velocities in the horizontal plane and V_{ref} is the reference velocity.

Chapter 4

Central Costa Rica

4.1 Introduction

The Central America convergent margin off Costa Rica has been intensively studied for many years because strong lateral variations in the subduction system (incoming plate, seismicity, arc volcanism) are encountered at relatively short distances, making this an ideal laboratory to investigate subduction zone processes. The investigation area is located in central Costa Rica and reaches from the trench to the volcanic front. It thus covers the forearc area of the seamount subduction province as well as its border to the Osa segment. By applying joint on- and offshore local earthquake tomography I am aiming to investigate the following points related to the question of stress transfer and mass transport from the subducting to the overriding plate:

1. Do the seismogenic zone and stress transfer change in correspondence to the incoming plate?
2. If so: What changes in slab geometry and crustal structures are related to these variations?
3. Is there evidence of fluid transport from the dewatering subducting plate into the mantle wedge and up to the volcanic arc?
4. Do the seismic velocities or Poisson's ratio indicate substantial differences in the crustal structure across the edge of the active section of the volcanic arc?

Based on two temporal seismic networks with an average station spacing of 15 km, I aimed to obtain high resolution P- and S-wave tomographic images and hypocenter locations as a basis for tectonic interpretation. Previous local seismicity and teleseismic studies based on the Costa Rican permanent regional network were performed with only

P-waves. They cover the central part of Costa Rica almost completely but with a lower spatial resolution and they do not include the off-shore area (Quintero and Kissling, 2001; Colombo et al., 1997; Husen et al., 2003; Protti et al., 1999; Sallares et al., 2000; Yao et al., 1999). Further geophysical and geologic background information is provided by regional studies including seafloor age dating (Hoernle and Hauff, 2007; Barckhausen et al., 2001) and a wealth of geological, tectonic and volcanological investigations (for an overview see, for example, Bundschuh & Alvarado, 2007).

4.2 Data Base

Two temporary amphibious seismological networks, named JACO and QUEPOS, were deployed along the Pacific coast of central Costa Rica in 2002 and 2003, respectively. The networks comprised a total of 46 ocean bottom and 27 land stations (Fig. 4.4 & 4.10). Most of the marine stations were only hydrophones, nine of them were equipped with seismometers (IFM-Geomar type OBS as described by Bialas and Flueh (1999)). The land stations were short period Mark-L-3D seismometers with Reftek recorders provided by the German instrument pool of GFZ (Potsdam). JACO was operated from April 2002 to October 2002 while QUEPOS was operated from September 2002 to May 2003. The station list is given in Appendices B1 & B2. Figure 4.1 shows an example of an event recorded at several stations. Figure 4.2 & figure 4.3 give examples how the picking procedure was performed.

More than 4000 earthquakes were located (Fig. 4.4) by the standard earthquake location procedure HYPO77 using the revised minimum 1-D model from Quintero and Kissling (2001) for Costa Rica which consists of constant velocities (Table. 4.1). P-wave onsets recorded by the stations of the Red Sismológica Nacional of Costa Rica (RSN) (Appendix B3), from September 2002 to May 2003, were also included into the database to improve the coverage and to increase the number of intra-plate and Wadati-Benioff zone events. For the tomographic inversion the data set was edited on the basis of a preliminary hypocenter localization with a 1D-velocity model and the following criteria: (1) each event observed at a minimum number of 10 stations or more; (2) horizontal distance to the nearest station of the network < 150 km; (3) rejection of the events if the travel time residual after the preliminary localization > 1 s; (4) elimination of events which show deviations less than 2 km in horizontal and less than 5 km in vertical position which is determined by a statistical approach. Applying these criteria, 31912 P-wave and 9298 S-wave travel time observations from 2079 events were selected for the inversion (Fig. 4.10).

In order to estimate the error of the obtained velocity fields and hypocenter locations

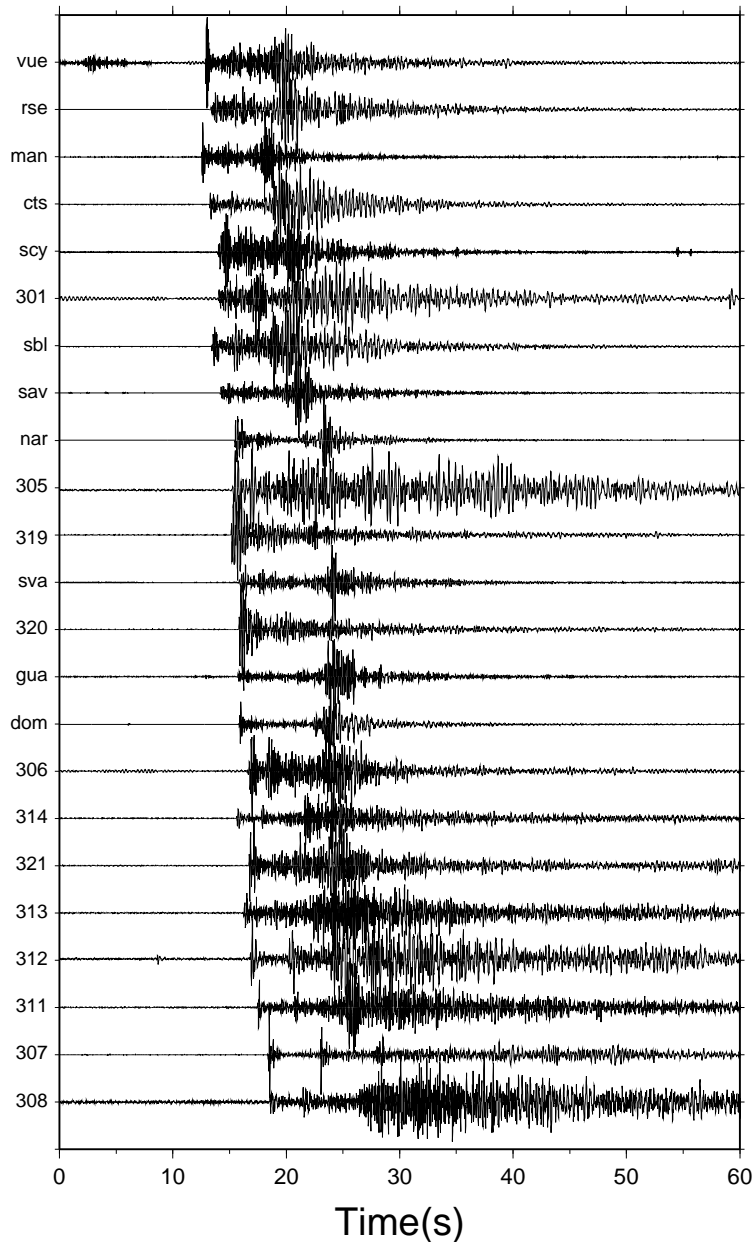


Figure 4.1: Example of a record section for the event that occurred on 16.12.2002 at 19:16:55. Hydrophone components of the ocean bottom stations and vertical components of the land stations are displayed.

which is mentioned in the criteria 4 of the data editing, the following approach is applied: 10 subsets of the original data set, each containing 70 % of the data were randomly selected. Each subset was inverted in five iterative steps using the same processing parameters as applied to the full data set. After the inversion, the deviations of the hypocenter locations and velocity models were calculated with respect to the average value and visualized in the form of a cumulative frequency distribution (Fig. 4.5). By

picking the 95 % limits from the histograms of deviations in Fig. 4.5 I estimated the global standard deviations of 2 km for the horizontal and 5 km for the vertical coordinates of the hypocenters. For the subsequent final tomographic inversion I edited the travel time data again keeping only those events in the data base which had shown deviations less than 2 km in horizontal and less than 5 km in vertical position which reduced the number of events from ~ 3044 to 2079.

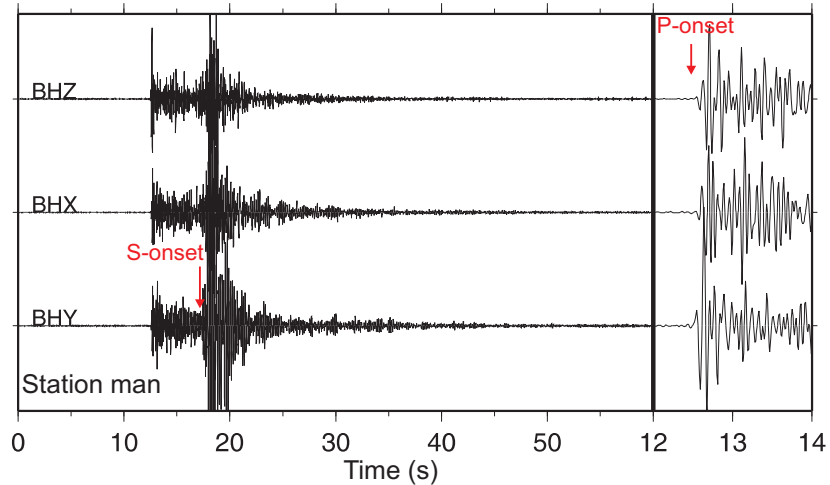


Figure 4.2: Example recording of the event in Fig. 4.1 at the 3 component land station man. The P-wave onsets are picked from the vertical component (BHZ) and the S-wave onsets are picked from the lateral components (BHX or BHY).

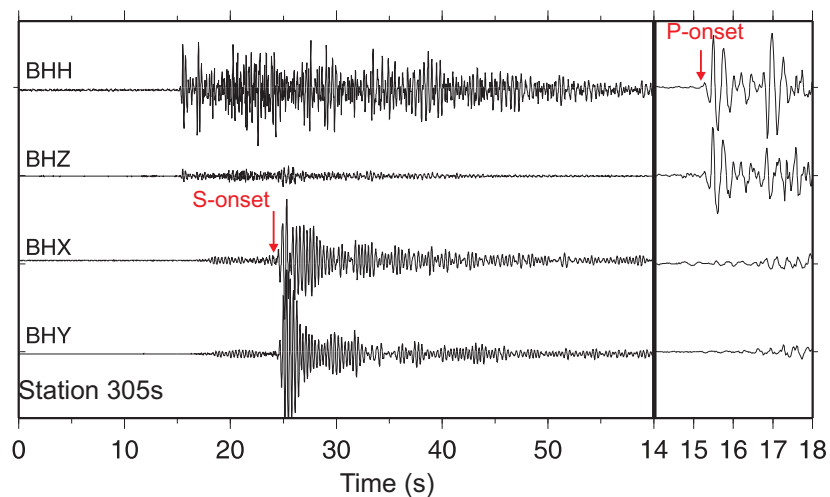


Figure 4.3: Example recording of the event in Fig. 4.1 at the 4 component sea station o305. The P-wave onsets are picked either from the hydrophone (BHH) or vertical component (BHZ). The S-wave onsets are picked from the lateral components (BHX or BHY) of the seismometers.

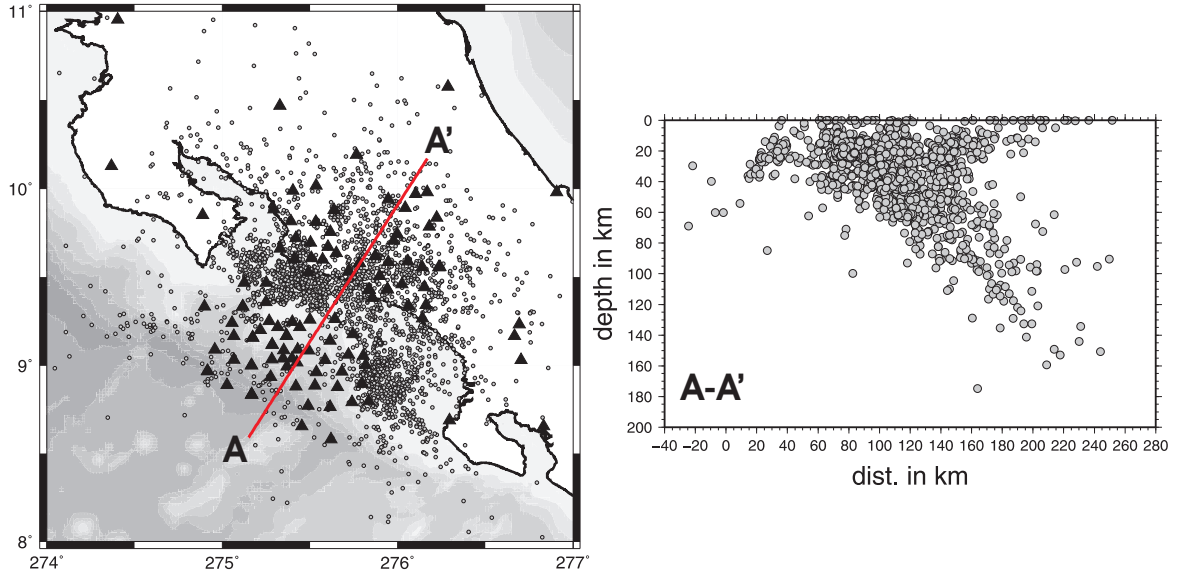


Figure 4.4: Distribution of events (circles) recorded by JACO, QUEPOS and RSN networks shown by triangles (left). Depth distribution of events along profile A-A' (right) in a 50 km band.

Table 4.1: Background model of V_p and V_s applied in the tomographic inversion.

Depth (km)	V_p (km/s)	V_s (km/s)
0.0	4.45	2.50
4.0	5.50	3.00
6.0	5.60	3.15
8.0	6.00	3.37
11.0	6.15	3.45
14.0	6.25	3.51
21.0	6.50	3.65
28.0	6.80	3.82
34.0	7.00	3.93
44.0	7.30	4.10
54.0	7.90	4.44
74.0	8.20	4.60
104.0	8.30	4.66
124.0	8.35	4.69
154.0	8.40	4.72

4.3 Resolution Tests

In order to show that the tomographic inversion produces reliable images of the subsurface structure I investigated the stability of inversion results with respect to a random

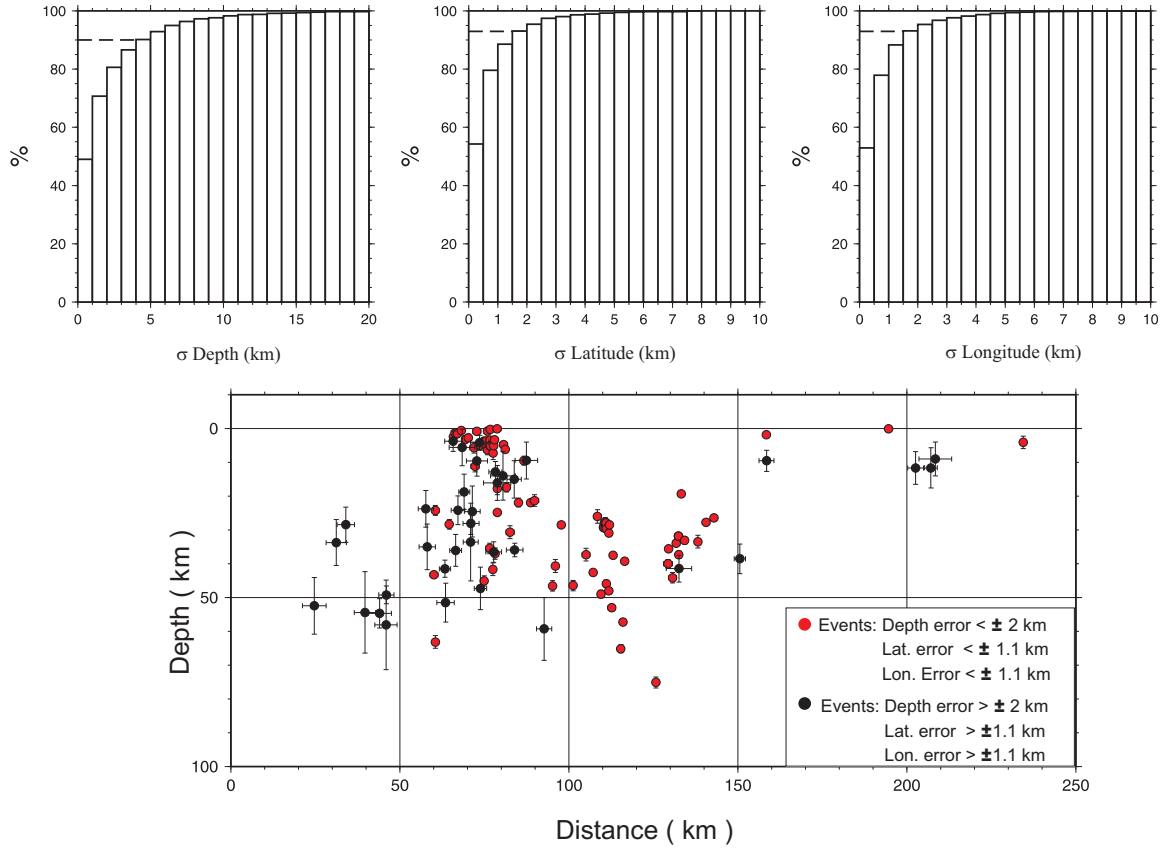


Figure 4.5: Statistical approach for calculating the standard deviation of events in the mean of latitude, longitude and depth. Upper row shows the histograms indicating the distribution of deviations for all events. Lower row is the distribution of events in a depth-distance section along profile-6 in Fig. 4.10. Red circles indicate the events with small deviation which are selected for the data base and black circles denote the rejected events.

selection of input data (Section 4.3.1) and performed three different tests of spatial resolution based on synthetic data (Section 4.3.2). Since the data are from a combination of three different networks operated in different time periods, I paid special attention to the resolution in the overlapping areas.

4.3.1 Test with a random selection of events

In order to investigate the influence of random noise in the real travel time data, I performed independent inversions for two randomly separated data subsets. The subsets were selected by choosing events with either odd or even identification numbers. In the case of a strong noise influence the correlation between the different results should be low. In figure 4.6 results are presented in two vertical and one horizontal sections corresponding to the independent inversion of data sets with odd, even and all events. It is obvious that the prominent features are recognizable in all subsets. Even small

patterns in the coastal area are robustly retrieved with both data subsets. The test shows that the noise in the data has negligible effect on the stability of the results.

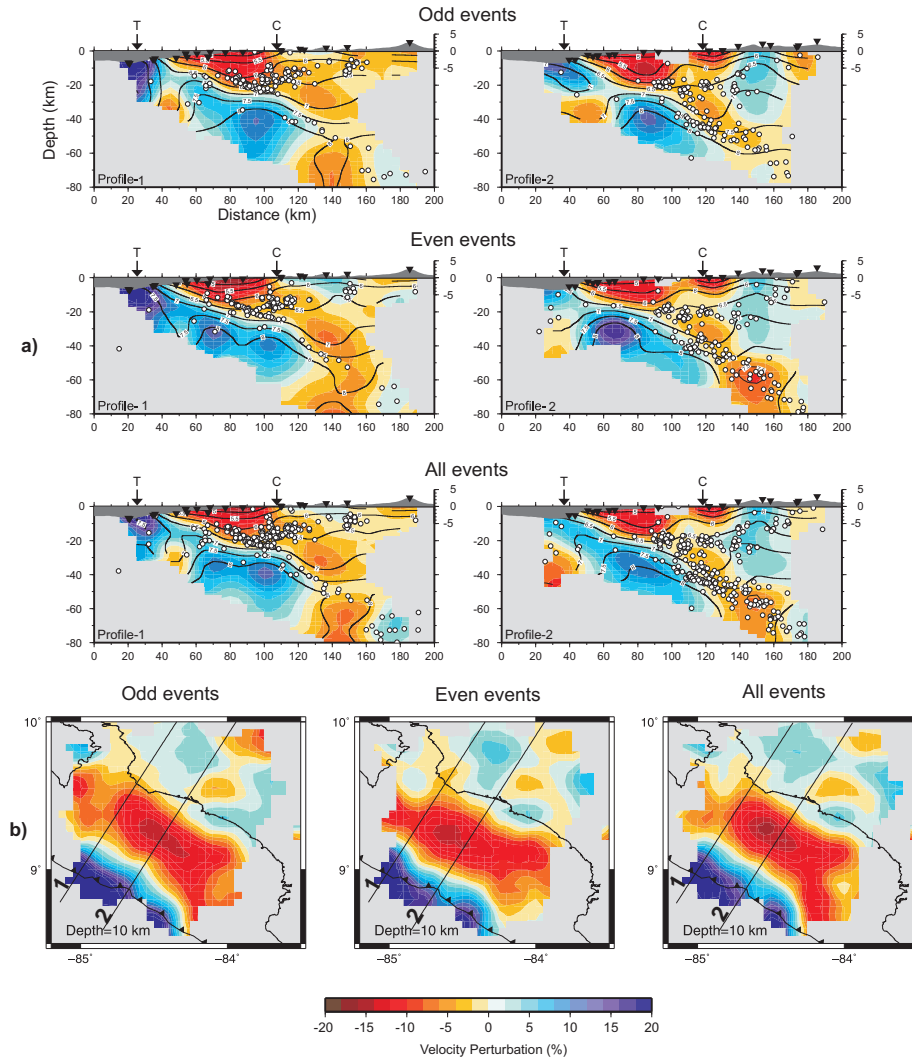


Figure 4.6: P and S velocity anomalies obtained from the inversion of odd, even number of events and all data set. a) Vertical sections along the profiles 1 & 2 shown in Fig. b). White circles: earthquakes; T: trench; C: coast; triangles: stations. Contours represent the absolute velocities with an interval of 0.5 km/s. b) Horizontal sections from 10 km depth.

4.3.2 Tests with synthetic data

To check the spatial resolution of the actual data set, I performed three different tests with synthetic data. In each test, the synthetic travel times were computed by 3D ray tracing through a synthetic model using the actual configuration of sources and receivers. To simulate real conditions I added random noise to the travel times with 0.2 s standard deviation similar to the real travel time residuals after the final inversion.

The reconstruction was performed using the same program codes and parameters as in the real case. I started with source localization accepting that the sources would be shifted from the "true" positions. After several iterations the algorithm shifted the sources close to their initial position and retrieved the velocity model.

Checkerboard test:

To check the horizontal resolution in different depths I performed a checkerboard test using the initial configuration of which is presented in figure 4.7 (lower left corner). The anomalies represent alternating high and low velocity blocks of $\pm 7\%$ amplitude. The horizontal block size is 30x30 km. The anomaly structure remained unchanged at all depths but the sign of the anomalies was reversed with 20 km depth spacing.

In figure 4.7 I show the reconstruction results for P- and S-wave velocity models at depth levels of 5, 20, 40 and 50 km. It can be seen that the P-wave velocity anomalies are well reconstructed in shape and amplitude beneath the entire study area. Up to the depth of 40 km the resolution is also good for the S-wave model. However, at deeper levels the resolution is lower for the S-waves due to the smaller number of events and subsequently poor ray coverage in the offshore part.

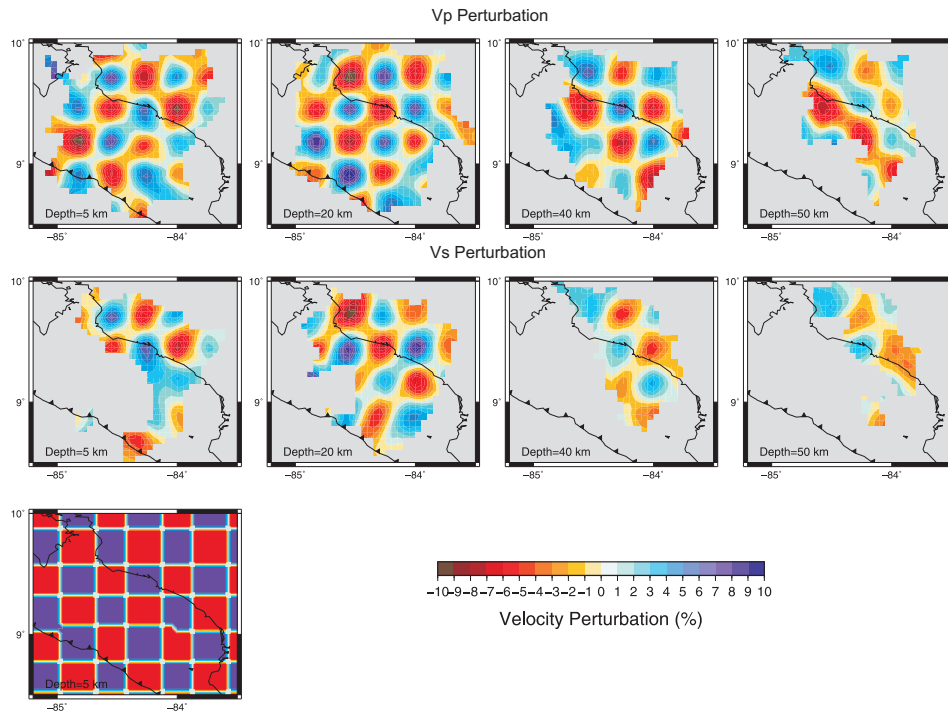


Figure 4.7: A checkerboard sensitivity test was performed to evaluate the resolution capability of the data set and sensitivity of the model. A 30x30 km grid size with an amplitude of $\pm 7\%$ was used for calculating the synthetic travel times (lower left corner). Calculated travel times were distorted using random noise with 0.2 s RMS for both P and S data. Upper row shows the reconstructed model for V_p and lower row shows the reconstructed model for V_s .

Simon Bolivar test:

To check the limitations of spatial resolution I performed a synthetic test with a portrait of Simon Bolivar (Fig. 4.8). This image (Fig. 4.8, upper left corner) contains both large and small wavelength anomalies so the reconstruction reveals information on the smallest patterns which can be resolved using the real observation system. The velocity distribution in the initial model remained unchanged at all depths. The synthetic travel times are calculated through this model using the real event and station configuration. The calculated travel times are distorted using a randomly distributed noise with 0.1s RMS. The obtained travel times and real source-receiver configurations are used to perform inversion. The 1D model given in table. 4.1 is used as an initial velocity model for the real inversion. The aim is to reproduce the portrait of Soimon Bolivar.

The reconstruction results for the depth of 15 km is shown for the first, second and fourth iteration. It can be seen that the face of Simon Bolivar is clearly recognizable after the first iteration. Even thin patterns such as the nose line, which is about 5 km wide, are clearly resolved. Both the Simon Bolivar and checkerboard tests show that the combination of data from three distinct networks did not cause a resolution problem in the overlap areas of the individual networks.

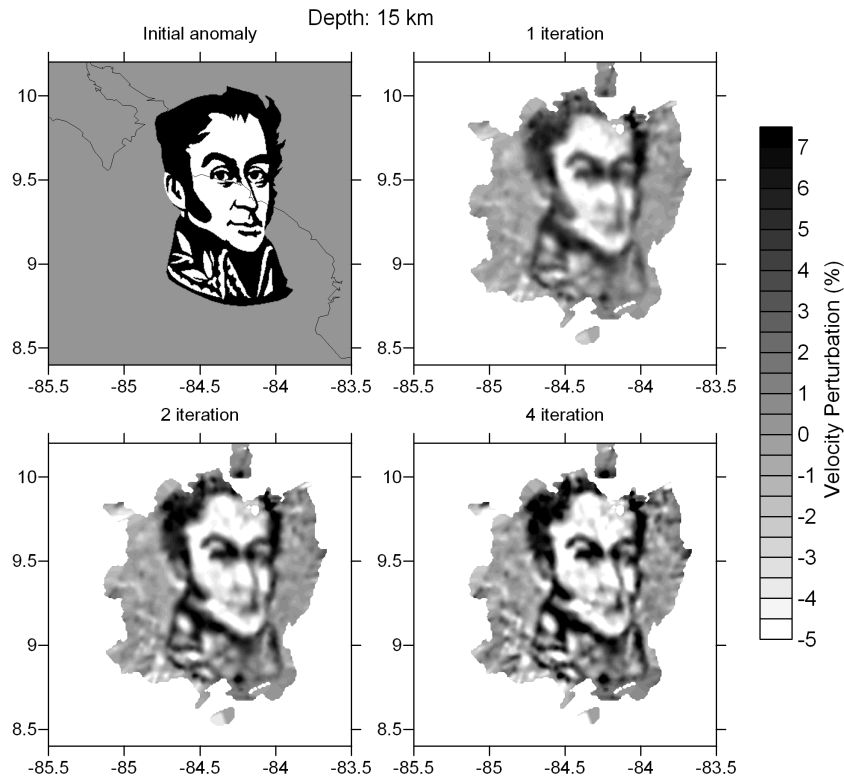


Figure 4.8: Simon Bolivar test. Upper left corner is the initial model for calculation of the synthetic travel times. The other three figures are the reconstructed models after the first, second and fourth iteration, respectively.

Resolution of realistic velocity anomalies:

The aim of the third test was to check how well the amplitudes of realistic velocity anomalies would be reproduced for a synthetic velocity model showing a similar subsurface structure as the Costa Rica subduction zone (Fig. 4.9 top, compare with Fig. 4.11, profile-2). The tomographic image (Fig. 4.9 bottom) reproduces shape and amplitude of the true model well. However, maximum reconstructed velocity amplitudes are about 2 % smaller than the amplitudes of the true model.

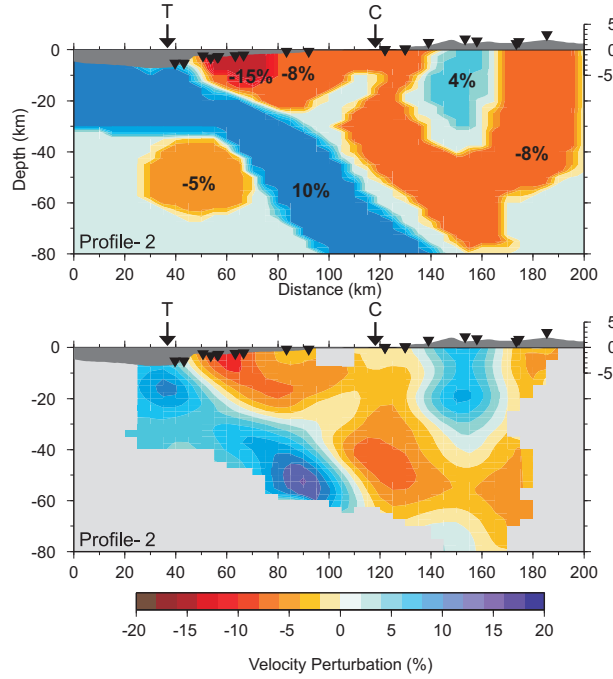


Figure 4.9: Synthetic test to check the vertical resolution with real anomalies. The upper row is the synthetic model showing the defined perturbations in percentage. The last row is the recovered model. The noise of 0.2 s RMS was added to the synthetic travel times. The result of reconstruction is identical with the real inversion case and reproduces the main patterns. T: trench; C: coast; triangles: stations.

4.4 Results of Tomographic Inversion

The tomographic inversion procedure was applied to the combined JACO, QUEPOS and RSN data sets. The 3D-inversion was terminated after 5 iterations. RMS travel time residuals were reduced from 0.31 s to 0.13 s for P-wave data and from 0.33 s to 0.14 s for S-wave data (Table 4.2). This corresponds to a RMS reduction of ~ 60 % for P-and S wave travel time residuals with respect to the 1D starting model. The tomographic results are presented in the form of vertical depth sections and horizontal depth slices. The vertical sections are arranged along profiles perpendicular and parallel to the trench

(Fig. 4.10). The figures show P-wave velocity perturbations (Fig. 4.11) relative to the 1D-reference model (Table 4.1), absolute P-wave velocities (Fig. 4.12) and V_p/V_s ratios (Fig. 4.15). Velocity perturbations are mostly used for interpretation because variations of the physical state of the materials are more easily seen. Hypocenters within a ± 10 km wide band are projected onto the vertical sections (Figs. 4.11, 4.12 & 4.15).

Table 4.2: Reduction of travel time residuals during 5 iterations of inversion procedure.

	1.iteration	2.iteration	3.iteration	4.iteration	5.iteration
P-RMS (s)	0.31	0.17	0.14	0.13	0.127
S-RMS (s)	0.33	0.18	0.15	0.14	0.137

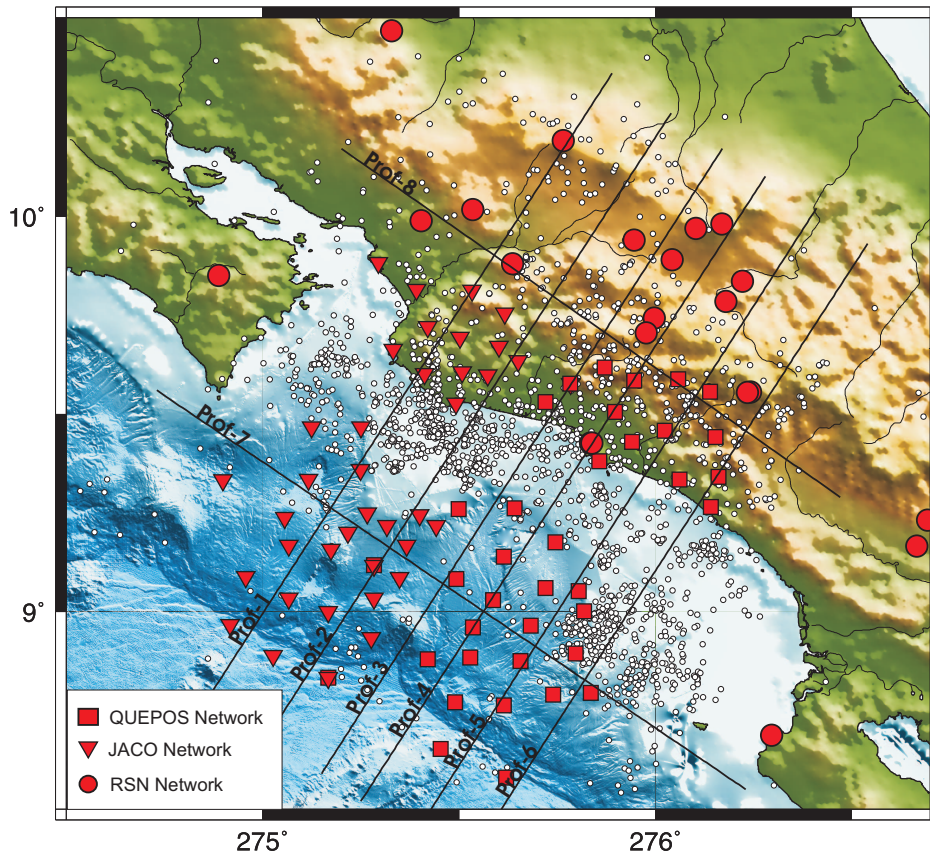


Figure 4.10: Distribution of the accurately located events after Local Earthquake Tomography. The lines show the profiles for vertical sections shown in Figs. 4.11, 4.12 and 4.15. White circles: events; red squares: stations of QUEPOS network; red triangles: stations of JACO network; red circles: stations of RSN network.

4.4.1 Seismicity

The seismicity observed in the vertical sections (Figs. 4.11, 4.12 & 4.15) can be classified in four groups. Specific clusters of seismicity are indicated in figure 4.12 and redrawn with index numbers in Fig. 4.13:

1. *Interplate seismicity* at crustal levels occurs between 10-30 km depths at 35-90 km distance from the trench. Enhanced earthquake clustering is found in the northern profiles 1&2 at about 20 km depth where the plate interface bends from 20° to 30° dip (point B and cluster 1a, Fig. 4.13). Further to the south, in profiles 3&4, this sort of clustering is significantly weaker. A special situation is found along profiles 6&7 where near-surface interplate seismicity is weak but a dense pattern of linearly aligned events extends within the forearc from the surface down to 20 km depth (cluster EQ in Fig. 4.13). This pattern represents the aftershocks of the M=6.9 earthquake of 20 August 1999. It starts at the bending point of the plate interface at 20 km depth and lines up to the surface with 40° dip in straight prolongation of the deeper plate interface. Interplate events are found closer to the trench (cluster 1b in Fig. 4.13) where they line up more steeply than in the north according to the more complicated plate geometry.
2. The *Wadati-Benioff-zone (WBZ)*, understood as the plate interface at mantle level, can be followed in the whole area of the network down to a depth of 80 km and up to maximum distances of 110-150 km from the trench (clusters 2a and b). At about 20 km depth all sections show a bending point of the plate interface below which the dip remains constant (B in Fig. 4.13). Laterally, however, the dip angle of the WBZ seismicity increases from 30° in the north to 45° in the South (profiles 1 to 6) showing an abrupt change between profiles 3 and 4. Generally, the density of seismic events observed in the WBZ is lower in north-western than in south-eastern Costa Rica.
3. Within the *overriding plate*, seismicity appears in zones of aligned events connecting the WBZ to the volcanic arc. Along the northern profiles 1 to 3 these linear clusters seem to form 20°S dipping parallel fault planes extending from a depths of 20-30 km up into the forearc and to the volcanic chain at the surface (cluster 3a). Along the southern profiles 5&6 the seismicity cluster forms criss-cross lineaments of 35° dip which could be interpreted as conjugate thrust planes (cluster 3b). This type of seismicity starts near the WBZ at a depth of 40-50 km and extends obliquely towards the Talamanca range. Along profiles 3&4, which cover the transition from the active volcanic chain to the presently volcanically inactive Talamanca range, pattern 3a and 3b seem to interfere.

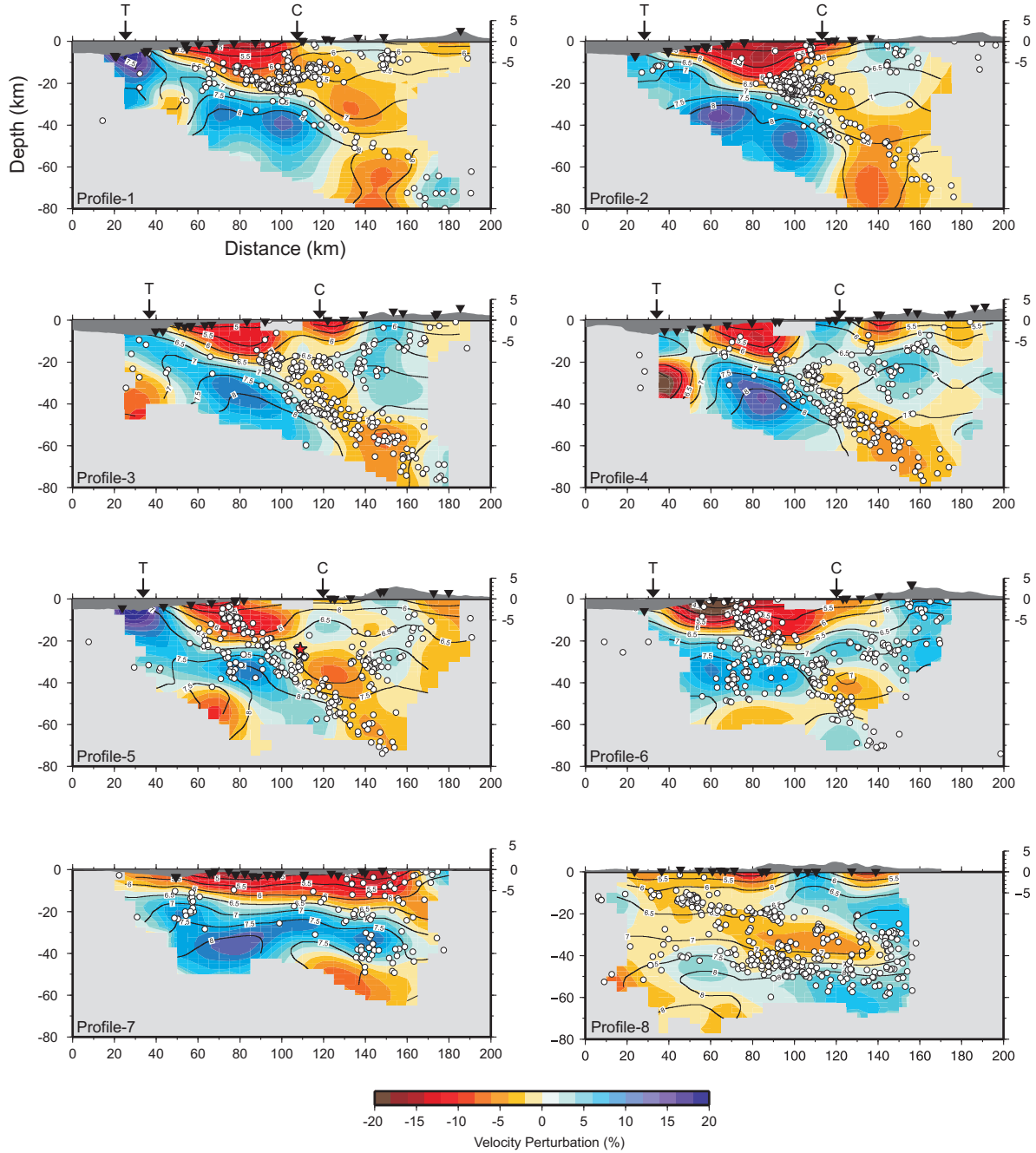


Figure 4.11: Cross-sections of the convergent margin of central Costa Rica showing seismicity and P-wave velocity perturbation corresponding to the reference model in table 4.1. Location of all cross-sections see Fig. 4.10. Black triangles = seismic stations; white circles = earthquake hypocenters; red star indicating August 20, 1999, Quepos earthquake, Mw=6.9; T = trench; C = coast; contour lines indicate absolute P-wave velocities with contour interval 0.5 km/s.

4. *Seismicity within the subducting plate* was found on sections 5&6 in a linear cluster extending from the plate interface into the subducting plate (cluster 4, Fig. 4.12). It dips 45° SE starting near the bending edge of the plate interface at 20-30 km

depth. It seems to cut about 40 km deep into the inclined slab and appears like a conjugate fracture pattern of the aftershock sequence of the M=6.9 earthquake of 20 August 1999 (Fig. 4.11).

In summary, between the NW and SE sections of the investigated area I observe significant differences in the geometry of the plate interface and in the forearc seismicity patterns. An abrupt structural change occurs between profiles 4 and 5 indicating the transition from the volcanic province to the non volcanic Talamanca province connected with the transition to a compressional tectonic regime.

4.4.2 Seismic velocity model

Regarding the 3D-seismic velocity models (Figs. 4.11, 4.12, 4.13, 4.15 & 4.16) the following observations can be drawn:

1. The top of the cold *subducting Cocos Plate* is associated with a positive P-wave velocity anomaly of maximum 10 % dipping parallel to the Wadati-Benioff-zone below Costa Rica (Fig. 4.11). The top of the zone is clearly defined by the upper envelope of the interplate seismicity. In most vertical sections it is connected with a transition from positive to negative velocity found between 5 % and -5 % with respect to the background model (Table 4.1). The surface of the high velocity zone is not smooth and shows several step structures. This is particularly evident on profiles 5 & 6 where the step structure seems to be connected with an extension of seismicity into the subducting plate (cluster 4, Fig. 4.13).
2. I observe a *thickening of the mantle wedge and oceanic lithosphere* from northwest to southeast Costa Rica evident from profiles 7 & 8 (Fig. 4.11) which is parallel to the Middle America Trench. The perturbation of 0 to -5 contour level starts at ~ 8 km depth in the north and reaches to ~ 20 km depth in the south. This structural change reflects the transition from the subducting seamount province to the Cocos Ridge in the south.
3. Within the *deep crust and upper mantle wedge* an increase in V_p/V_s ratio is found from SE to NW (Fig. 4.15 and Fig. 4.16 depth slices at 30 and 40 km). The transition occurs in the form of a rather sharp contrast along a line which can be correlated with the Central Costa Rica Deforming Belt (CCRDB) (Fig. 2.1).
4. One major feature of the *forearc* is a zone of low P-velocity in the uppermost 10 km between the trench and the coastline (Fig. 4.11 & 4.12). Since the Costa Rica margin is erosional it can be interpreted as the fractured part of the margin

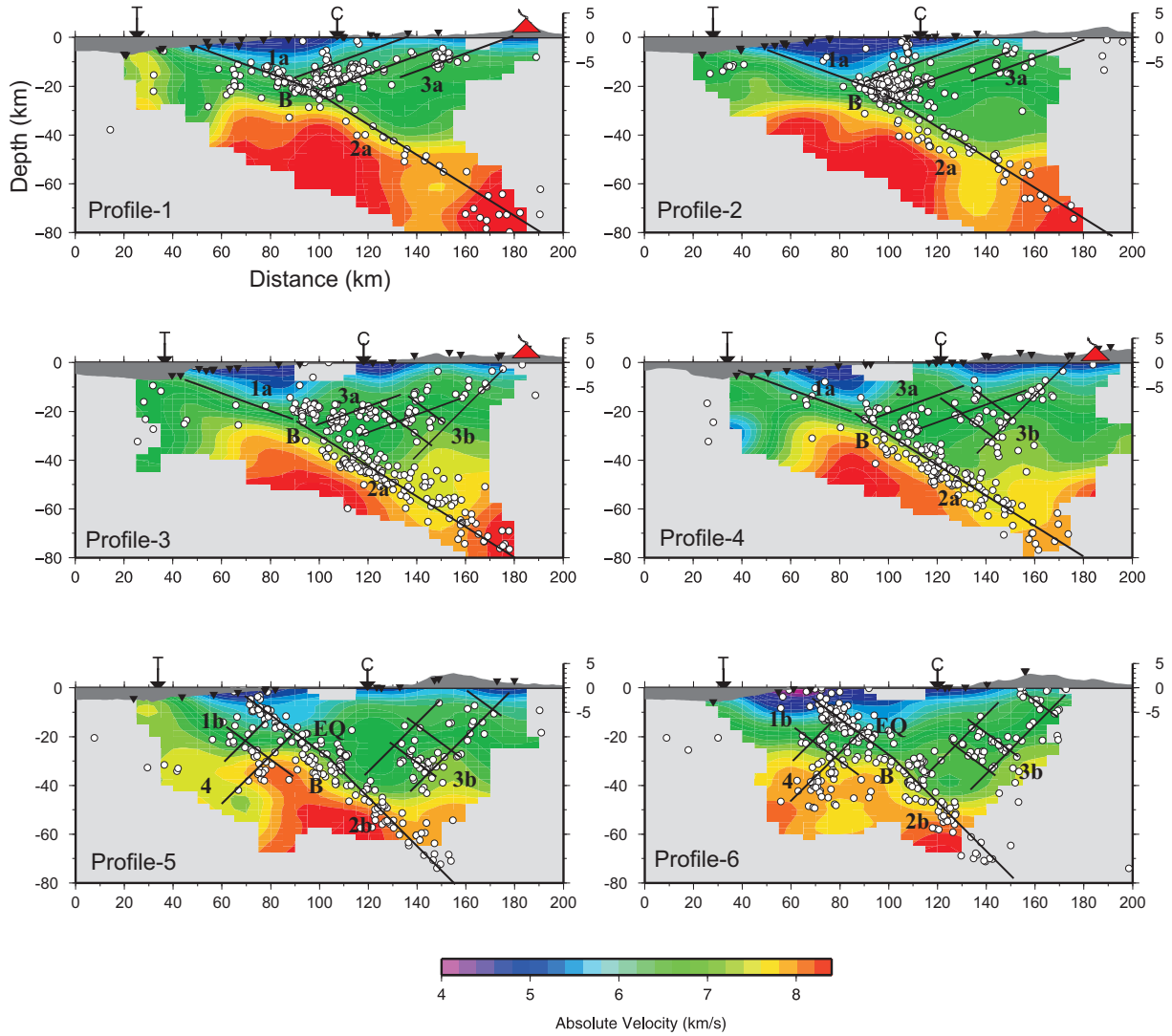


Figure 4.12: Cross-sections of the convergent margin of central Costa Rica showing seismicity and corresponding absolute P-wave velocities. Location of all cross-sections see Fig. 4.10. Black triangles = seismic stations; white circles = earthquake hypocenters; red triangles = volcanoes; T = trench; C = coast. Solid black lines = faults and plate interfaces. 1a,b: seismogenic zone; 2a,b: Wadati-Benioff zone; 3a,b: internal deformation zone; 4: oceanic mantle deformation; EQ: hypocenters of aftershocks of the Quepos earthquake (red star in Fig. 4.11); B: bending point of the downgoing plate and transition to the Wadati-Benioff-Zone.

wedge with a high fluid content rather than as an accumulation of sediments. This interpretation is consistent with the observed increase in the V_p/V_s ratio (Fig. 4.15) and numerous seismic measurements and wide-angle profiles (e.g. Hinz et al., 1996; Ye et al., 1996; von Huene, 1995; von Huene et al., 2000).

5. The *deep crust of the overriding plate* is characterized by a sequence of basement highs and lows rather than by a layered appearance. This is obvious mainly from

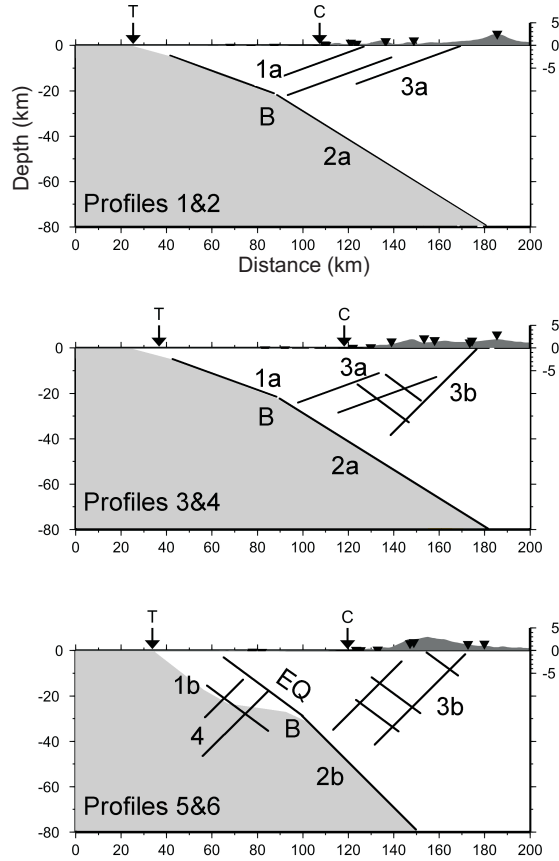


Figure 4.13: A tentative schematic tectonic interpretation based on seismic distribution of Fig. 4.11 and 4.12. Solid black lines = faults and plate interfaces. 1a,b: seismogenic zone; 2a,b: Wadati-Benioff zone; 3a,b: internal deformation zone; 4: oceanic mantle deformation; EQ: hypocenters of aftershocks of the Quepos earthquake (red star in Fig. 4.11); B: bending point of the downgoing plate and transition to the Wadati-Benioff-Zone.

the plots of absolute P-wave velocity (Fig. 4.12). The high-velocity lower crust seems to form a tilted block with a sharp velocity transition or discontinuity at about 20 km depth. A comparison with an active seismic profile (Stavenhagen, 1998) located close to our profile 6 shows that the Moho can be associated most probably with the 7.4 km/s velocity contour at about 40 km depth.

6. Beneath the *volcanic arc* the resolution of the tomograms is low. Nevertheless, the results indicate a low P-wave velocity anomaly at the Poás and Irazú volcanoes (profiles 1 and 4 in Fig. 4.11) which can be correlated with the partial melting and upwelling of magma. A corresponding anomaly of the V_p/V_s ratio could not be identified because the S-wave velocity structure is not resolved well enough towards the edge of the investigated area.

4.5 Discussion and Conclusion

4.5.1 The seismogenic zone and slab geometry

The seismogenic zone and slab geometry of central Costa Rica exhibit significant spatial variation corresponding to the spatial change of the incoming plate. The general trend shows a steepening of the plate interface towards the south (Fig. 4.14) and an increasing complexity of the plate contact (Figs. 4.11 to 4.14). Our investigation area covers three sections which can be characterized in terms of the geometry of seismicity patterns and P-wave velocity structure as follows:

1. In the northernmost section (profiles 1&2 in Figs. 4.11 to 4.15), corresponding to the incoming seamount province, the subducting plate interface shows a dip angle of 30° at 20-60 km depth indicated by a sparse homogeneous pattern of earthquakes. In addition a dense seismicity pattern occurs in the upper overriding plate at depths of less than 25 km. It may be related to the transcurrent fault system of the Central Costa Rica Deforming Belt (CCRDB). This fault zone is assumed to be caused by the transmission of shear stress coupled into the overriding plate through the rough surface of the subducting plate (Colombo et al., 1997). Generally, profiles 1&2 are similar to the findings of DeShon et al. (2006) in the area of the Nicoya Peninsula neighboring in the north.
2. The central section (profiles 3&4) coincides with the southern part of the CCRDB. The subduction angle and seismicity at the plate interface are still similar to the northern section but a clear change is observed in the spatial distribution of events in the overriding plate. Compared to profiles 1&2, where the shallow events seem to follow oblique planes, the geometry of these patterns is less clear. It can possibly be understood as a combination of the patterns found in the north and south sections indicating an interference of the different stress mechanisms found in the north and south of the central section.
3. The southern section of the investigated area (profiles 5&6) is influenced by the subduction of the northern edge of the Cocos ridge. It differs significantly from the previous sections in both slab geometry and seismicity. In the upper 20 km the plate interface is nearly horizontal. Between 20 and 60 km depth the slab gets steeper and again shallower forming a stair-shape cross-section (Fig. 4.13). Between 40 and 60 km depth, a constant final dip angle of about 45° is observed. In previous studies only the shallow dip of the upper part of the subducting plate had been recognized and usually interpreted as an underplating feature (Husen et al., 2003; Protti et al., 1999). Our results show that the situation is probably

more complicated: The subduction seems to continue to deeper levels and with a steeper angle than previously thought, and the stair-shaped plate interface couples plate motion more intensely than a smooth interface would do. Compared to the northern section the average stress transfer seems to occur more horizontally leading to a collision style setting with $\sim 45^\circ$ dipping conjugate fault planes in the overriding plate. This view seems to be confirmed by the uplift of the Talamanca as such and by the aftershock pattern of the 1999 M 6.9 earthquake (EQ in Fig. 4.11). This aftershock plane terminates approximately at the step of the stair-shaped plate interface at ~ 25 km depth. This coincidence could indicate that this structural heterogeneity of the plate interface may have caused a local stress accumulation later-on released in the 1999 earthquake.

4. The velocity structure of the subducted plate is only weakly constrained by the travel time data because most hypocenters are located near its surface. Nevertheless, the tendency of a decrease in P-wave velocity from northern to southern Costa Rica is observed. This is probably caused by the higher age and lower temperature of the oceanic lithosphere subducting beneath northern Costa Rica.

4.5.2 Lateral change in the slab geometry

The lateral change in the slab geometry can be caused by the convergence rate of the incoming plate, the density contrast and thickness of the incoming and overriding plates, pulling forces of the subducted plate portion, and friction and deformation in the contact zone. A quantification of these forces in form of a modeling study is beyond the scope of this study, but some aspects can be discussed: The convergence rate of the incoming plate is approximately constant in the investigation area (about 9.3 cm/y (DeMets, 2001)). Future modeling of the gravity field will have to show in how far the seismic velocity decrease observed in the incoming plate from N to S is correlated with a density decrease. A density decrease, however, would imply higher buoyancy in the south which would not be compatible with the observed steepening of the subducting plate interface. Besides age differences also compositional changes of the subducting lithosphere have to be considered: In the northern segment of our investigation area the incoming plate shows many seamounts and trench parallel fractures, possibly connected with serpentization, which could lower the density (Ranero et al., 2003) and cause uplift in the overriding plate (von Huene et al. 2004b). The southern section is influenced by the Cocos Ridge with its thickened crust, and it is unclear which of these factors has a stronger effect on local buoyancy. Phase changes related to lateral compositional changes within the slab may also cause lateral variation in slab pull (Zhang and Kayal, 2000). However, in summary, plate convergence, buoyancy considerations as well as lateral P-wave velocities

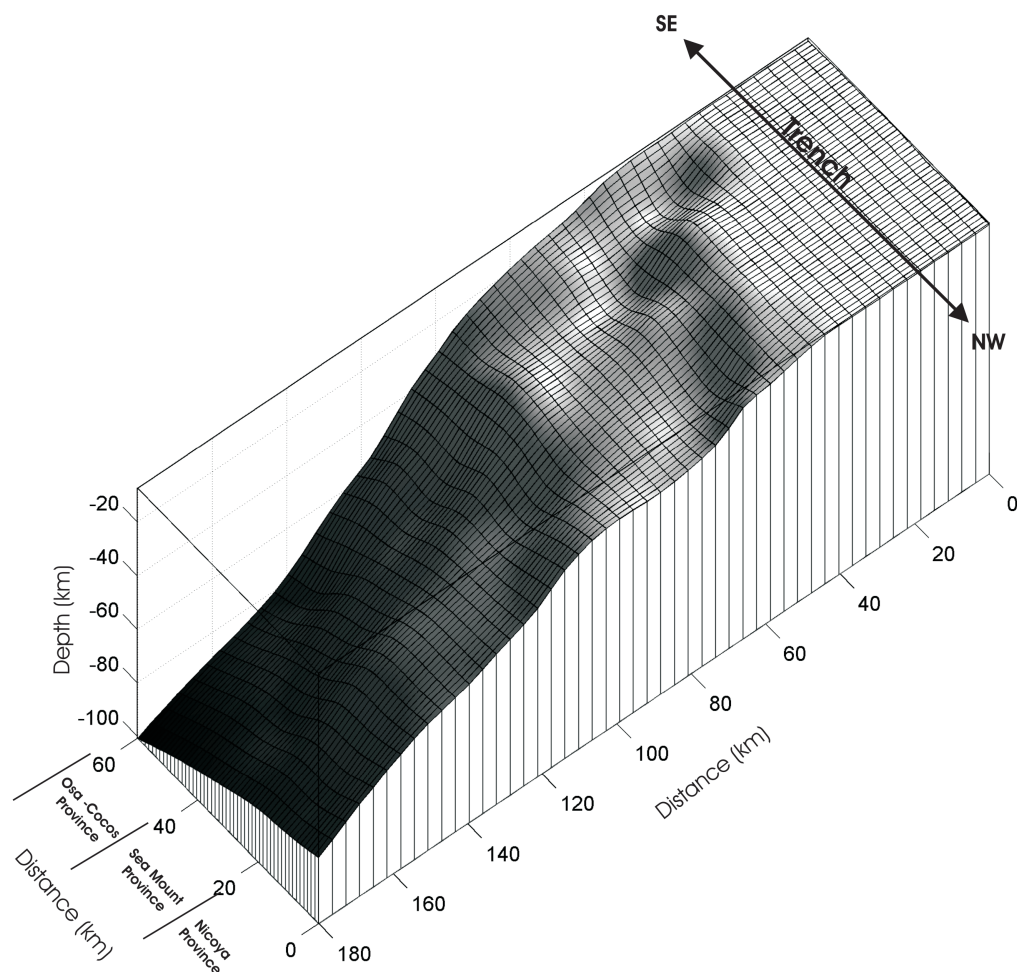


Figure 4.14: Flying carpet showing the lateral structural changes. Zero perturbation contour which is almost the upper envelope of the slab are digitized for all the vertical sections (Fig. 4.10) perpendicular to the MAT. The data in between is interpolated by the MATLAB 4 griddata method.

do not offer an obvious explanation for the dip increase of the plate interface. Rather, the complexity of the P-wave velocity model near the plate interface and the seismicity patterns seem to indicate that the dip change could be understood as a consequence of changes in plate coupling and related deformation.

4.5.3 Evidence of fluid transport

The intermediate depth earthquakes of central Costa Rica are supposed to be triggered by dehydration (Hacker et al., 2003; Husen et al., 2003). Husen et al. (2003) calculated the predicted dehydration depth of hydrous minerals depending on Hacker et al. (2003) from onshore central Costa Rica, along a profile close to the profile-2 of this study. Most

of the mineral dehydration depths correspond well to the distribution of the intermediate depth earthquakes. P-wave tomography shows a low velocity zone in the mantle wedge at about 40 km depth (Fig. 4.11) which would correspond to a very low local mantle V_p (about 7.2-7.4 km/s) possibly indicating hydration of the mantle wedge. The P-wave velocity is lower on profiles 1-3 than on profiles 4-6 indicating that the fluid input into the mantle wedge is higher in the fractured seamount province than in Cocos Ridge area. Further evidence of fluid transport through the crust may be seen in the seismicity patterns connecting the plate interface to the forearc and arc along profile 1 to 3 (pattern type 3a in Fig. 4.13). These patterns may represent a fault system through which fluids released from subducted rocks can rise up to the volcanic arc.

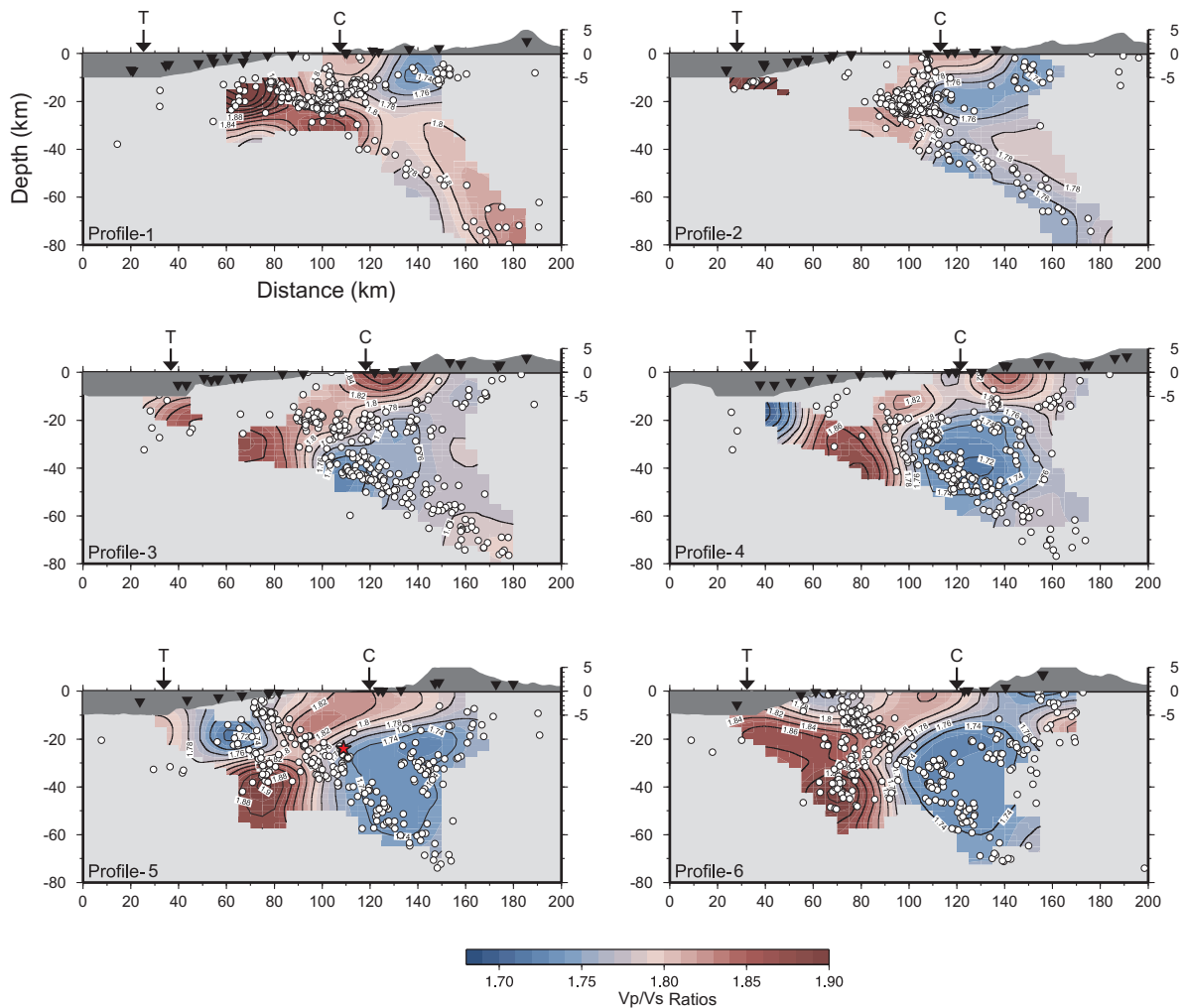


Figure 4.15: Cross-sections through V_p/V_s ratios. Earthquakes (white circles), stations (black triangles), trench(T) and coast (C) are projected on to the sections. Red star indicates the August 20, 1999, Quepos earthquake, $M_w=6.9$. Profiles are displayed in Fig. 4.10.

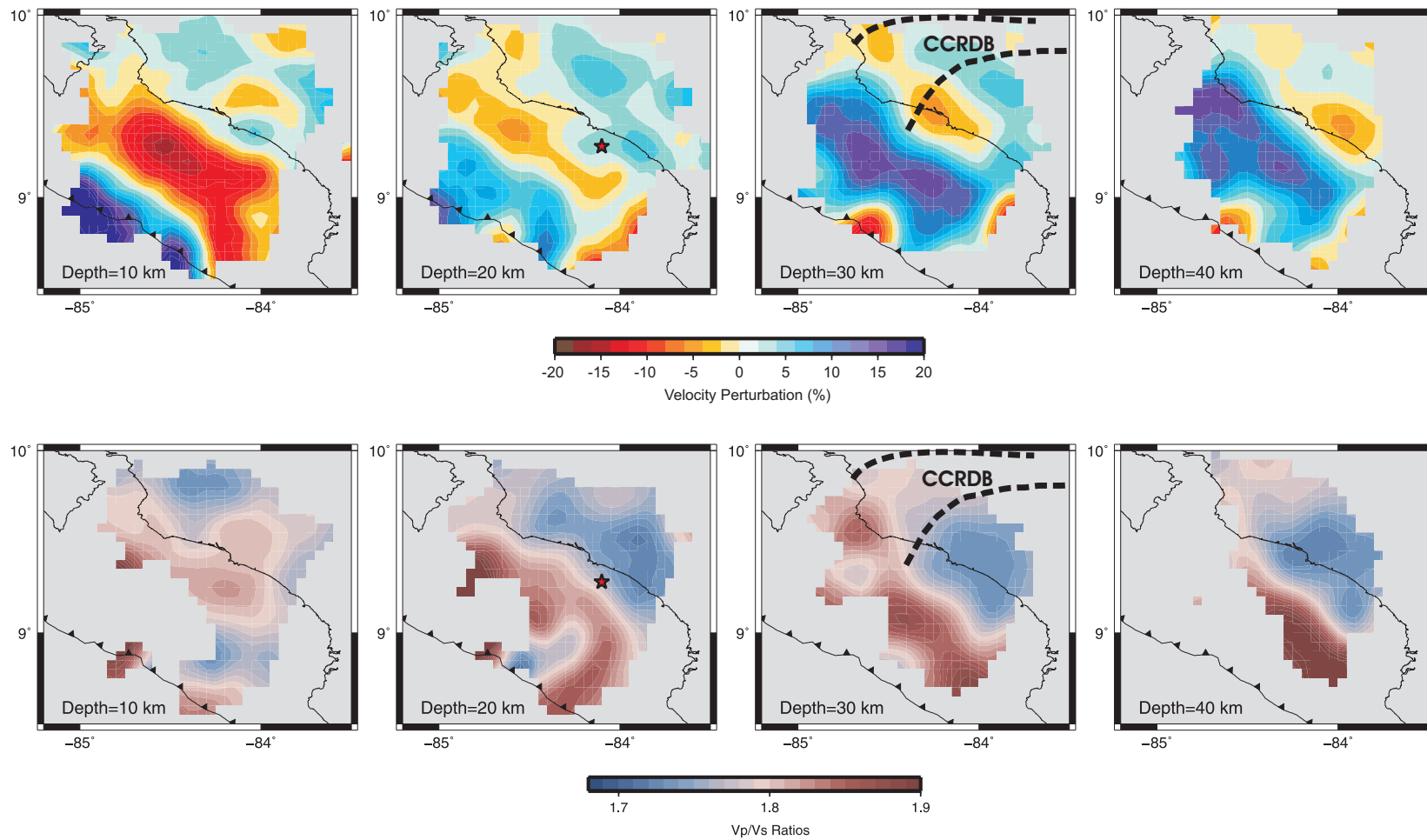


Figure 4.16: Horizontal depth sections of V_p perturbations (upper row) and V_p/V_s ratios (lower row) after the inversion. The reference model (background model) is given in table. 4.1. V_p perturbations show the lateral variation of the subduction zone. The star indicates the August 20, 1999, Mw=6.9 Quepos earthquake. Location of Central Costa Rica Deforming Belt (CCRDB) indicated by dashed lines.

4.5.4 Costa Rica Deformation Belt

The active part of the Costa Rican volcanic arc terminates at the Central Costa Rica Deforming Belt (CCRDB). Beneath the CCRDB a significant contrast in P-wave velocity and V_p/V_s ratio reaching down to 40 km depth (Fig. 4.15) is found. Therefore, the CCRDB, separating the northwestern and southeastern parts of Costa Rica, can be interpreted as a major crustal transition zone connected also with the beginning gap of the volcanic chain in the south. Again, this transition zone can be understood as the result of the changing structure of the incoming plate with the fractured dewatering seamount province in the NW and the Cocos Ridge in the SE causing a thickening of the overriding plate and transferring a smaller amount of water into the mantle wedge beneath the Talamanca. Beneath the active part of the volcanic arc an increased V_p/V_s ratio of 1.8 is found at 30 km depth (Fig. 4.15). Most of the crustal earthquakes are found in the transition zone from high to low V_p/V_s values attributed to the CCRDB which, therefore, has to be regarded as a highly deformed region down to depths of 30 km.

Chapter 5

Southern Nicaragua/Northern Costa Rica

5.1 Introduction

Mantle wedge hydration caused by fluids derived from the subducting slab is believed to control the downdip limit of the seismogenic zone (e.g. Hyndman et al., 1997; Peacock and Hyndman, 1999). It seems to be influenced by various parameters, such as the age of the incoming plate, dip of the plate interface, volume of the subducted sediment, rate of the convergence, thickness of the overriding crust (Oleskevich et al., 1999; Hyndman et al., 1997; Peacock and Hyndman, 1999), and stress state of the overriding plate (Seno, 2005; Heuret et al., 2007; Heuret and Lallemand, 2005). The downdip limit of the seismogenic zone is important for the generation of megathrust earthquakes because it determines the length of the rupture zone in the landward direction. In the relatively warm subduction zones of Cascadia (Bostock et al., 2002; Brocher et al., 2003) and SW Japan (Kamiya and Kobayashi, 2000) this limit coincides with the mantle wedge corner and an aseismic zone explained by the slippery behavior of serpentine at the contact between the subducting oceanic crust and the overriding forearc mantle (Bostock et al., 2002; Kamiya and Kobayashi, 2000; Brocher et al., 2003; Zhang et al., 2004). In the cold subduction zones, the lack of mantle wedge hydration can be explained by the existence of a thicker continental crust. In such a case, the major part of the water goes into the forearc crust rather than into the forearc mantle (Hyndman and Peacock, 2003). The hydration process is further more important because the hydrated forearc mantle represents a big reservoir in the global hydrologic cycle (Zandt, 2002) and may provide water for forearc volcanism or lubricating faults (Brocher et al., 2003).

The degree of the mantle wedge hydration depends on the amount of water that is carried

with the incoming plate down to greater depths. The initial hydration of the subducting crust and mantle is thought to take place near the mid-ocean ridges and near the trench along bend-related faults, representing a reservoir of fluids and fluid rich sediments. The release of fluids in dehydration reactions can trigger intermediate depth earthquakes in the uppermost part of the slab (Hacker et al., 2003; Ranero et al., 2003; van Keken, 2003), creating pathways for water into the overriding mantle wedge (Husen et al., 2003; Hacker et al., 2003; Hasegawa and Nakajima, 2004; Carlson and Miller, 2003).

Recent seismic investigations have shown that the incoming plate of the Nicaraguan convergent margin is highly hydrated. The hydration corresponds to an almost uniformly dense pattern of normal faults that are extending all along the bending Cocos Plate near the trench offshore Nicaragua and north Costa Rica. In contrast, the overriding plate shows clear geological changes from the northwest to the southeast, shown in Fig. 2.1. For example, a deep forearc, intra and backarc basins are found in Nicaragua but are absent in northern Costa Rica (McIntosh et al., 2007). The active volcanic front of Nicaragua shows a marked landward displacement coincident with the political boundary of Nicaragua and Costa Rica. High concentrations of ^{10}Be and B/La are found at the volcanoes in the Nicaraguan section while the concentrations are low in Costa Rica (Noll et al., 1996; Patino et al., 2000; Hoernle and Hauff, 2007). Since lateral variations of the incoming plate seem not to exist, these changes should be caused mainly by the structure, composition and tectonics of the overriding plate. Considered together, these findings suggest that the continental margin of Nicaragua and N Costa Rica is an excellent site to study the interplay of the dehydration of the downgoing plate, the (possible) hydration of the mantle wedge and the influence of tectonics and structure of the overriding plate.

I approach this theme by applying a joint on- and offshore local earthquake tomography. I present P- and S-wave tomographic images and hypocenter locations from a temporary network leading to an improved view of the deep water cycle at subduction zones.

5.2 Data Base

An amphibious seismic network was operated off- and onshore N Costa Rica and S Nicaragua between December 2005 to June 2006, involving 20 Ocean Bottom Seismometers and 30 land seismic stations. Ten of the marine stations were only hydrophones and 10 of them were equipped with seismometers (IFM-Geomar type OBS as described by Bialas and Flueh (1999)). The land stations were short period Mark-L-3D seismometers with Earth Data Logger (EDL) recorders provided by the geophysical instrument pool of GFZ, Potsdam. Figure 5.1 shows an example of an event recorded at several stations. Figure 5.2 & figure 5.3 give example how the picking procedure was performed. During

the observation period more than 1000 events were recorded (Fig. 5.4).

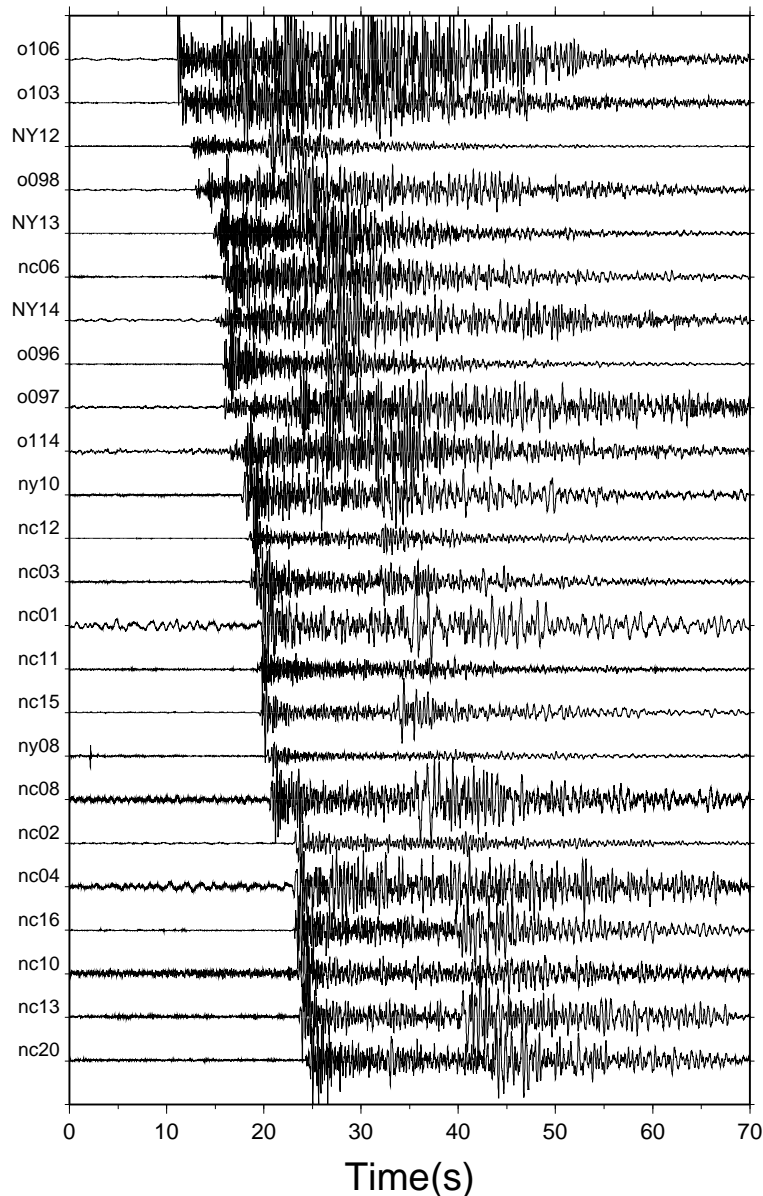


Figure 5.1: Example recording of an event that occurred on 10.12.2005 at 10:47:54. Hydrophone components of the ocean bottom stations and vertical components of the land stations are displayed.

For the tomographic inversion the data set was edited on the basis of a preliminary hypocenter localization with a 1D-velocity model and of the following criteria: (1) each event observed at a minimum number of 5 stations or more; (2) horizontal distance to the nearest station of the network < 50 km. Applying these criteria, 860 earthquakes of high signal-to-noise ratio with 10770 P-phase and 6898 S-phase readings were used to perform local earthquake tomography (Fig. 5.8). The optimum 1D background model

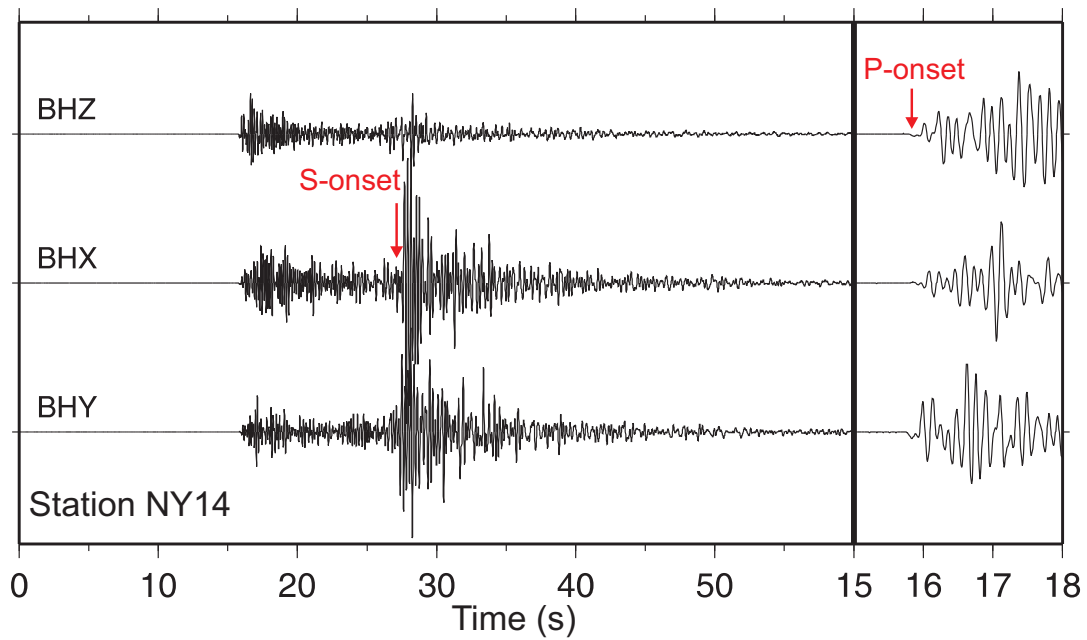


Figure 5.2: Example recording of the event in Fig. 5.1 at the 3 component land station NY14. The P-wave onsets are picked from the vertical component (BHZ) and the S-wave onsets are picked from the lateral components (BHX or BHY).

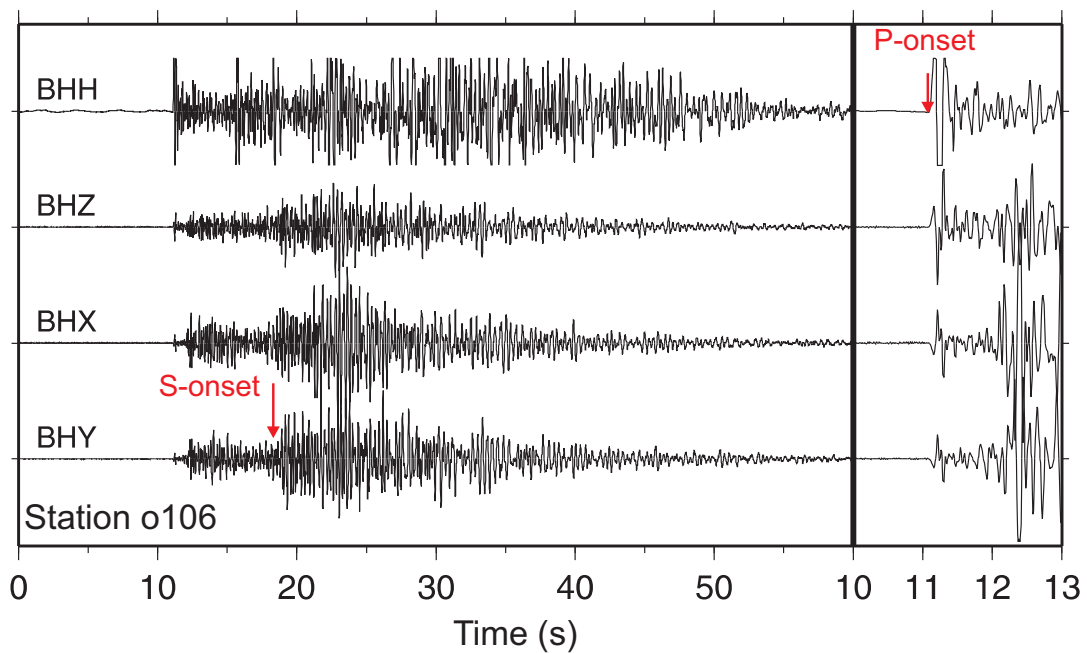


Figure 5.3: Example recording of the event in Fig. 5.1 at the 4 component sea station OBS106. The P-wave onsets are either picked from the hydrophone (BHH) or vertical component (BHZ). The S-wave onsets are picked from the lateral components (BHX or BHY) of the seismometers.

consisting of constant velocities is given in table 5.1 which is used for the preliminary location of the events and as an initial model for the 3D inversion. The optimization of the 1D model was performed using the VELEST program. Several inversions were performed following the Kissling et al. (1994) to obtain the optimum 1D velocity model for the region.

Table 5.1: Background model of V_p and V_s applied in the tomographic inversion.

Depth (km)	V_p (km/s)	V_s (km/s)
0.0	2.40	1.34
10.0	4.29	2.41
16.0	6.30	3.53
19.0	6.88	3.86
22.0	7.00	3.93
41.0	7.90	4.43
80.0	8.20	4.60
124.0	8.35	4.69
310.0	8.66	4.92

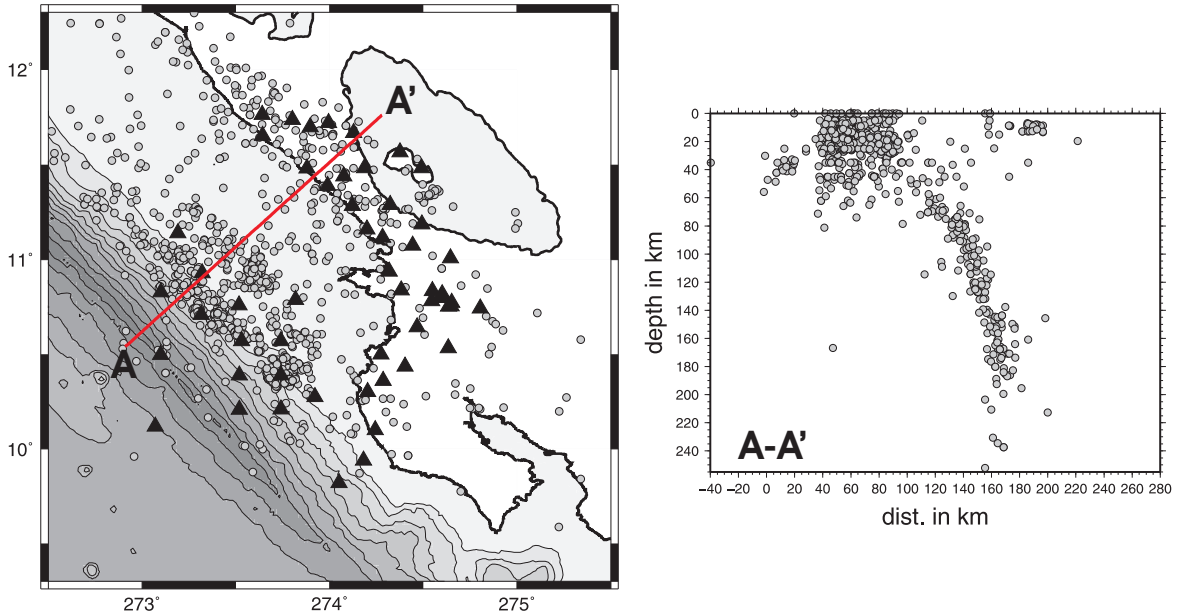


Figure 5.4: Seismicity of Nicaragua recorded from December 2005 to June 2006 (left). Depth distribution of events along profile A-A' (right)

5.3 Resolution Tests

In order to show that the tomographic inversion produces reliable images of the real structures I investigated the stability of inversion results with respect to a random selection of input data (Section 5.3.1) and performed two different tests of spatial resolution based on synthetic data (Section 5.3.2).

5.3.1 Test with random selection of events

In order to investigate the influence of random noise in the real travel time data, I performed independent inversions for two randomly separated data subsets. The subsets were selected by choosing events with either odd or even identification numbers. In the case of a strong noise influence the correlation between the different results should be low. The results are presented in two vertical and one horizontal sections corresponding to the independent inversion of data sets with odd, even and all events in figure 5.5. It is obvious that the prominent features are recognizable in all subsets. Even small patterns in the coastal area are robustly retrieved with both data subsets. The test shows that the noise in the data has negligible effect on the stability of the results.

5.3.2 Tests with synthetic data

The synthetic travel times were computed by 3D ray tracing through a synthetic model using the actual configuration of sources and receivers. To simulate real conditions I added random noise to the travel times with 0.2 s standard deviation similar to the real travel time residuals after the final inversion. The reconstruction was performed using the same program codes and parameters as for the real data: I started with source localization accepting that the sources would be shifted from the "true" positions. After several iterations the algorithm shifted the sources close to their initial position and retrieved the velocity model.

Checkerboard test:

To check the horizontal resolution in different depth I performed a checkerboard test. The initial configuration is presented in figure 5.6 (lower left corner). The anomalies represent alternating high and low velocity blocks of $\pm 7\%$ amplitude. The horizontal block size is 40x40 km. The anomaly structure remained unchanged at all depths but the sign of the anomalies was reversed with 50 km depth spacing. In figure 5.6 I show the reconstruction results for P- and S-wave velocity models at depth levels of 30 and 50 km which coincide with the mantle depths. It can be seen that the P-wave velocity anomalies are well reconstructed in shape and amplitude beneath the entire study area.

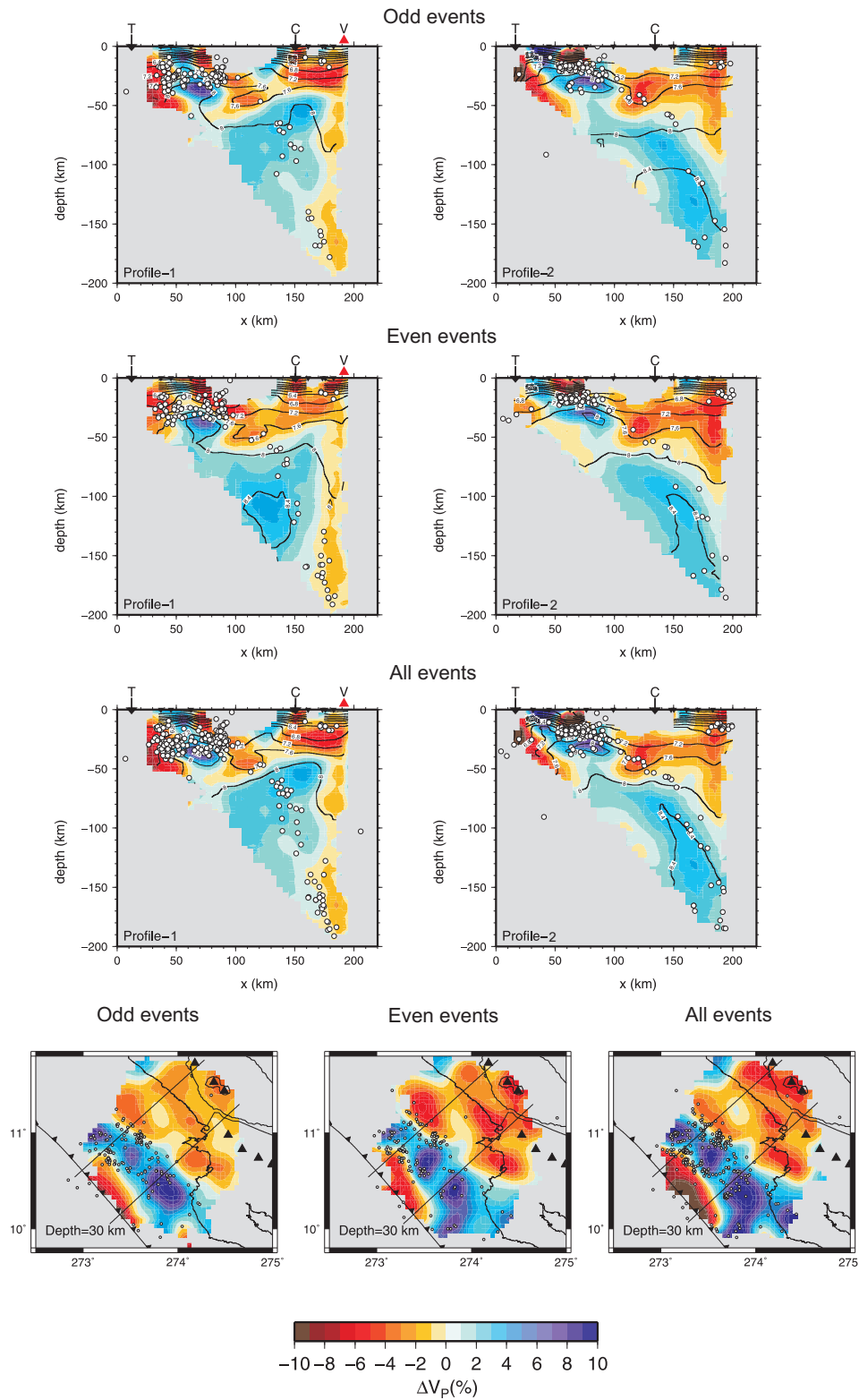


Figure 5.5: P and S velocity anomalies obtained from the inversion of odd, even number of events and all data set.

However, at deeper levels the resolution is lower due to the smaller amount of data and poor ray coverage.

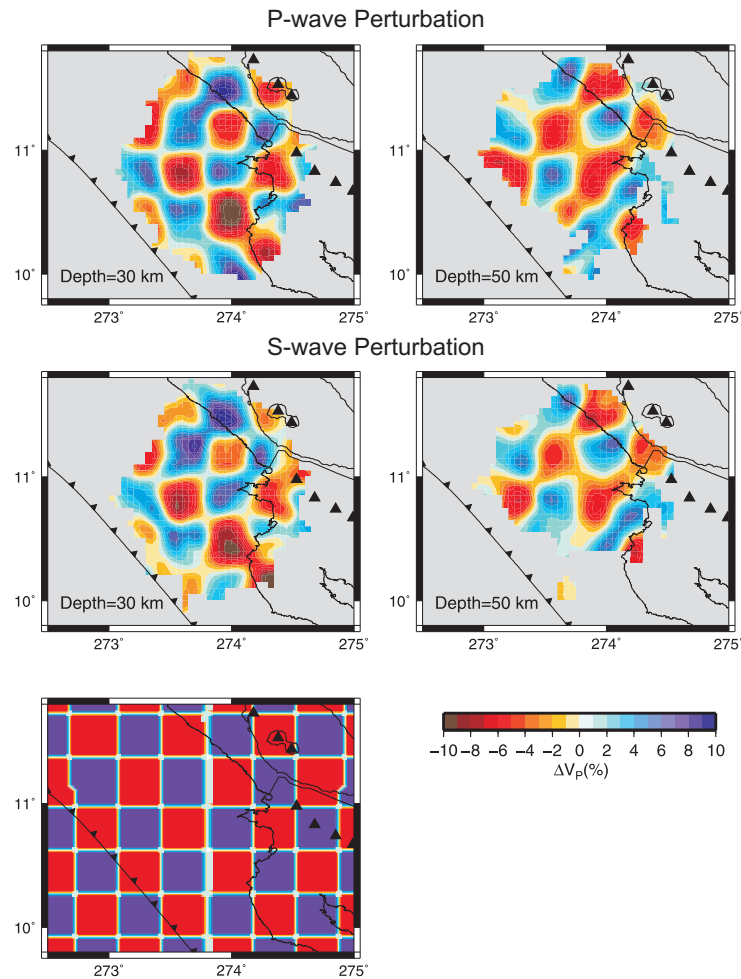


Figure 5.6: A checkerboard sensitivity test was performed to evaluate the resolution capability of the data set and sensitivity of the model for P-(upper row) and S-waves (middle row). A 40x40 km grid size with an amplitude of $\pm 7\%$ was used for calculating the synthetic travel times for P and S (lower left corner). Calculated travel times are distorted using random noise with 0.2 s RMS for both P and S data.

Resolution of realistic velocity anomalies:

The aim of this test is to check how well the vertical velocity anomalies would be reproduced for a synthetic velocity model showing a similar subsurface structure as the Nicaragua subduction zone (Fig. 5.7 top, compare with Fig. 5.9, profile-4). The tomographic image (Fig. 5.7 right) reproduces shape and amplitude of the true model well. However, maximum reconstructed velocity amplitudes are about 2 % smaller than the amplitudes of the true model in deeper parts, especially for the slab body.

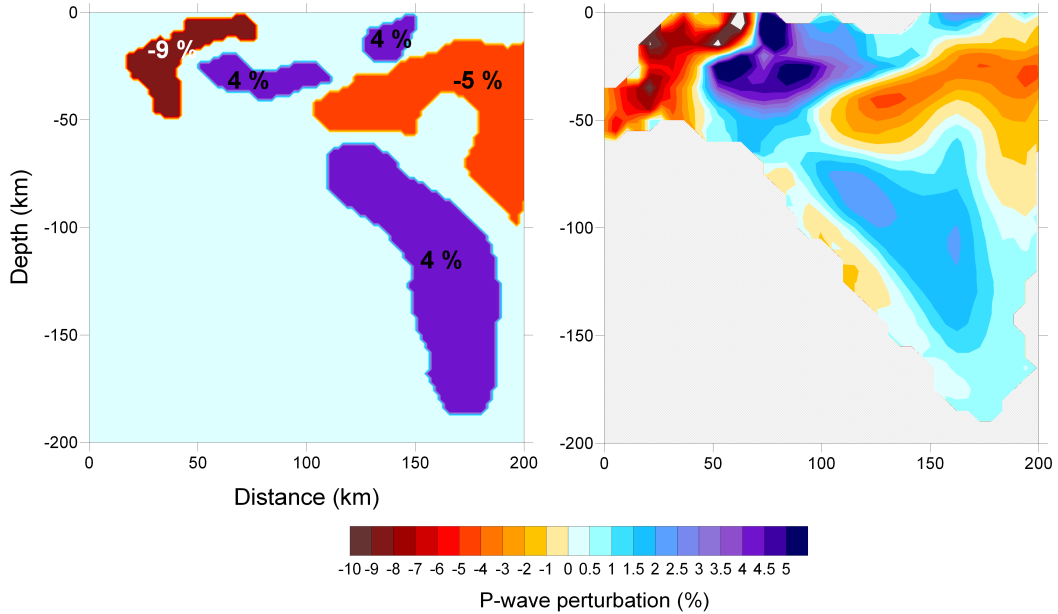


Figure 5.7: Synthetic test to check the vertical resolution with real anomalies. The left figure is the synthetic model, the right figure is the recovered model. The noise of 0.2 s RMS was added to the synthetic travel times. The result of reconstruction is identical with the real inversion case and reproduces the main patterns.

5.4 Results of Tomographic Inversion

The 3D-inversion was terminated after 5 iterations. RMS travel time residuals were reduced from 0.36 s to 0.22 s for P-wave data and from 0.73 s to 0.35 s for S-wave data (Table 5.2). This corresponds to a RMS reduction of 40% for P-wave and 52% for S-wave travel time residuals with respect to the 1D starting model.

Table 5.2: Reduction of travel time residuals during 5 iterations of inversion procedure.

	1.iteration	2.iteration	3.iteration	4.iteration	5.iteration
P-RMS (s)	0.36	0.28	0.24	0.228	0.219
S-RMS (s)	0.73	0.45	0.39	0.36	0.35

The following prominent features can be identified in the tomograms of Figs. 5.9. to 5.11:

1. The cold and dense slab appears as a dipping high velocity structure anomaly with a dip angle of 35° in the upper 60 km depth, which steepens to $\sim 70^\circ$ down to 200 km depth (Fig. 5.9). The top of the slab coincides with the upper envelope of the earthquake distribution. The dip of the slab gets shallower from north (38°) to

south (30°) in the upper 60 km depth. The dip angle does not change significantly in the deeper parts but the number of events decreases in these depths from north to south.

2. The mantle wedge corner of the overriding plate, found between 30-70 km depths at 100-150 km distance from the trench, shows a 4% decreased P-velocity with respect to 7.9 km/s and a high V_p/V_s ratio of ~ 2.0 . The zone of the high V_p/V_s ratios disappears from north (Nicaragua) to the south (Nicoya Peninsula, N Costa Rica), where it returns to the usual value of 1.7-1.8 (Figs. 5.9 & 5.10). The transition is well visualized in the horizontal sections (Fig. 5.11). While the low P-velocity anomaly extends and strikes almost uniformly parallel to the slab, I find that the high V_p/V_s ratio anomaly extending downwards beneath 30 km terminates abruptly at 274° E (Fig. 5.11). Therefore, a significant difference exists in V_p/V_s between Nicaragua and N Costa Rica. This transition occurs almost at the southern edge of the Sandino forearc basin and near the border between the Chortis and Chorotega blocks. Also, it coincides with a line between the Madera volcano (Nicaragua) and Orosi volcano (N Costa Rica) along which the volcanic chain shows a displacement of about 25 km (dashed line in Fig.5.11).

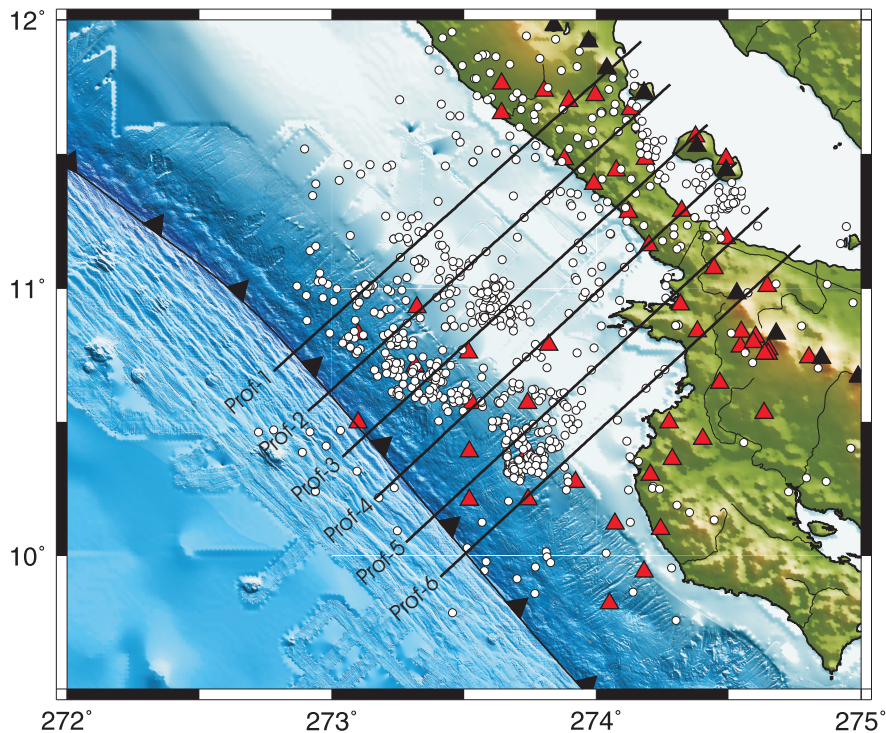


Figure 5.8: Distribution of the events used for Local Earthquake Tomography. The lines show the profiles for vertical sections shown in Fig. 5.9 and Fig. 5.10. The white circles denote the earthquakes located after 3D inversion. The red triangles indicate the seismic stations. Black triangles are the volcanoes.

3. A slight difference of 0.05 in V_p/V_s is found between the N and S sections of the dipping oceanic mantle. Lower values are found in the south.
4. I find a zone of 4% decreased P-wave velocity and increased V_p/V_s -ratio, which starts at the the mantle wedge corner and continues upwards until the volcanic arc. The width of the zone is 30 km and the angle to the horizontal is about 15° .
5. The slowest mantle P-wave velocities correlating with an increased V_p/V_s -ratio are found directly beneath the volcanoes. These anomalies indicate a zone of partial melting, extending to 100-150 km depth almost vertically (Fig. 5.10). The low velocity is broader in the northern profiles and gets weaker towards the south suggesting a decrease in partial melting from north to south.
6. In Nicaragua, I identified the continental Moho with a sharp increase in the P-wave velocity from 7.6 km/s to 8 km/s at about 30 km depth. This value agrees with the results of a gravity model of western Nicaragua constrained by magnetotelluric measurements, which defined the crust-mantle boundary at ~ 28 km depth (Elming and Rasmussen, 1997). A similar velocity increase is found in N Costa Rica at about 40 km depth, suggesting an increase of crustal thickness from north to south by about 10 km. These mantle depth variations are also indicated in Flueh and von Huene (2007).

5.5 Discussion and Conclusion

5.5.1 Effect of overriding plate on the system

The tomographic maps of P-wave velocity and V_p/V_s ratio down to 60 km depth show a zoning, which corresponds closely to the changes in geological structure observed at the Earth's surface. However the incoming plate does not show a major change within the considered segment. Therefore I conclude that the state of the overriding plate has a major influence on the subduction system of Nicaragua and N Costa Rica. In previous publications (e.g. Grevemeyer et al., 2007; Ranero et al., 2003), mainly changes within the incoming plate have been suggested to be responsible for the geological change along the continental margin. In contrast, our findings show that the properties such as the stress regime, the thickness of the crust and possibly the origin of the overriding plate have to be considered in order to understand the variability of the system as a whole. The major observations to be considered as a result of the overriding plate are the dip change in the slab in the upper 60 km from north to south (Fig. 5.9) and the sharp

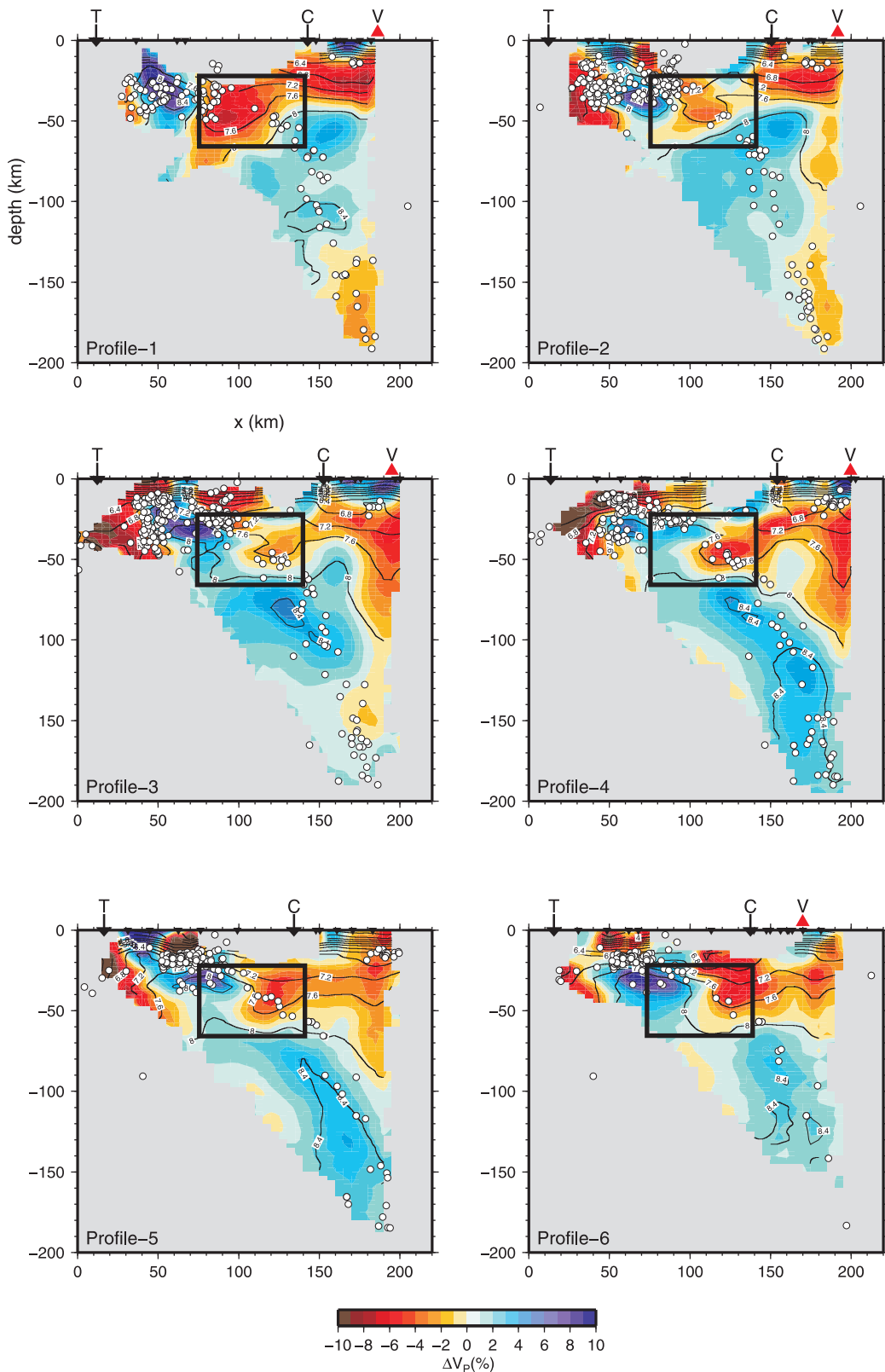


Figure 5.9: Cross-sections through V_p perturbations. Earthquakes (white circles), stations (black triangles), volcanoes (red triangles), trench (T) and coast (C) are projected on to the sections. Contour lines mark absolute P-wave velocities, the contour interval is 0.4 km/s. Profiles are displayed in Fig. 5.8. The box indicates the mantle wedge corner.

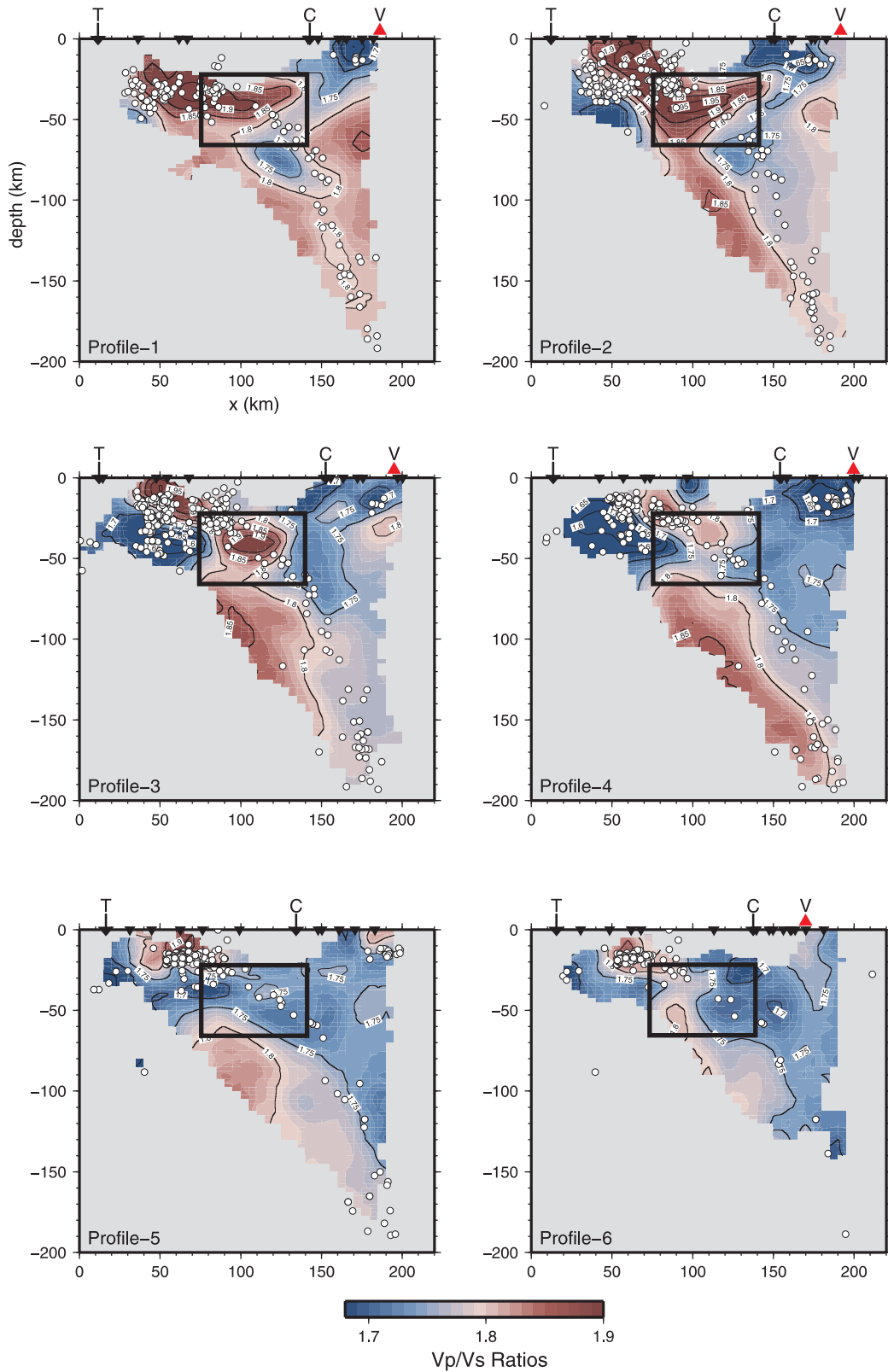


Figure 5.10: Cross-sections through absolute V_p/V_s ratios. Earthquakes (white circles), stations (black triangles), volcanoes (red triangles), trench (T) and coast (C) are projected on to the sections. Contour lines mark absolute V_p/V_s ratios, the contour interval is 0.05. Profiles are displayed in Fig. 5.8. The box indicates the mantle wedge corner.

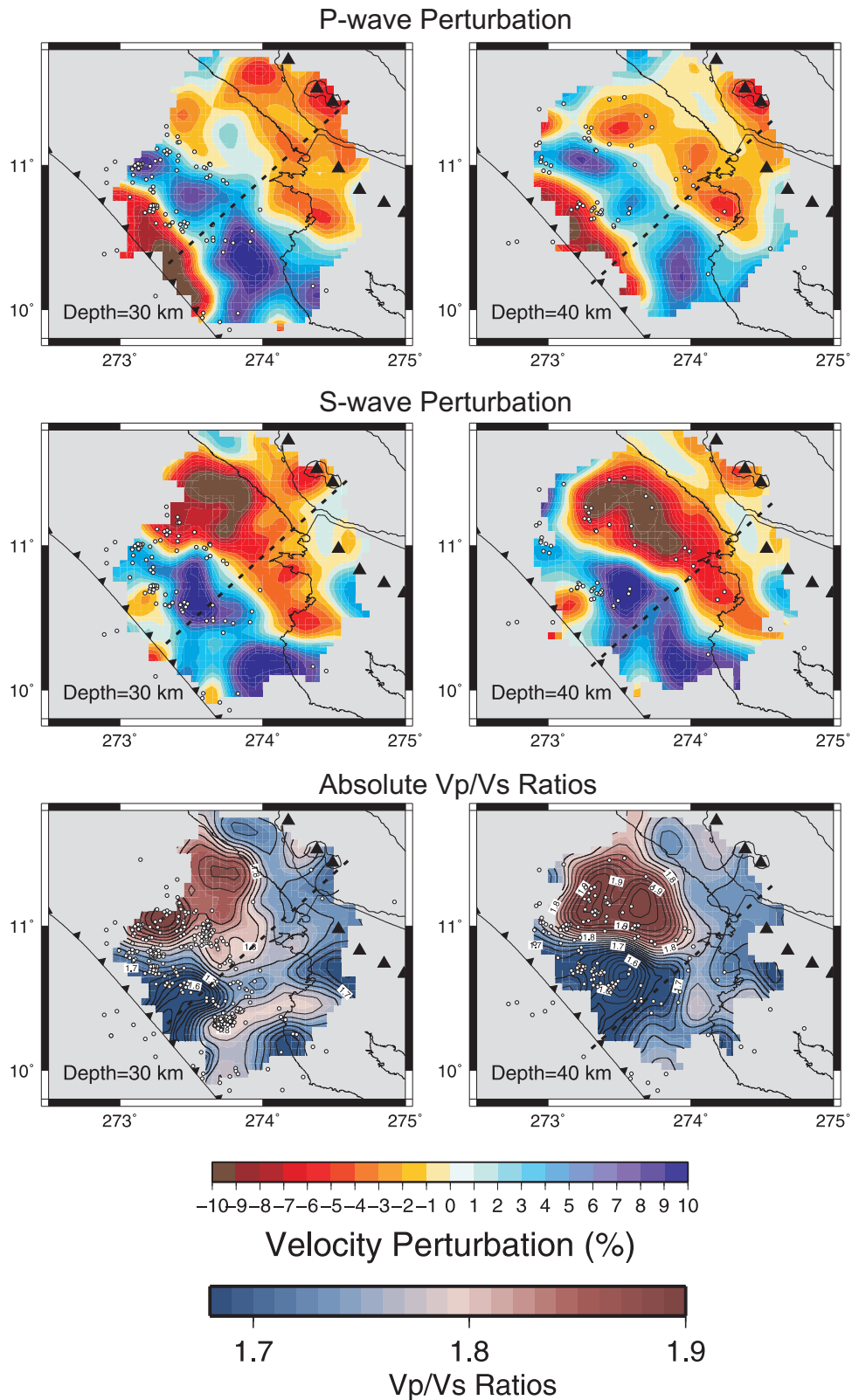


Figure 5.11: Horizontal depth sections for 30 km and 40 km depth. Upper row: V_p perturbations, middle row: V_s perturbations and lower row: V_p/V_s ratio after 5 iterations inversion. The dashed line indicates the possible transition.

lateral contrast in V_p/V_s ratios (Fig. 5.11) in the mantle wedge between northern and southern part.

The overriding plate is composed of the Chortis Block in the north and the Chortega Block in the south. These two terranes are supposed to be separated by a right lateral strike slip fault (Bowland, 1993), thought to represent a continuation of the Hess Escarpment in the Carribean Sea (Fig. 2.1). Our tomographic results (Fig. 5.9) together with Elming and Rasmussen (1997) and Flueh and von Huene (2007) show that the crustal thickness of these two blocks differs by about 10 km. The thinner crust is found beneath Nicaragua and the thicker crust is located beneath N Costa Rica. The crustal thinning may be a result of a tensional stress regime, which finds its expression in back- and fore-arc depression fields such as the Sandino Basin. The origin of this large scale extension is probably the roll-back or step back (Walther et al., 2000) of the slab connected with the oblique subduction and a steep slab (Fig. 7). This situation seems to change in the southern part of our study area, where the crust gets thicker. This is consistent with the recent uplift of Nicoya Peninsula with a rate of 4.5 mm/yr (Marshall and Anderson, 1995).

Heuret et al. (2007) showed in their modelling study that the trench motion, slab geometry and the deformation style of the overriding plate (compression or extension) are closely related to the absolute motion of the overriding plate. Trench advance, steep dip, thin continental crust and backarc extension are observed mostly if the overriding plate is under extensional regime. A number of authors (e.g. Forsyth and Uyeda, 1975; Chapple and Tullis, 1977) invoked the existence of a trench suction force, induced by slab pull. Slab pull would cause the trenchward motion of the arc and its consequent divergence from the overriding plate. This seems to be the case along the Nicaragua segment of the Central American arc. Seno (2005) stated that the stress regime of the mantle wedge also controls the extent of hydration. Hydro-fracturing under extension can be considered as a mechanism to create fluid path ways. Therefore, the high V_p/V_s ratios of ~ 2.0 observed in northern Nicaragua (Fig. 5.10) could be explained by a broadly hydrated mantle wedge which was favoured by an extensional forces in the overriding plate. Also, the forearc and intra arc depression occur along normal faults, that are cutting deeply into the mantle. They may provide additional pathways for fluids to migrate, to hydrate the mantle wedge, crust and to contribute to the melts beneath volcanoes (Fig. 5.12).

5.5.2 Geophysical evidences of mantle wedge hydration

The increased V_p/V_s ratio (~ 2.0) and low P-wave velocity (Fig. 5.9, Fig. 5.10 & Fig. 5.11) observed at the mantle wedge corner (30-40 km depth) in the northern part of the investigation area can be regarded as an evidence for an intense hydration which

is not found in the southern part. This variable degree in mantle wedge hydration correlates with the local maxima of geochemical trace elements found in the N Nicaraguan volcanoes, especially the maxima of ^{10}Be concentration and B/La ratios indicative for oceanic crustal fluids (Carr et al., 2003; Noll et al., 1996; Patino et al., 2000; Hoernle and Hauff, 2007). With increasing degree of hydration or serpentinization V_p/V_s is increased from 1.7 to a maximum of 2.4. On the other hand, the P-wave velocity is reduced from 8.0-8.2 km/s to a minimum of 4.5 km/s at 100 % transformation of peridotite to serpentinite (Christensen, 1966; Carlson and Miller, 2003; Grevemeyer et al., 2007). The P-wave velocities and V_p/V_s ratio found at the tip of the mantle wedge (box in Fig. 5.9 & Fig. 5.10) are between 7.4-7.6 km/s and 1.95-2.00, respectively. These values would be compatible with about 20 % serpentinization and 2.5wt % H_2O . Serpentinite is stable up to temperatures of 600–700° C, at depths between 30-150 km (Ulmer and Trommsdorff, 1995). At higher temperatures it decomposes and water is set free (e.g. Zandt, 2002). In the mantle wedge of S Nicaragua and N Costa Rica the estimated temperature is about $\sim 400^\circ\text{C}$ at 1 Gpa (Rüpke et al., 2002; Peacock et al., 2005). Thus, serpentine should be stable. Similar results have been found for the central Japan subduction zone (Kamiya and Kobayashi, 2000) and the central Cascadia subduction zone (Bostock et al., 2002). Serpentine shows stable-sliding behavior in the laboratory. Therefore, it has been concluded that the plate interface between the slab and hydrated overriding mantle should be seismically silent (Peacock and Hyndman, 1999). Indeed, I observe a decrease in the seismicity in the mantle wedge beneath Nicaragua (Fig. 5.9 & Fig. 5.10) which supports the idea of a locally ductile subduction process connected with weak seismic or aseismic coupling (Kamiya and Kobayashi, 2000; Zhang et al., 2004; van Keken, 2003). At the Central America subduction zone a pronounced aseismic gap between 25-40 km has been observed also by other authors (Protti et al., 1995; Walther et al., 2000). However, it was not paid attention because it was regarded as an artefact of hypocenter localization. With the marine stations, our new data set covers the investigation area more densely than the previous studies, which were only based on the land stations. Moreover, joint tomographic and hypocentral inversion applied by this study provides a reasonable observation for the gap of hypocenters.

5.5.3 Fluid source for the hydrated mantle wedge

Dehydration and eclogitization of the subducting oceanic slab are most likely the source of water for the serpentinization of the forearc upper mantle (Bostock et al., 2002; Brocher et al., 2003; Hyndman and Peacock, 2003). Additionally, fluids are supposed to be introduced into the slab by the sediment filled half grabens, created by the bend-related faults of the incoming plate. The bend-related faults offshore Nicaragua also facilitate plate hydration (Ranero et al., 2003; Grevemeyer et al., 2007). However, how can water

penetrate into the overriding mantle?

Most of the free water is expelled at shallower depths due to the compaction of subducted sediments and collapse of porosity in the upper oceanic crust and most fluid is released beneath the forearc (Rüpke et al., 2002; Hyndman and Peacock, 2003). Additional water is released by dehydration reactions starting at >75 km depth. It may migrate up dip

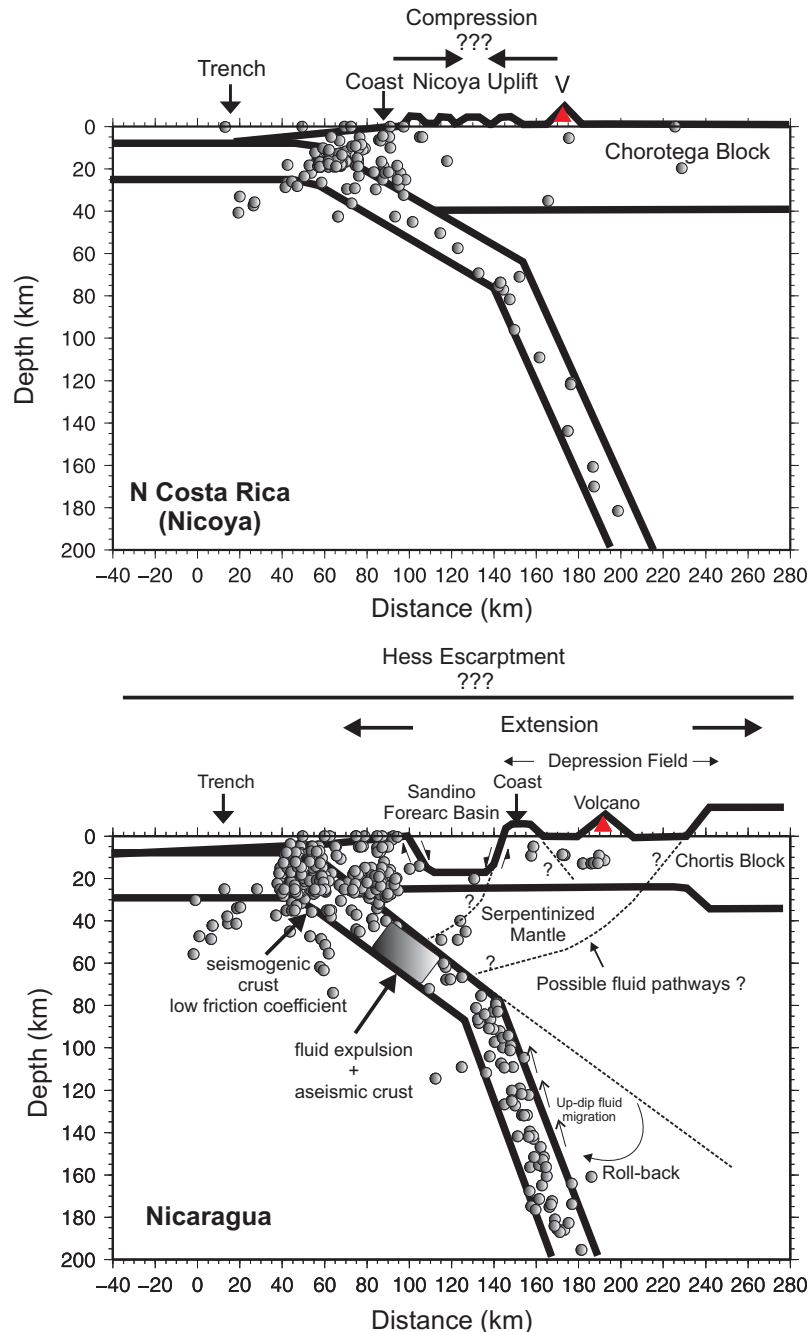


Figure 5.12: Schematic interpretation of the proposed transition between S Nicaragua and N Costa Rica.

in the slab and hydrate subducted crust at shallower levels (Hacker et al., 2003). This process would require a pathway that allows fluids to ascend up the slab. The steep dip of the Nicaragua slab of $\sim 80^\circ$ may facilitate such a pathway. In addition, the P-waves for the intraslab events at 100-150 km depth in Nicaragua show a high-frequency late arrival, apparently trapped in a low velocity waveguide that could be explained by a high degree of hydration (Abers et al., 2003). This hypothesis is supported by our study through the slight increase of V_p/V_s ratios found along the subducting oceanic mantle offshore Nicaragua. For the water ascent into the overriding plate the extensional stress regime and related fractures seem to play an important role. Water accumulated at the depths of 30-50 km in the slab can escape into the overriding mantle wedge along these fractures (Seno, 2005).

Chapter 6

P-wave Anisotropy

6.1 Introduction

Mantle anisotropy is believed to result from strain-induced, preferred orientation of mantle minerals, mainly olivine. Thus anisotropy observations can characterize the orientation and depth extent of the mantle strain fields (e.g. Savage, 1999). Therefore, it is an important tool to understand the mantle dynamics and tectonics of the Earth's interior. The link between mantle anisotropy and mantle tectonics is a consequence of the aggregate alignment of olivine during mantle deformation. Theoretical studies, laboratory and field investigations infer that the anisotropy can be attributed to strain and that there are consistent relationships between the mean orientation of the olivine crystal axes and axes of the strain ellipsoid. The traditional view of the anisotropy concept is the following: during deformation, the olivine slow velocity axes (b axes) tend to align with the shortest strain axis, the olivine fast velocity axes (a axes) tend to align with the longest strain axis, and the olivine intermediate velocity axes (c axes) tend to align with the intermediate strain axis (McKenzie, 1979; Ribe and Yu, 1991; Ribe, 1992) (Fig. 6.1). Consequences of these relationships are that under simple shear deformation, the olivine a axes tend to align in the direction of maximum shearing, while, under pure shear deformation, the olivine b axes tend to align parallel to the direction of maximum compression (Hearn, 1996).

Shear-wave splitting observations from most subduction zones show complex patterns of seismic anisotropy that usually have trench-parallel polarization directions of the fast split S-waves (S1-waves). These observations are unexpected, because models of two-dimensional wedge flow (corner flow) predict fast seismic velocity parallel to plate motion (trench perpendicular) therefore these observations contradict classical corner flows. Recent studies strongly suggest that the anisotropy in subduction zones is generated by 3D flow such as illustrated in Fig. 6.2 (e.g. Long and Silver, 2008). Possible further

causes for the trench-parallel S1-wave polarization and fast anisotropic P-wave velocity and abrupt rotations in the fast directions in the mantle wedge of subduction zones include an olivine fabric transition to B-type (Fig. 6.3), supposed to be present at high stress and water contents (Fig. 6.4) (Kneller et al., 2005), melt-related anisotropy and three-dimensional flow with stretching-parallel olivine fabrics. In this concept, the B-type fabric may be important in explaining trench-parallel fast seismic wave polarization in subduction zones. In addition, three-dimensional flow can be caused by small-scale convection (Honda and Saito, 2003), oblique subduction (Mehl et al., 2003), differential slab rollback (Russo and Silver, 1994), trench-parallel motion of the overriding plate (Hall et al., 2000), and variations in slab geometry (Hall et al., 2000; Mehl et al., 2003).

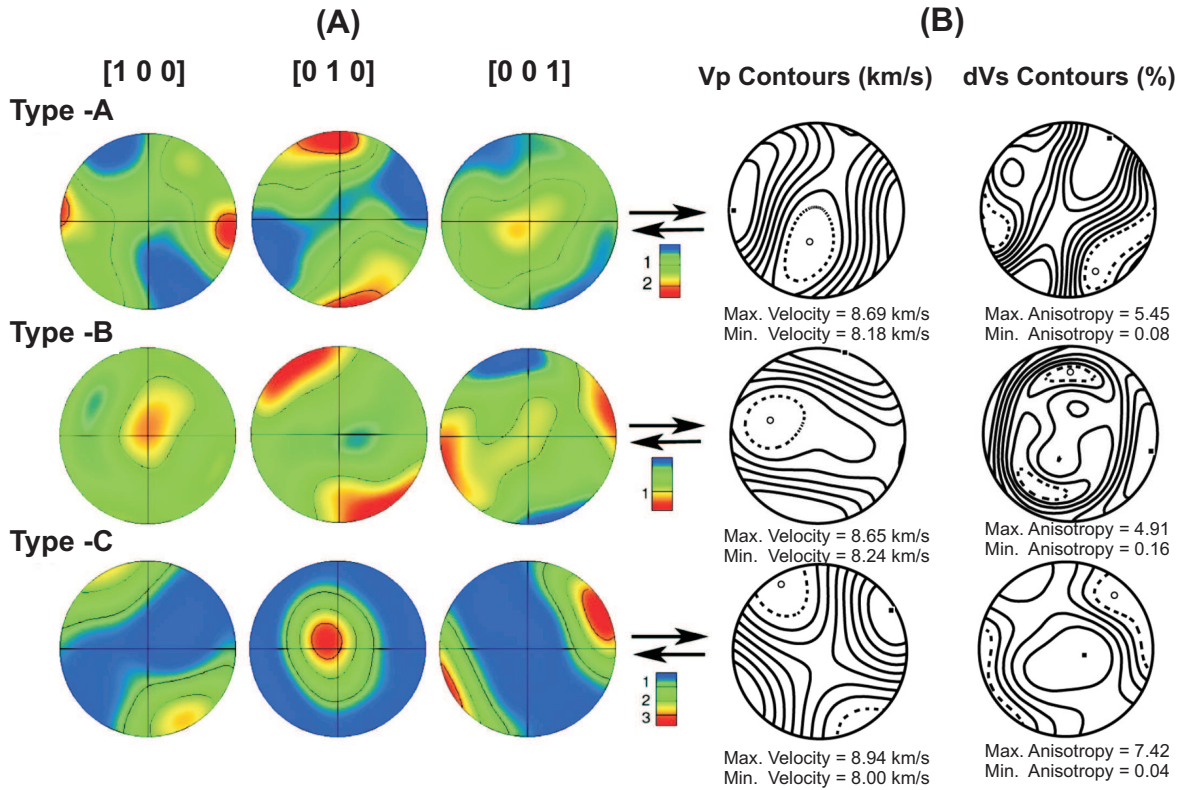


Figure 6.1: Pole figures of crystallographic orientation of deformed olivine aggregates (a) and corresponding seismic anisotropy (b) from Jung and Karato (2001). A) The east-west direction corresponds to the shear direction, and the north-south poles correspond to the shear plane normal. Equal area projection to the lower hemisphere is used. The color coding refers to the density of data points (the numbers in the legend correspond to the multiples of uniform distribution). B) The east-west direction corresponds to shear direction, and the center of the plot corresponds to shear-plane normal (this coordinate is chosen to clearly illustrate the polarization directions of fast shear waves and is different from that used in (A)). Azimuthal anisotropy of P waves (V_p) and magnitude of S-wave polarization anisotropy (dVs) are shown.

Most of the anisotropy studies are based on shear wave splitting. The polarization direction of the leading shear-wave polarization direction (fast direction) varies among

subduction zones. Fast directions, oriented nearly perpendicular to the trench have been reported, for example, in the subduction zones of Tonga (Fischer and Wiens, 1996), Izu-Bonin (Fouch and Fischer, 1996) and Mariana (Fouch and Fischer, 1998). Fast directions sub-parallel to the trench have also been reported for New Zealand (Audoine et al., 2000) and the Shumagin Island section of the Aleutian (Yang et al., 1995). In addition, complex patterns of fast directions have been observed in northeastern Japan (Okada et al., 1995), central Japan (Hiramatsu et al., 1998), central south America (Polet et al., 2000), south central Alaska (Wiemer et al., 1999) and the Lau backarc (Smith et al., 2001).

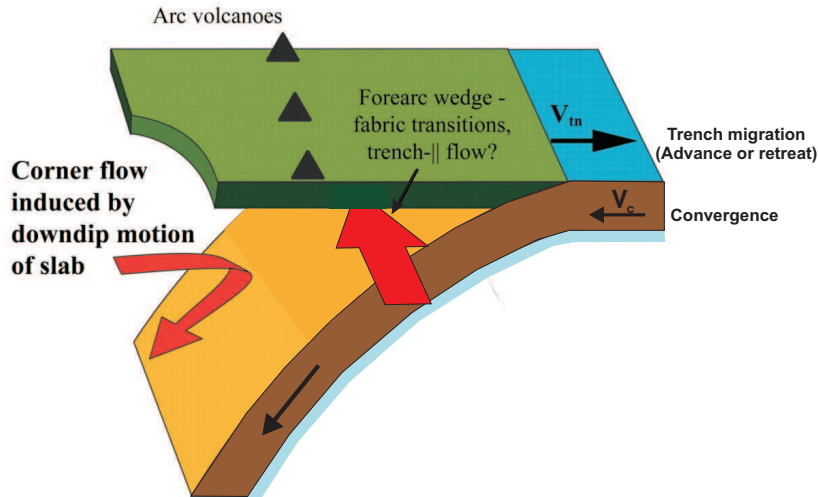


Figure 6.2: Schematic diagram of 2D and 3D flow fields in the mantle wedge revised from Long and Silver (2008).

Previously shear wave splitting analysis in Central America was described by Hoernle et al. (2008). The observed polarization pattern is very complicated and the dominant orientation of the anisotropy is only poorly reconstructed. I believe that P-wave travel time data have the potential to image lateral variations of anisotropic velocity structures with higher resolution than the shear-wave splitting. The observation of shear-wave splitting indicates that there is an anisotropic zone somewhere on a ray path of shear wave, but it is hard to specify what segment of the ray path is anisotropic, especially in the case of spatially variable anisotropy. Often the observed direction of the leading S-wave shows only the tectonic structure of near surface regions (Ozalaybey and Savage, 1995; Savage, 1999). Regarding this situation, we expect P-wave anisotropy analysis to provide us the variation of P-wave anisotropy with depth.

In this study, a P-wave anisotropy analysis is determined for the investigation areas of central Costa Rica and S Nicaragua/N Costa Rica, separately. The same data sets as described in Sections 4.2 and 5.2 are used for this analysis. A comparative discussion is presented in the following sections. The P-wave anisotropy results will be compared

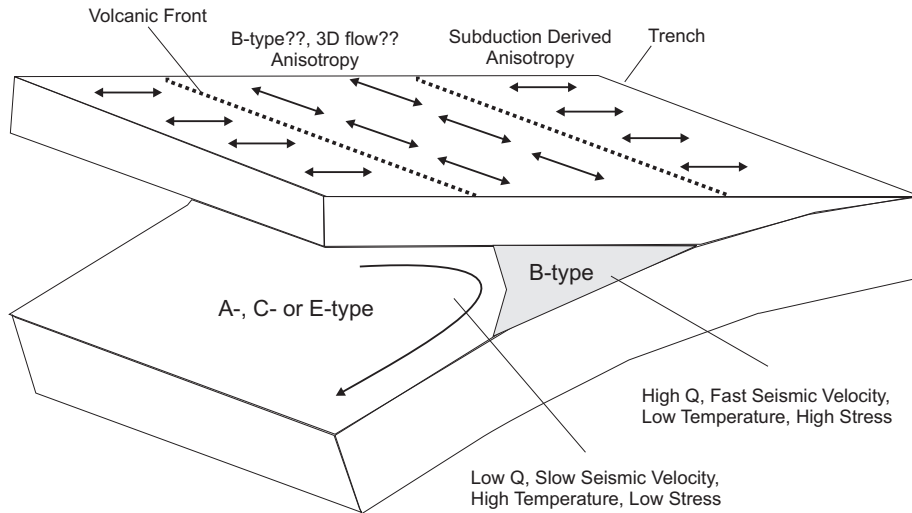


Figure 6.3: Sketch model showing regions for B-type fabric and the transition from B-type conditions to A-type and other fabrics from Kneller et al. (2005). Fast polarization orientations are plotted with black arrows.

with shear-wave splitting anisotropy (Hoernle et al., 2008) beneath Central America. The comparison with results from shear-wave splitting data is especially important in order to verify the consistency of results. Finally, the anisotropy results are related to the regional tectonics of the Central America.

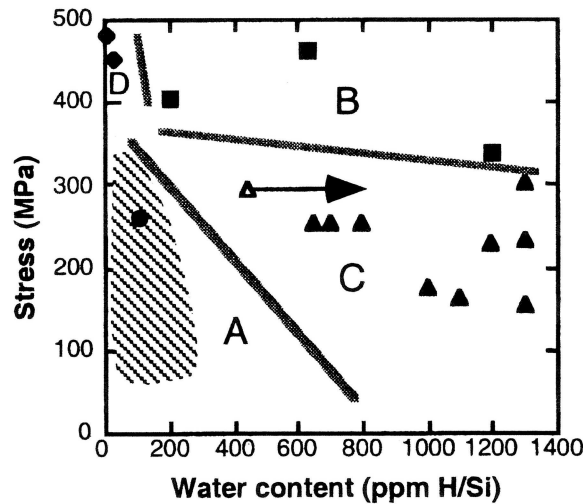


Figure 6.4: A fabric diagram for olivine on a stress-water content plane at higher temperature conditions. Data shown are from the experiments at $T=1400$ to 1570K from Jung and Karato (2001)

6.2 Data Base and Method of Interpretation

The P-wave anisotropy study is based on 2079 events of high signal-to-noise ratio with 31912 P-wave and 9298 S-wave travel time observations from the merged data set of JACO, QUEPOS and the RSN networks in central Costa Rica, and based on 860 earthquakes with 10770 P-phase and 6898 S-phase readings from TOMO network in S Nicaragua/N Costa Rica. The data quality for both investigation areas have been discussed in the previous chapters (Chapters 4&5).

The anisotropic inversion may be an ill-conditioned problem due to the high number of unknown parameters and to the algorithm which presumes an anisotropic medium with a predefined vertical orientation of one of the axes of the anisotropic velocity ellipsoids (Chapter 3). Therefore we applied several resolution tests with synthetic models and real data set with different parametrizations. The aim was to define the best parametrization which provides the most stable results for the existing source-receiver configuration. The best recovered models assist us to evaluate the sensitivity of the model related to the resolution of features in different parts of the study area.

The P-wave anisotropy is described in terms of the following four parameters (cf. 3: formulas 3.6-3.13):

- dV_{max} : maximum horizontal velocity variation;
- dV_{min} : minimum horizontal velocity variation;
- dV_{ver} : velocity variation in vertical direction;
- ψ : azimuth of the maximum velocity orientation;

The travel times for the synthetic models are computed by the anisotropic version of forward 3D ray tracing, using the bending method for the real source-receiver configuration. Then the travel times are distorted by a randomly distributed noise.

Horizontal anomaly test:

I defined three anomalies in a shape of rectangles and assigned to them significantly different isotropic and anisotropic parameters, listed in table 6.1 for central Costa Rica and S Nicaragua/N Costa Rica, respectively. These anomalies correspond to the real situation: An intermediate low velocity anomaly with an arc parallel oriented fast P-axes in the onshore, a low velocity anomaly with a NW-SE oriented fast P-axes in the forearc for central Costa Rica and NE-SW oriented fast P-axes for S Nicaragua/N Costa Rica. And a high velocity anomaly along the trench in the offshore is defined with trench perpendicular oriented fast P-axes. I calculated travel times by forward ray tracing for

the real source-receiver configuration and distorted them by a random distributed noise with 0.15 s RMS.

Table 6.1: Parameters of horizontal synthetic models presented in this study (Fig. 6.5 and 6.6). The parameters for central Costa Rica are presented in the second column and S Nicaragua/N Costa Rica are presented in the third column. dV_{max} and dV_{min} are maximum and minimum horizontal velocity variations; ψ is the azimuth of fast velocity orientation; dV_{ver} is vertical velocity variation.

MODEL	Central Costa Rica				S Nicaragua/N Costa Rica			
	dV_{max}	dV_{min}	dV_{ver}	ψ	dV_{max}	dV_{min}	dV_{ver}	ψ
Trench	15%	5%	10%	45°	10%	3%	7%	45°
Forearc	-5%	-15%	-10%	20°	-5%	-15%	-10%	60°
Onshore	-2%	-6%	-3%	135°	-2%	-6%	-3%	135°

The tomographic results show that the horizontal anisotropic orientation vectors are reconstructed correctly in the central region of the central Costa Rica data set (Fig. 6.5). The shape of the anomalies is also well reconstructed but the amplitudes of the average (isotropic) background velocity are obtained smaller than the input model.

For the S Nicaragua/N Costa Rica region, anisotropic vectors can be reconstructed robustly only along a 30 km wide SW-NE swath in the center of investigation area (Fig. 6.6). This swath however covers all units of the on- and offshore areas. The average (isotropic) background velocities are better reproduced in shape and amplitude than central Costa Rica.

Checkerboard test:

In figures 6.7 and 6.8, we present the results of a checkerboard synthetic tests which also show the horizontal resolution. The initial configuration of the model is presented in the upper left corner. The horizontal block size is 50 km. These anomalies remain unchanged at all depths. The initial anisotropic parameters inside the anomalies are defined the same for both data sets (Central Costa Rica and S Nicaragua/N Costa Rica) and shown in table 6.2.

Table 6.2: Parameters of checkerboard synthetic models presented in this study (Fig. 6.8 and 6.7). dV_{max} and dV_{min} are maximum and minimum horizontal velocity variations; ψ is the azimuth of fast velocity orientation; dV_{ver} is vertical velocity variation.

MODEL	Blue Anomaly				Red Anomaly			
	dV_{max}	dV_{min}	dV_{ver}	ψ	dV_{max}	dV_{min}	dV_{ver}	ψ
CheckerBoard	15%	5%	7%	45°	-15%	-5%	-7%	-45°

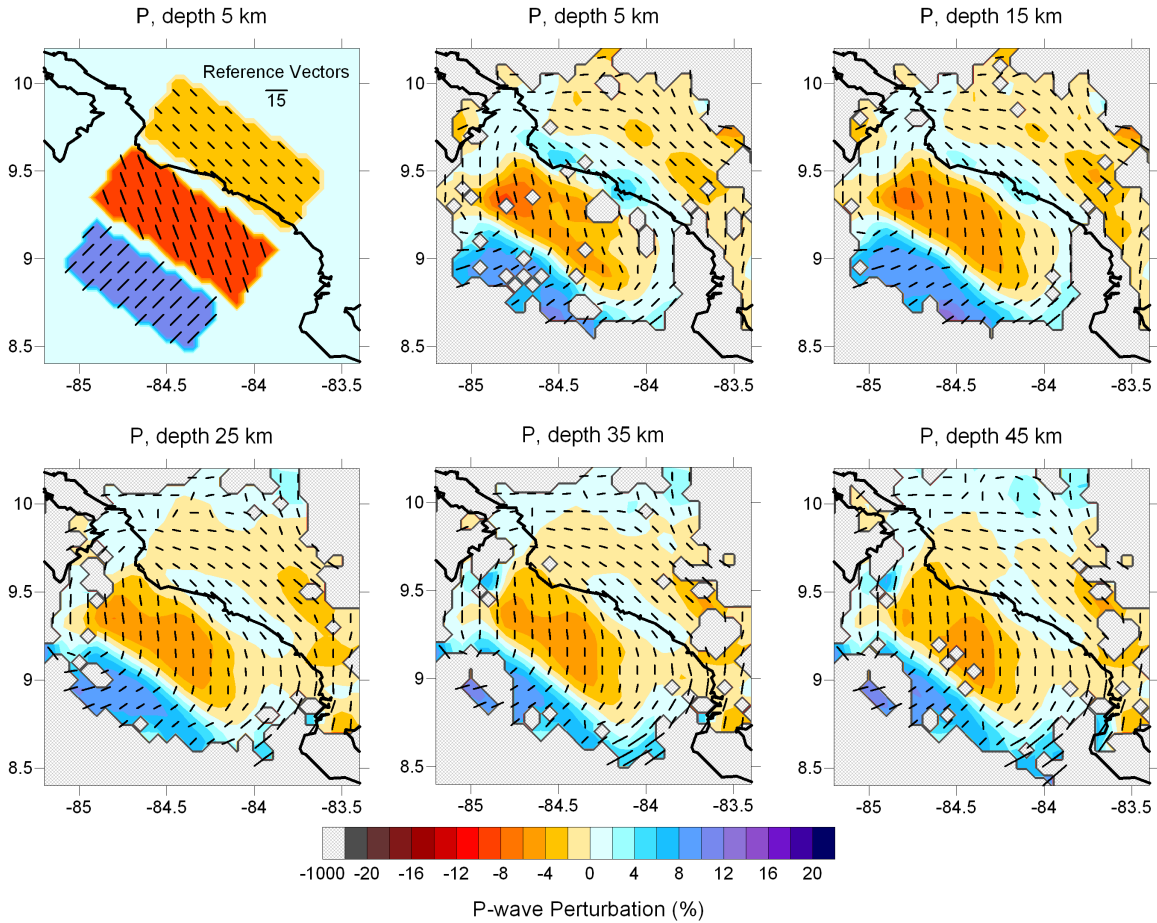


Figure 6.5: Results of the horizontal anomaly test for central Costa Rica data set for different depth sections. The initial model is represented by unlimited vertical columns as shown on the upper left corner. The colors indicate the isotropic velocity perturbations. Vectors show the directions of maximum horizontal velocities. Length of vectors are the difference between the fastest and slowest horizontal velocities. The reference vector (15 %) is shown in the upper left initial model figure. The parameters of the initial model are presented in table 6.1.

After performing a 5 iteration inversion with the synthetic travel times, we obtained the borders of the well resolved areas with the real source-receiver configuration of our data set. The velocity anomalies and fast polarization directions are well reconstructed in the forearc and onshore parts of the study area where we have high ray coverage. The edges of the resolved areas have to be considered as less reliable.

Inversion of the field data with different smoothing and grid parameters:

In the inversion program there are two smoothing constants: one controls the smoothness of the velocity image by damping of the slowness variations and the other constant controls the smoothness of the anisotropy by damping the anisotropy coefficients. Both damping constants control the trade-off between low errors (high damping) and small resolution width (low damping). Therefore it is important to define the proper smoothing

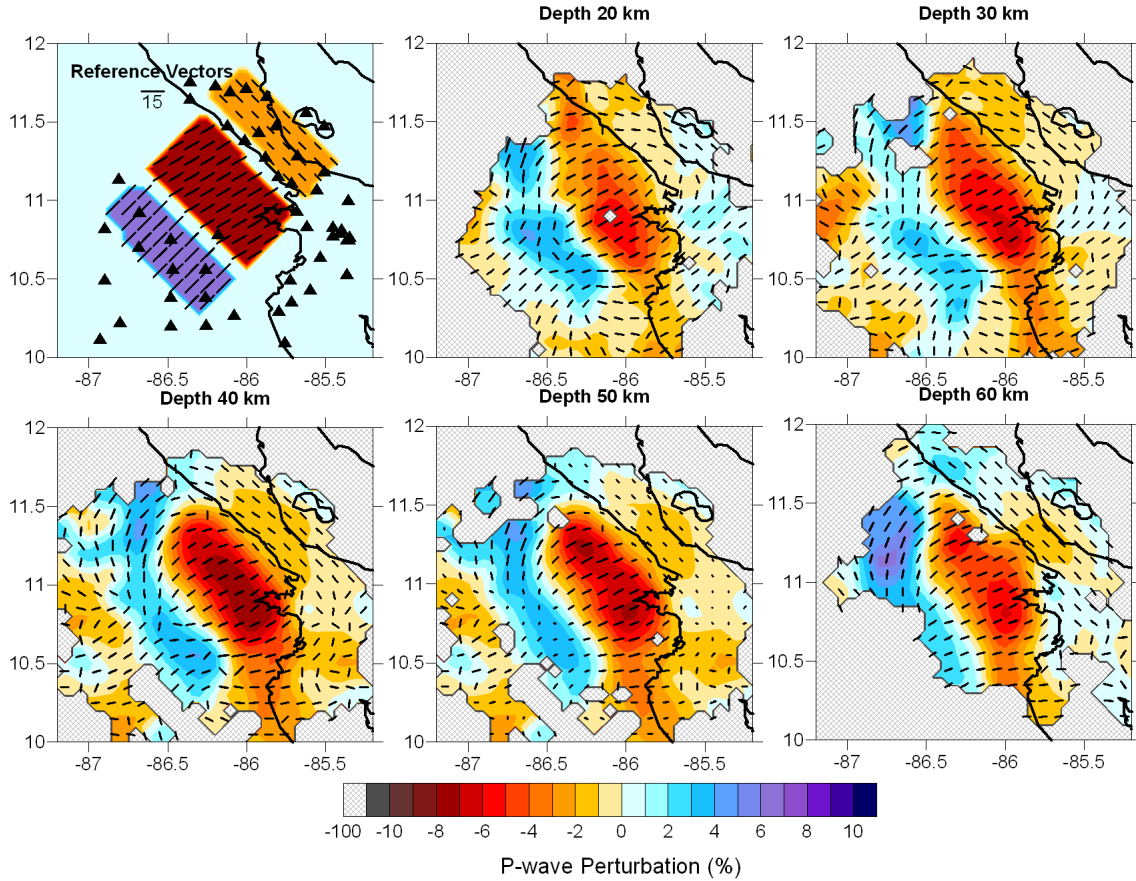


Figure 6.6: Results of the horizontal anomaly test for S Nicaragua/N Costa Rica data set. The initial model is represented by unlimited vertical columns as shown on the upper left corner. The colors indicate the isotropic velocity perturbations. Vectors show the directions of maximum horizontal velocities. Length of vectors are the difference between the fastest and slowest horizontal velocities. The reference vector (15 %) is shown in the upper left initial model figure. The parameters of the initial model are presented in table 6.1.

constants. I estimated the appropriate smoothing parameters for both data sets (central Costa Rica and S Nicaragua/N Costa Rica) by performing real inversions with different smoothing parameters (Figs. 6.9 and 6.10).

The grid parametrization should be constructed in such a way that it may appropriately represent the 3D velocity structure of the real earth. Smaller grid spacing can cause artefacts due to the insufficient ray coverage. But also with larger grid spacing the existing real anomalies could be avoided. It means that a seismic grid must be fine enough to allow adequate representation of near surface structures. Therefore several grid spacings were tested.

Figure 6.9 shows the results of central Costa Rica for different grid and smoothing parameters. The first row is the results for 5 km grid spacing with a smoothing factor of 5. The calculated RMS for this case is 0.13 which is the lowest. But the anisotropy vec-

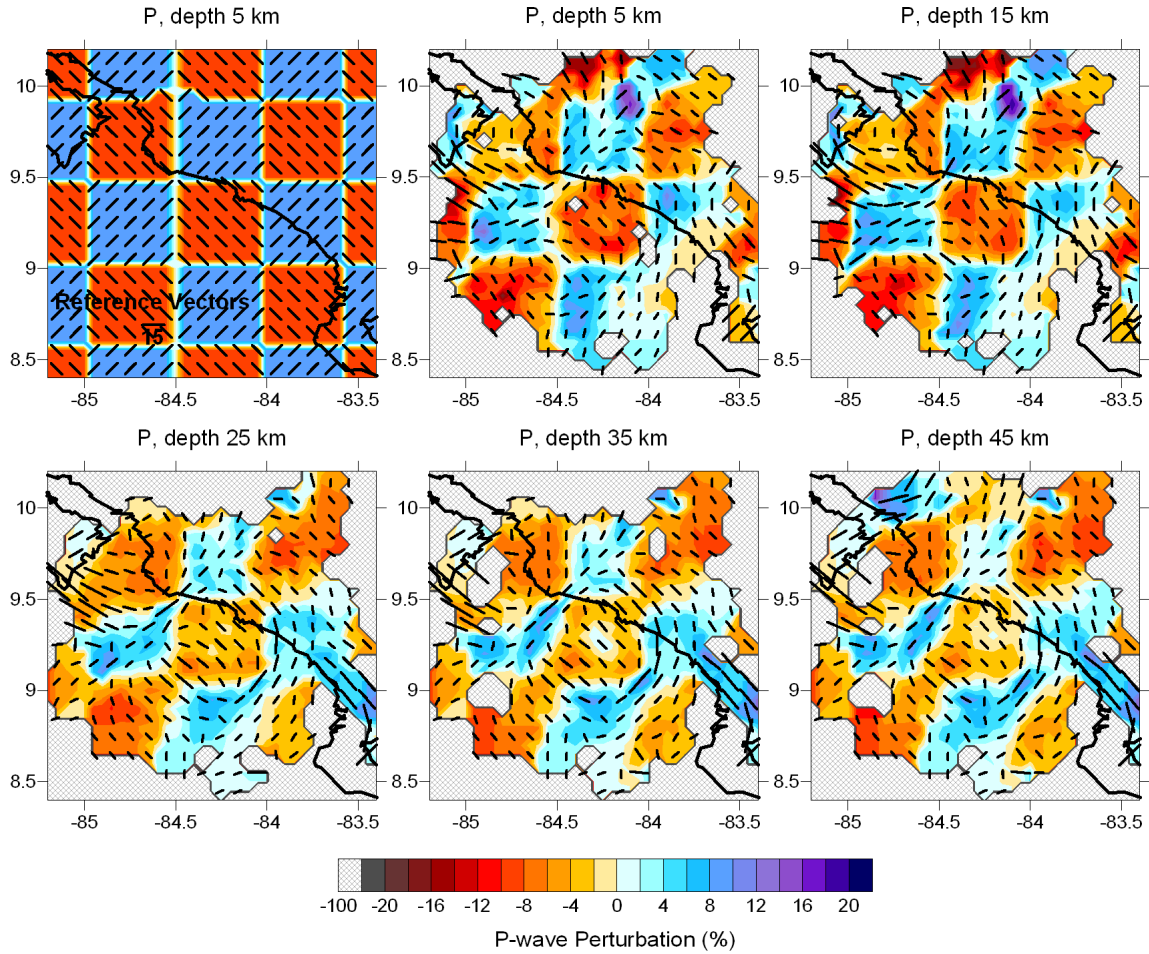


Figure 6.7: Results of the checkerboard test for central Costa Rica. The initial model is represented by unlimited vertical columns as shown on the upper left corner. The colors indicate the isotropic velocity perturbations. Vectors show the directions of maximum horizontal velocities. Length of vectors are the difference between the fastest and slowest horizontal velocities. The reference vector (15 %) is shown in the upper left initial model figure. The parameters of the initial model are presented in table 6.2.

tors are mostly scattered around showing unstabilities. Higher smoothing constant (10) with the same grid size (5 km) improved the distribution of the vectors but increased the RMS value to 0.14 s (Fig. 6.9b). Fig. 6.9c presents the results of a greater grid spacing of 10 km with a smoothing factor of 10. Although the RMS is increased to 0.15 s, the magnitudes and directions of the anisotropy vectors and the isotropic velocity at the background remained almost the same with the Fig. 6.9b. In all three cases, the isotropic part is calculated robustly showing similar anomalies and the RMS variations are in the order of the sampling interval of the seismograms. Therefore it is meaningful to select the third case which will decrease the computation time due to the smaller size of matrix and produce more stable solutions for the anisotropy vectors.

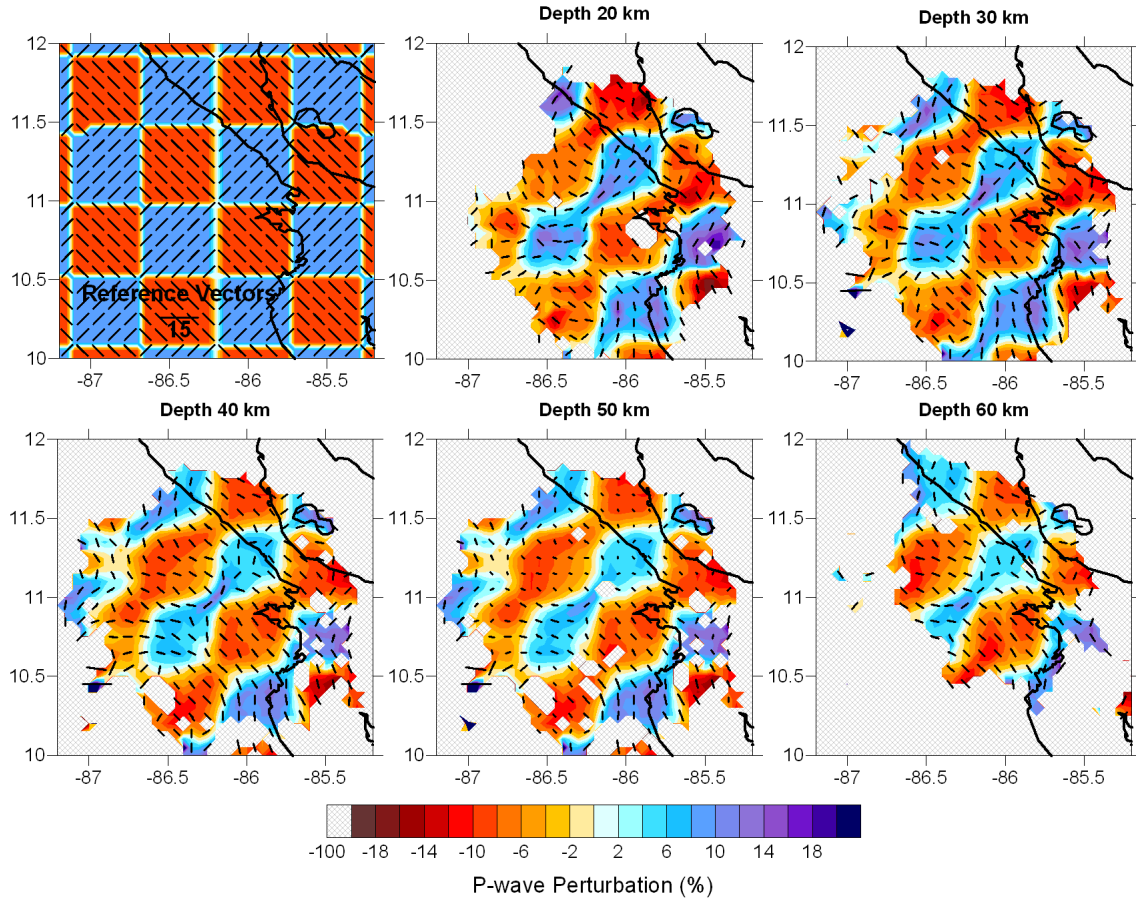


Figure 6.8: Results of the checkerboard test for S Nicaragua/N Costa Rica. The initial model is represented by unlimited vertical columns as shown on the lower right corner. The colors indicate the isotropic velocity perturbations. Vectors show the directions of maximum horizontal velocities. Length of vectors are the difference between the fastest and slowest horizontal velocities. The reference vector (15 %) is shown in the upper left initial model figure. The parameters of the initial model are presented in table 6.2.

Figure 6.10 presents the results of S Nicaragua/N Costa Rica data set for different grid and smoothing parameters. The first row shows the results of 10 km grid spacing with smoothing factor of 10, the second row displays the results of 10 km grid spacing with a smoothing factor of 5 and the third row shows the results of 5 km grid spacing with smoothing factor of 10. After 5 iterations inversion the isotropic part is robustly reconstructed. There are negligibly small anomalies calculated by the 5 km grid spacing (Fig. 6.10c) but the main anomalies remained the same. For example the main anomalies of high velocity subducting plate, forearc and the volcanic chain are still distinguishable. Regarding to those three inversions with different parametrization, grid spacing of 10 with a smoothing factor of 10 are selected for the real data inversion which provided the best model in the mean of amplitude, shape and P-wave fast directions although the RMS values were slightly higher.

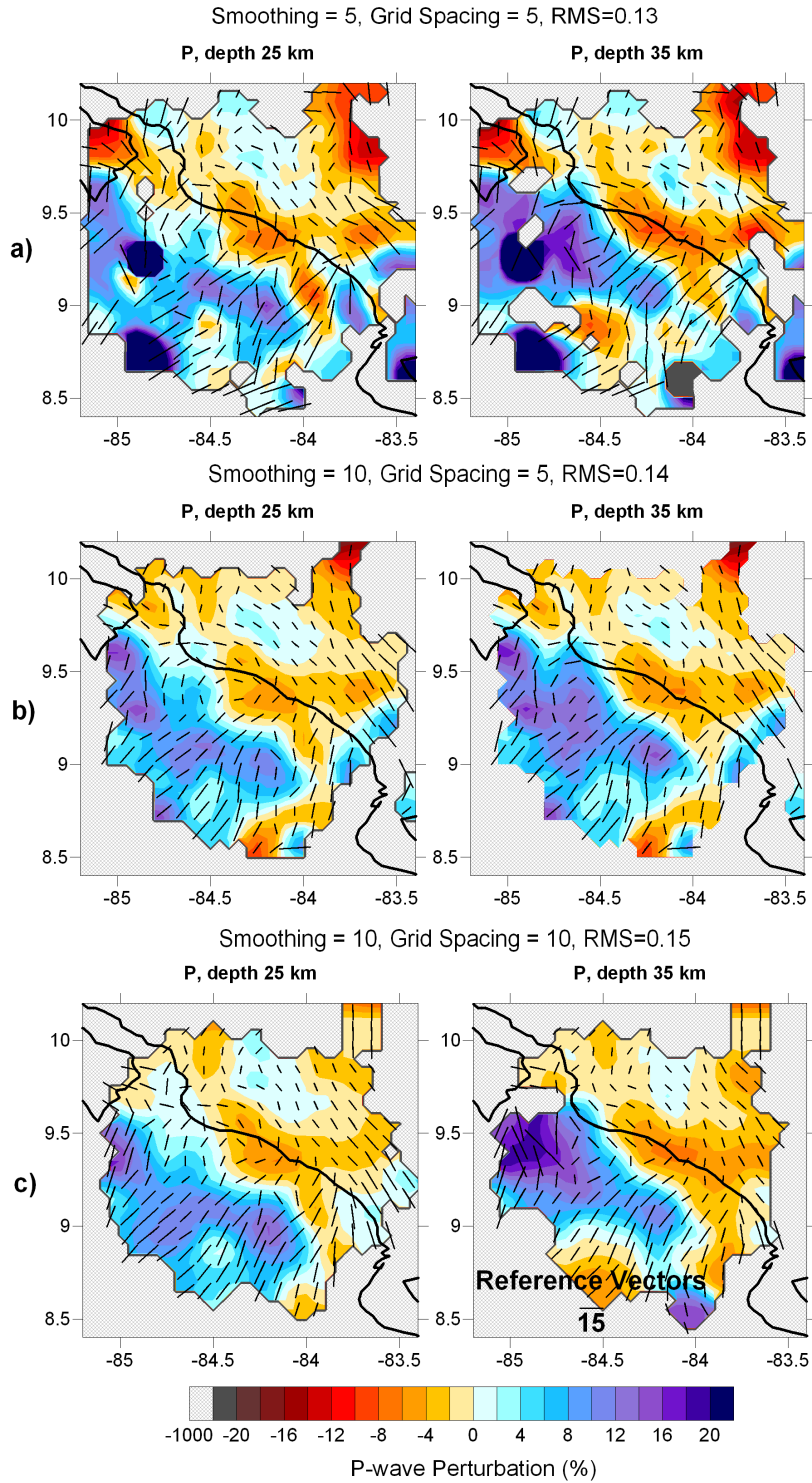


Figure 6.9: Results of the inversion of field data for different grid and smoothing parameters for the central Costa Rica data set. The colors indicate the isotropic velocity perturbations. Vectors show the directions of maximum horizontal velocities. Length of vectors are the difference between the fastest and slowest horizontal velocities. The reference vector (15 %) is shown in the right bottom corner.

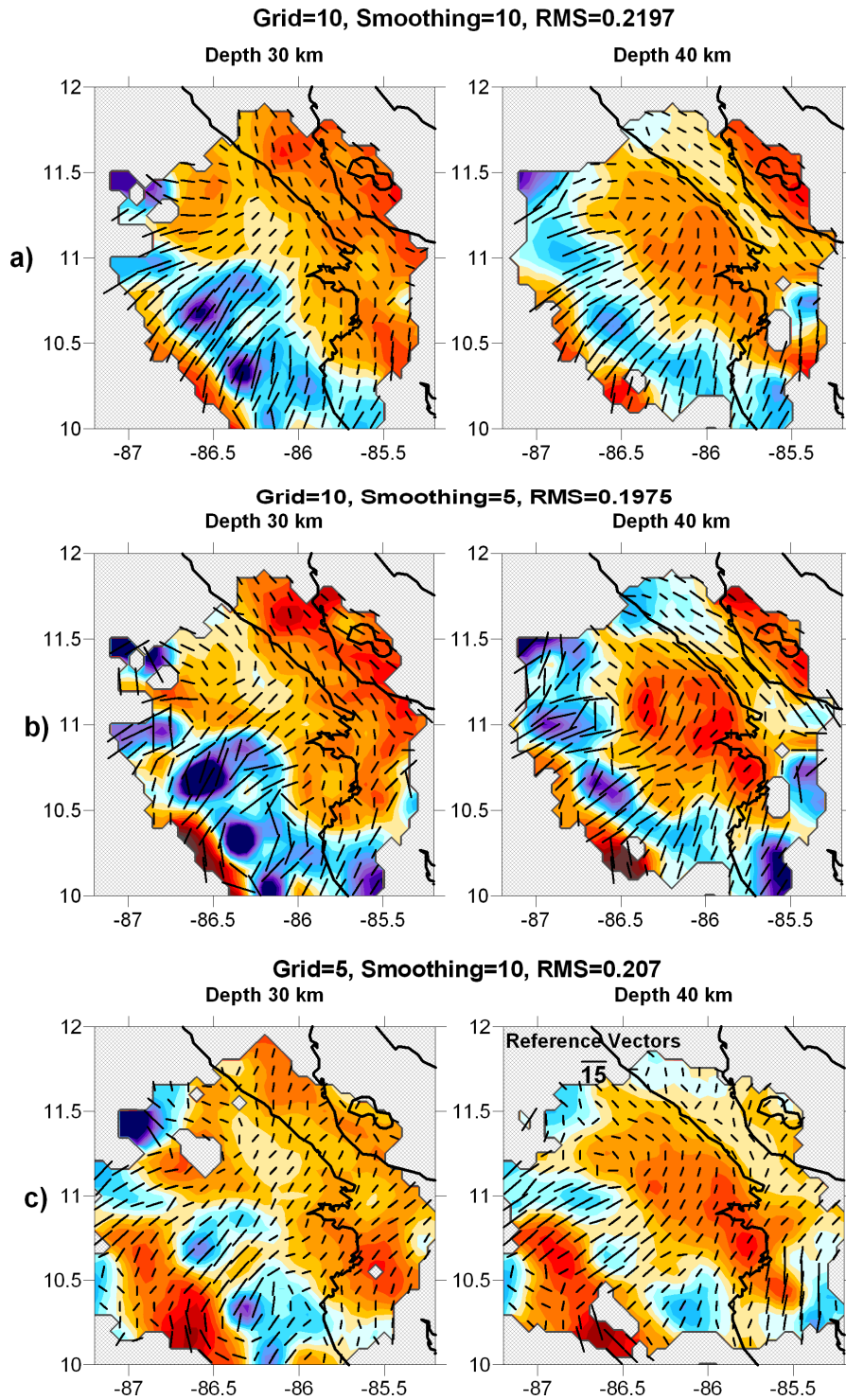


Figure 6.10: Results of the inversion of field data for different grid and smoothing parameters for the S Nicaragua/N Costa Rica data set. The colors indicate the isotropic velocity perturbations. Vectors show the directions of maximum horizontal velocities. Length of vectors are the difference between the fastest and slowest horizontal velocities. The reference vector (15 %) is shown in the right bottom corner.

6.3 Results

Using the parametrization determined in the previous section, I performed 5 iterations of P-wave anisotropic inversion for both data sets. In order to assess the significance of the anisotropy I compared the final P-wave residuals of anisotropic and isotropic inversions (Table 6.3 & 6.4).

It can be seen that the reduction of RMS for the anisotropic inversion is quicker than the isotropic case for S Nicaragua/N Costa Rica data set (Table 6.4). After five iterations the anisotropic model provides smaller RMS than in the isotropic model. This difference shows that the contribution of anisotropy is fairly important in the case of S Nicaragua/N Costa Rica. But for the central Costa Rica data set I did not observe a similar reduction in RMS (Table 6.3). This shows that there seems to be a trade-off between the structural heterogeneity and anisotropy.

Table 6.3: RMS values of P-wave travel time residuals and RMS reductions during 5 iteration steps for anisotropic and isotropic inversions for central Costa Rica.

Iteration	Anisotropic P-velocity model		Isotropic P-velocity model	
	RMS of dtp	RMS Red., P, %	RMS of dtp	RMS Red., P, %
1	0.309	0	0.308	0
2	0.174	43.40	0.169	44.99
3	0.148	51.89	0.140	54.44
4	0.139	54.79	0.132	57.36
5	0.134	56.32	0.127	58.79

The fast propagation directions of P-wave anisotropy show 2 main structures:

1) Trench perpendicular orientations along the high velocity anomaly in the offshore part: The orientation vectors are aligned almost homogeneously perpendicular to the trench. Between 85°W and 84°W in Costa Rica and 86°W and 87°W in Nicaragua, the trench perpendicular orientations are NE-SW, but the directions are rotated to N-S in Osa Peninsula in the south and in Nicoya Peninsula in the north. However, this N-S orientation could be caused by the artefacts on the edge of the observation area.

2) Trench parallel orientations along the forearc and arc: Between the coast and the volcanic chain, the fast directions rotate and tend to orient arc-parallel in the onshore along the volcanic chain. In central Costa Rica arc-parallel orientations show some heterogeneities at mantle depths but somehow, in S Nicaragua/N Costa Rica, the orientations are dominantly arc parallel with a magnitude of 10 %. These arc-parallel orientations are independent of the different smoothing and grid parameters.

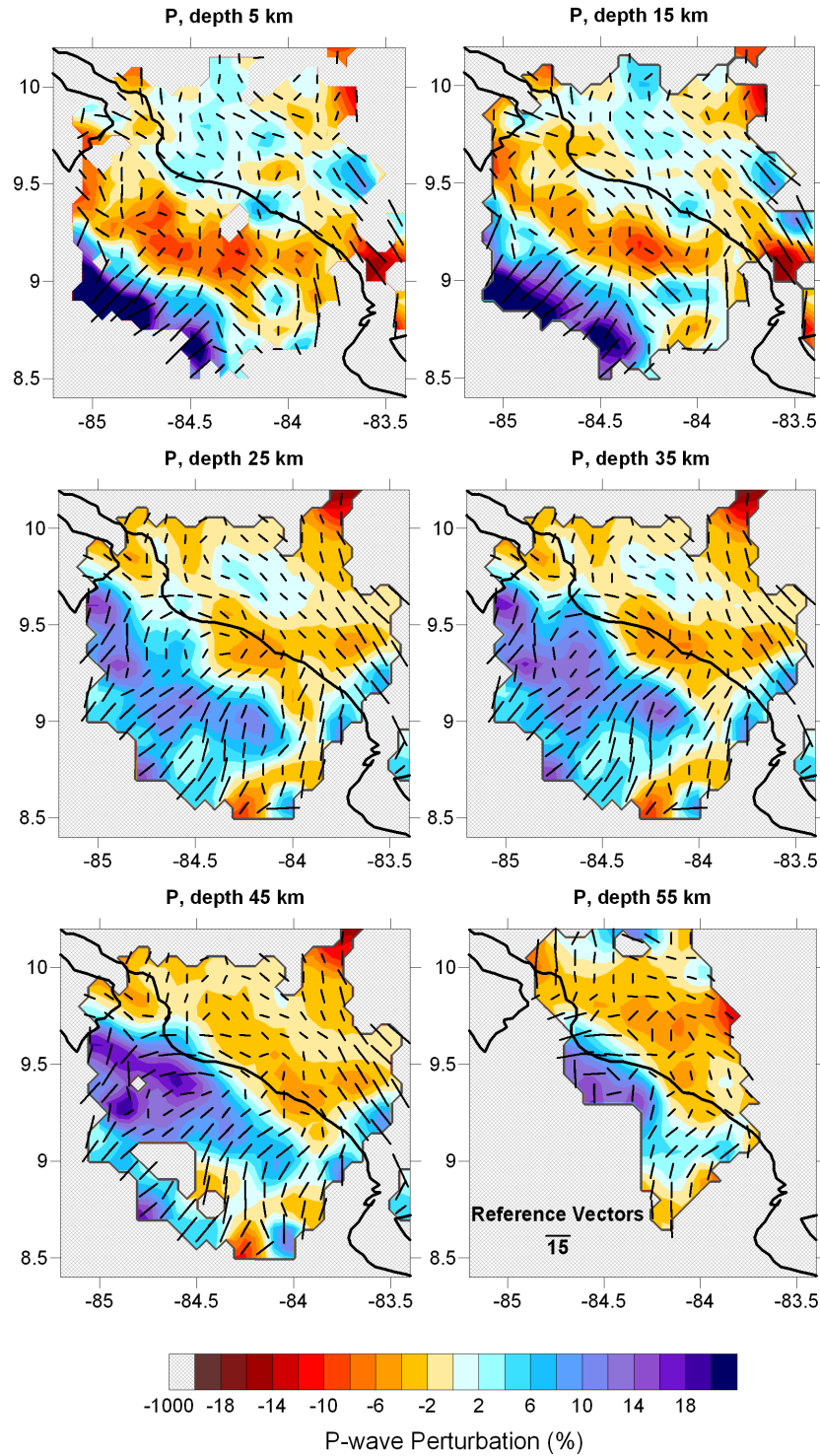


Figure 6.11: Results of anisotropic inversion after five iterations in horizontal sections for central Costa Rica. Colors indicate the isotropic velocity perturbations, which are computed from an average of four anisotropic parameters for each point. Vectors show the directions of maximum horizontal velocities. Length of vectors reflects the difference between the fastest and slowest horizontal velocities. The reference vector (15 % of anisotropy) is shown in the right-bottom corner.

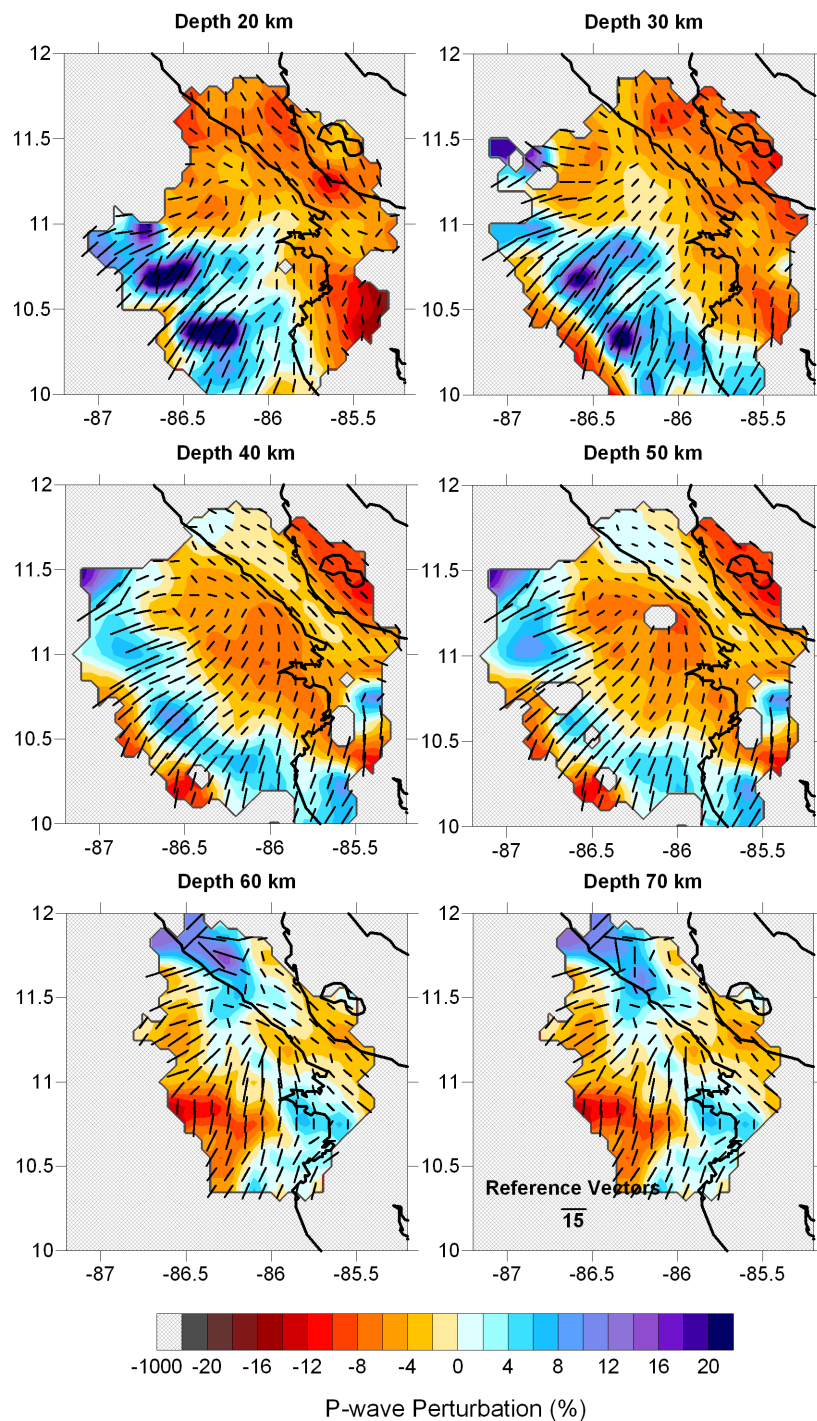


Figure 6.12: Results of anisotropic inversion after five iterations in horizontal sections for S Nicaragua/N Costa Rica. Colors indicate the isotropic velocity perturbations, which are computed from an average of four anisotropic parameters for each point. Vectors show the directions of maximum horizontal velocities. Length of vectors reflects the difference between the fastest and slowest horizontal velocities. The reference vector (15 % of anisotropy) is shown in the right-bottom corner.

Table 6.4: RMS values of P-wave travel time residuals and RMS reductions during 5 iteration steps for anisotropic and isotropic inversions for S Nicaragua/N Costa Rica.

Iteration	Anisotropic P-velocity model		Isotropic P-velocity model	
	RMS of dtp	RMS Red., P, %	RMS of dtp	RMS Red., P, %
1	0.364	0	0.366	0
2	0.248	31.64	0.290	20.64
3	0.218	39.88	0.253	30.72
4	0.204	43.76	0.238	34.89
5	0.197	45.71	0.226	38.03

6.4 Discussion and Conclusion

Offshore, the fast direction of P-wave anisotropy is NE-SW oriented, which is parallel to the direction of relative plate motion (trench normal) between Cocos Plate and Caribbean plate. In contrast, along the arc, the fast orientations are abruptly changed to almost trench-parallel directions (NW-SE).

The trench perpendicular orientations which may be induced by the downdip motion of the slab, could be explained by classical 2D flow. But in the forearc and along the arc, the fast polarization directions abruptly orient arc parallel and the 2D corner flow model seems to fail. The anisotropy in such complicated region has to be explained either by a 3D flow model or by the occurrence of B-type fabric.

The anisotropy resulting in arc-parallel fast directions can be explained by several hypotheses. Russo and Silver (1994) explained the trench-parallel fast directions in South America by trench parallel flow beneath the slab associated with slab rollback. Smith et al. (2001) suggested that the trench parallel fast directions in the Lau Basin result from trench parallel flow around a slab edge. Hall et al. (2000) proposed that oblique subduction, slab rollback or existence of significant strike slip motion in the back arc, result in significant trench-parallel shear in the mantle wedge and simple corner flow fails. In this case three-dimensional flow patterns in the mantle wedge become important (Fig. 6.2). An alternative model is corner flow with B-type olivine fabric in the mantle wedge which occurs in the case of high water content and high stress shown in Fig. 6.4 (Jung and Karato, 2001). Jung and Karato (2001) revealed that the dominant slip systems in olivine change by adding water, and that the fast direction produced by the deformation of water-rich olivine under high-stress conditions is nearly perpendicular to the flow direction (Fig. 6.3). The existence of B-type olivine in the mantle wedge, results in simple 2D corner flow (trench perpendicular) in the mantle wedge producing trench-parallel fast splitting directions (Jung and Karato, 2001). That means, in the

case of B-type olivine transition, the fast direction will not be aligned with the mantle flow direction.

The trench parallel alignment of the fast axis orientations ($\sim 10\%$) is consistent with the shear wave splitting results shown in Hoernle et al. (2008). The S-waves suggest arc-parallel a-axes beneath much of the arc in Nicaragua and Costa Rica. Hoernle et al. (2008) interpreted this pattern as an indication of an arc parallel flow in Costa Rica and Nicaragua which has its origin in the mantle wedge above the subducting slab (Fig. 6.11 & 6.12). Hoernle et al. (2008) see a correlation of the shear wave splitting results and a lead isotope signatures from volcanic front lavas of Central America. They found out that geochemical signatures from Costa Rica are also evident in Nicaragua with a decreased magnitude of concentration. Interpreting this finding as a material transport to northwest, they estimated the flow rates of 63-190 mm/yr which is comparable to the magnitude of the Cocos Plate motion (~ 80 mm/yr) (Demets et al., 1994). Also GPS measurements (Turner et al., 2007) show 15 mm/yr forearc motion towards the northwest and DeMets (2001) estimated the arc-parallel forearc sliver motion in Nicaragua with a rate of 14 mm/yr. The combination of all these investigations provide a strong evidence of arc-parallel flow in Costa Rica and Nicaragua (Fig. 6.13).

Probable causes of the arc-parallel mantle flow could be: a change in the subducting plate geometry, proximity to the slab edge and most probably the strong slab rollback in Nicaragua which may generate arc-parallel fast axis orientations. However, an olivine fabric transition to B-type, which is supposed to be present at high water contents (Nakajima and Hasegawa, 2004) can not be ruled out in the case of Costa Rica and Nicaragua. I proposed that the mantle wedge corner is highly hydrated beneath southern Nicaragua (Fig. 5.11) and central Costa Rica (Fig. 4.16) in the previous chapter. This high V_p/V_s ratios are not observed beneath northern Costa Rica (Nicoya Peninsula) and the southern edge of Costa Rica (Osa Peninsula) (Figs. 5.11 and 4.16). The abnormal hydration ($V_p/V_s > 1.9$) beneath Nicaragua is also emphasized in several publications (Hoernle et al., 2008; Carr et al., 2003; Kutterolf et al., 2007; Abers et al., 2003). A possible hydration and serpentinization for central Costa Rica (Quepos) is also mentioned by Husen et al. (2003); Hacker et al. (2003). Following these publications and this study, we have to consider that high water content in the Nicaraguan and central Costa Rican mantle wedge could alternatively be an indication for a B-type olivine fabric transition as well. The models from Kneller et al. (2005) suggest low temperatures, high stress and B-type fabric in the part of the subduction zone where the trench-parallel fast directions are observed. The estimated temperature is about 400° C at 1 Gpa in the mantle wedge of Nicaragua and N Costa Rica (Peacock et al., 2005). The Cocos plate motion to north relative to the Caribbean Plate (Demets et al., 1994) and forearc motion toward to the northwest (Turner et al., 2007) are strong evidences for the high stress in the

region. These informations can indicate that temperature and stress in forearc mantle and slab-wedge interface are suitable for B-type fabric. The anisotropy caused by the B-type fabric transition is also mentioned in Kamchatka, Alaska (Kneller et al., 2005) and Ryukyu (Long and van der Hilst, 2006) subduction systems.

In conclusion, the situation in the study area can not uniquely be determined. It can be explained either by a combination of arc-parallel mantle flow and olivine A-type fabric related to the dry mantle rocks or by a simple 2D corner flow involving olivine B-type fabric related to a strongly hydrated mantle.

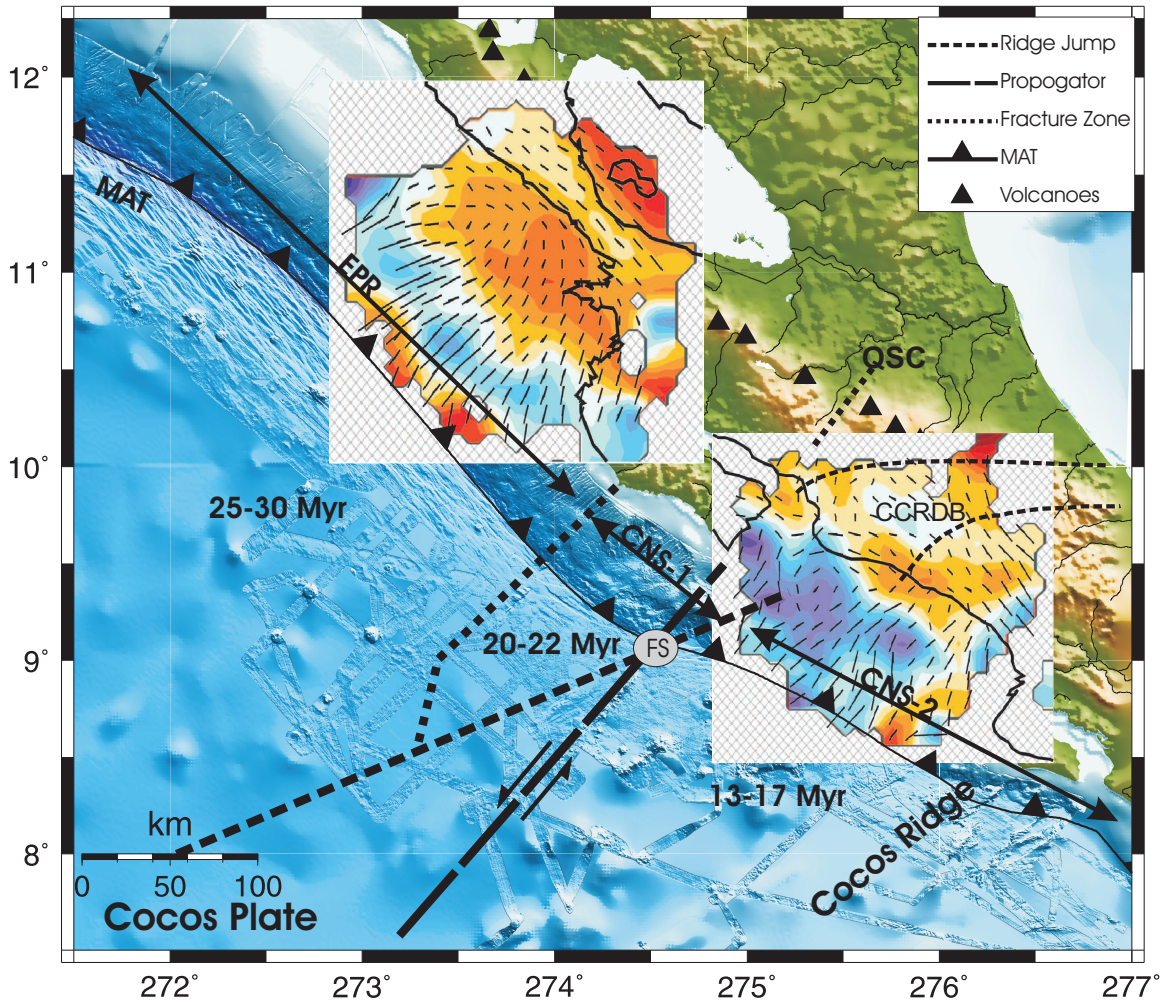


Figure 6.13: Results of anisotropic inversion in horizontal sections for the 40 km (mantle) depth from S Nicaragua/N Costa Rica and central Costa Rica, indicating an arc parallel flow.

Chapter 7

Conclusions

Based on the analysis of P-wave velocity, V_p/V_s ratio, local earthquake hypocenters and P-wave anisotropy the following conclusions can be drawn for the central Costa Rica and S Nicaragua/N Costa Rica margins regarding the stress distribution, dehydration and hydration processes.

1. The seismogenic zone and slab geometry of central Costa Rica exhibit significant spatial variation corresponding to the spatial change of the incoming plate. The general trend shows a steepening of the plate interface towards the south (Osa Peninsula) and an increasing complexity of the plate contact.
2. There is an evidence of mantle wedge hydration beneath NW central Costa Rica. The fluid input into the mantle wedge is higher in the fractured seamount province than in Cocos Ridge area.
3. A transition zone is defined as the result of the changing structure of the incoming plate with the fractured dewatering seamount province in the NW and the Cocos Ridge in the SE central Costa Rica.
4. We find evidence for 2.5 wt.% mantle wedge hydration beneath S Nicaragua. In contrast, the mantle wedge beneath N Costa Rica is only weakly or not hydrated. The hydration leads to a local gap in the seismicity.
5. The lateral transition between the hydrated and non hydrated areas occurs within a distance of about 10 km. This transition coincides with significant structural changes in the overriding plate: in particular a change in the crustal thickness in order of 10 km, thickening to the south and existence of different tectonic regimes.
6. The change in the tectonic regimes towards a stronger extension along the margin of Nicaragua seems to be the key for understanding the observed seismic structure:

the extension supports the opening of pathways for wide zones of fluid migration and hydration through the overriding plate which are identified with areas of low V_p , high V_p/V_s and low seismicity.

7. The extension has to be seen in the context of a large scale slab roll-back starting in Nicaragua with increasing amplitude to the north. It finds its expression in a significant steepening of the subducted plate towards the north of the observation area.
8. The results of P-wave anisotropy studies are compatible with the idea of an arc-parallel flow in Central America. However, the anisotropy can also be explained by the presence of B-type fabric in the mantle and simple corner flow.
9. Mainly, the transition from dominating compressional forces in the south to extensional forces in the north explains the change along the subduction zone.

Acknowledgement

First of all, I would like to thank my advisor Prof. Dr. Wolfgang Rabbel for his important suggestions, advice and criticism. His excitement in my results made me highly motivated in my work. Ernst Flueh is warmly acknowledged for his contribution to my work. Valuable and rigorous discussions of him resulted in a nice output. I really thank Martin Thorwart for sharing his knowledge about programming and also his efforts during the field work. Yvonne Dzierma is thanked for her supports during the field work and nice suggestions during my study. Her patience in sharing an office with me during the stressfull days of writing a thesis was incredible. Ivan Koulakov is acknowledged for providing me the LOTOS and ANITA codes. He also provided valuable technical support. Zuzana Alasonati, Diana Wagner and all the other colleagues are thanked for their help, support and especially for their friendship. I am grateful to Feyzullah Sanioglu for being beside me, encouraging and motivating me during my studies. He was also so thoughtful regarding my stress. Finally many thanks to my parents for believing in me and encouraging me all of my life. This study is dedicated to you.

Bibliography

- Abers, G. A., Plank, T., and Hacker, B. R., 2003. The wet Nicaraguan slab. *Geophys. Res. Lett.*, 30:70–1.
- Audoine, E., Savage, M. K., and Gledhill, K., 2000. Seismic anisotropy from local earthquakes in the transition region from a subduction to a strike-slip plate boundary, New Zealand. *J. Geophys. Res.*, 105:8013–8034.
- Barckhausen, U., Ranero, C. R., von Huene, R., Cande, S. C., and Roeser, H. A., 2001. Revised tectonic boundaries in the Cocos Plate off Costa Rica: Implications for the segmentation of the convergent margin and for plate tectonic models. *J. Geophys. Res.*, 106:19207–19220.
- Bialas, J. and Flueh, E. R., 1999. Ocean bottom seismometers. *Sea Technology*, 40:41–46.
- Bostock, M. G., Hyndman, R. D., Rondenay, S., and Peacock, S. M., 2002. An inverted continental Moho and serpentinization of the forearc mantle. *Nature*, 417:536–538.
- Bowland, C. L., 1993. Depositional history of the western Colombian Basin, Caribbean Sea, revealed by seismic stratigraphy. *Bulletin of Geology Society of America*, 105:1321–1345.
- Brocher, T. M., Parsons, T., Trehu, A. M., Snelson, C. M., and Fisher, M. A., 2003. Seismic evidence for widespread serpentinized forearc upper mantle along the Cascadia margin. *Geology*, 31:267–+.
- Carlson, R. L. and Miller, D. J., 2003. Mantle wedge water contents estimated from seismic velocities in Partially Serpentinized Peridotites. *Geophys. Res. Lett.*, 30:54–1.
- Carr, M., Feigenson, M. D., Patino, L. C., and Walker, J. A., 2003. Volcanism and geochemistry in Central America: Progress and problems. In Eiler, J., editor, *Inside the subduction factory*, pp. 153–179. American Geophysical Union.
- Carr, M. J., Saginor, I., Alvarado, G. E., Bolge, L. L., Lindsay, F. N., Milidakis, K., Turrin, B. D., Feigenson, M. D., and Swisher, C. C., 2007. Element fluxes from the

- volcanic front of Nicaragua and Costa Rica. *Geochemistry Geophysics Geoscience*, 8:1–22.
- Chapple, W. M. and Tullis, T. E., 1977. Evaluation of the forces that drive the plates. *J. Geophys. Res.*, 82:1967–1984.
- Christensen, N. I., 1966. Elasticity of Ultrabasic Rocks. *J. Geophys. Res.*, 71:5921–+.
- Christeson, G. L., McIntosh, K. D., Shipley, T. H., Flueh, E. R., and Goedde, H., 1999. Structure of the Costa Rica convergent margin, offshore Nicoya Peninsula. *J. Geophys. Res.*, 104:25443–25468.
- Colombo, D., Cimini, G. B., and de Franco, R., 1997. Three dimensional velocity structure of the upper mantle beneath Costa Rica from teleseismic tomography study. *Geophys. J. Int.*, 131:189–208.
- DeMets, C., 2001. A new estimate for present-day Cocos-Caribbean plate motion: Implications for slip along the Central American volcanic arc. *Geophys. Res. Lett.*, 28:4043–4046.
- Demets, C., Gordon, R. G., Argus, D. F., and Stein, S., 1994. Effect of recent revisions to the geomagnetic reversal timescale on estimates of current plate motions. *Geophys. Res. Lett.*, 21:2191–+.
- DeShon, H. R., Schwartz, S. Y., Bilek, S. L., Dorman, L. M., Gonzalez, V., Protti, J. M., Flueh, E. R., and Dixon, T. H., 2003. Seismogenic zone structure of the southern Middle America Trench, Costa Rica. *J. Geophys. Res.*, 108:2491–+.
- DeShon, H. R., Schwartz, S. Y., Newman, A. V., Gonzalez, V., Protti, M., Dorman, L. M., Dixon, T. H., Sampson, D. E., and Flueh, E. R., 2006. Seismogenic zone structure beneath the Nicoya Peninsula, Costa Rica, from three-dimensional local earthquake P- and S-wave tomography. *Geophys. J. Int.*, 164:109–124.
- Eberhart-Phillips, D. and Mark Henderson, C., 2004. Including anisotropy in 3-D velocity inversion and application to Marlborough, New Zealand. *Geophys. J. Int.*, 156:237–254.
- Elming, S. and Rasmussen, T., 1997. Results of magnetotelluric and gravimetric measurements in western Nicaragua, Central America. *Geophys. J. Int.*, 128:647–658.
- Fischer, K. M. and Wiens, D. A., 1996. The depth distribution of mantle anisotropy beneath the Tonga subduction zone. *Earth and Planetary Science Letters*, 142:253–260.

- Flueh, E. R. and von Huene, R., 2007. Crustal structure. In Bundschuh, J. and Alvarado, G., editors, *Central America: Geology, Resources and Hazards*, pp. 267–274. Taylor & Francis.
- Forsyth, D. W. and Uyeda, S., 1975. On the relative importance of the driving forces of plate motions. *Geophys. J. Int.*, 43:163–200.
- Fouch, M. J. and Fischer, K. M., 1996. Mantle anisotropy beneath northwest Pacific subduction zones. *J. Geophys. Res.*, 101:15987–16002.
- Fouch, M. J. and Fischer, K. M., 1998. Shear wave anisotropy in the Mariana subduction zone. *Geophys. Res. Lett.*, 25:1221–1224.
- Gardner, T. W. and Verdonck, D. and Pinter, N. M., 1992. Quaternary uplift astride the aseismic Cocos Ridge, Pacific coast, Costa Rica. *GSA Bulletin*, 104:219–232.
- Gräfe, K., 1998. Exhumation and thermal evolution of the Cordillera de Talamanca (Costa Rica): constraints from fission track analysis, ^{40}Ar - ^{39}Ar and ^{87}Rb - ^{87}Sr chronology. PhD thesis, Universität Tübingen, Germany.
- Grevemeyer, I., Ranero, C. R., Flueh, E. R., Klaschen, D., and Bialas, J., 2007. Passive and active seismological study of bending-related faulting and mantle serpentinization at the Middle America trench. *Earth and Planetary Science Letters*, 258:528–542.
- Hacker, B. R., Peacock, S. M., Abers, G. A., and Holloway, S. D., 2003. Subduction factory 2. Are intermediate-depth earthquakes in subducting slabs linked to metamorphic dehydration reactions? *J. Geophys. Res.*, 108:2030–+.
- Hall, C. E., Fischer, K. M., Parmentier, E. M., and Blackman, D. K., 2000. The influence of plate motions on 3D back arc mantle flow and shear wave splitting. *J. Geophys. Res.*, 105:28009–28033.
- Hasegawa, A. and Nakajima, J., 2004. Geophysical constraints on slab subduction and arc magmatism. In *Geophysical Monograph 150*, pp. 81–93. AGU.
- Hauff, F., Hoernle, K., Schmincke, H. U., and Werner, R., 1997. A Mid Cretaceous origin for the Galapagos hotspot: volcanological, petrological and geochemical evidence from Costa Rican oceanic crustal segments. *International Journal of Earth Sciences*, 86:141–155.
- Hearn, T. M., 1996. Anisotropic Pn tomography in the western United States. *J. Geophys. Res.*, 101:8403–8414.

- Heuret, A., Funiciello, F., Faccenna, C., and Lallemand, S., 2007. Plate kinematics, slab shape and back-arc stress: A comparison between laboratory models and current subduction zones. *Earth and Planetary Science Letters*, 256:473–483.
- Heuret, A. and Lallemand, S., 2005. Plate motions, slab dynamics and back-arc deformation. *Phys. Earth and Planet. Inter.*, 149:31–51.
- Hinz, K., von Huene, R., and Ranero, C. R., 1996. Tectonic structure of the convergent Pacific margin offshore Costa Rica from multichannel seismic reflection data. *Tectonics*, 15:54–66.
- Hirahara, K. and Ishikawa, Y., 1984. Travel time inversion for three-dimensional P-wave velocity anisotropy. *J. Phys. Earth*, 32:197–218.
- Hiramatsu, Y., Ando, M., Tsukuda, T., and Ooida, T., 1998. Three-dimensional image of the anisotropic bodies beneath central Honshu, Japan. *Geophys. J. Int.*, 135:801–816.
- Hoernle, K., Abt, D. L., Fischer, K. M., Nichols, H., Hauff, F., Abers, G. A., van den Bogaard, P., Heydolph, K., Alvarado, G., Protti, M., and Strauch, W., 2008. Arc parallel flow in the mantle wedge beneath Costa Rica and Nicaragua. *Nature*, pp. 1–5.
- Hoernle, K. and Hauff, F., 2007. Oceanic igneous complexes in central america. In Bundschuh, J. and Alvarado, G., editors, *Central America: Geology, Resources and Hazards*, pp. 523–548. Taylor & Francis.
- Honda, S. and Saito, M., 2003. Small-scale convection under the back-arc occurring in the low viscosity wedge. *Earth and Planetary Science Letters*, 216:703–715.
- Husen, S., Kissling, E., and Quintero, R., 2002. Tomographic evidence for a subducted seamount beneath the Gulf of Nicoya, Costa Rica: The cause of the 1990 Mw = 7.0 Gulf of Nicoya earthquake. *Geophys. Res. Lett.*, 29:79–1.
- Husen, S., Quintero, R., Kissling, E., and Hacker, B., 2003. Subduction-zone structure and magmatic processes beneath Costa Rica constrained by local earthquake tomography and petrological modelling. *Geophys. J. Int.*, 155:11–32.
- Hyndman, R. D. and Peacock, S. M., 2003. Serpentinization of the forearc mantle. *Earth and Planetary Science Letters*, 212:417–432.
- Hyndman, R. D., Yamano, M., and Oleskevich, D. A., 1997. The seismogenic zone of subduction thrust faults. *The Island Arc*, 6:244–260.
- Ishise, M. and Oda, H., 2005. Three-dimensional structure of P-wave anisotropy beneath the Tohoku district, northeast Japan. *J. Geophys. Res.*, 110:1–16.

- Jung, H. and Karato, S., 2001. Water-induced fabric transitions in olivine. *Science*, 293:1460–1463.
- Kamiya, S. and Kobayashi, Y., 2000. Seismological evidence for the existence of serpentinized wedge mantle. *Geophys. Res. Lett.*, 27:819–+.
- Kissling, E., Ellsworth, W. L., Eberhart-Phillips, D., and Kradolfer, U., 1994. Initial reference models in local earthquake tomography. *J. Geophys. Res.*, 99:19635–19646.
- Kneller, E. A., van Keken, P. E., Karato, S.-I., and Park, J., 2005. B-type olivine fabric in the mantle wedge: Insights from high-resolution non-Newtonian subduction zone models. *Earth and Planetary Science Letters*, 237:781–797.
- Koulakov, I., Bohm, M., Asch, G., Luehr, B.-G., Manzanares, A., Brotopuspito, K. S., Fauzi, P., Purbawinata, M. A., Puspito, N. T., Ratdompurbo, A., Kopp, H., Rabbel, W., and Shevkunova, E., 2007. P and S velocity structure of the crust and the upper mantle beneath central Java from local tomography inversion. *J. Geophys. Res.*, 112:8310–+.
- Koulakov, I. and Sobolev, S. V., 2006. Moho depth and three-dimensional P and S structure of the crust and uppermost mantle in the Eastern Mediterranean and Middle East derived from tomographic inversion of local ISC data. *Geophys. J. Int.*, 164:218–235.
- Kutterolf, S., Freundt, A., Perez, W., Wehrmann, H., and Schmincke, H. U., 2007. Late Pleistocene to Holocene temporal succession and magnitudes of highly-explosive volcanic eruptions in west-central Nicaragua. *Journal of Volcanology and Geothermal Research*, 163:55–82.
- Lefeldt, M., Grevemeyer, I., Ivandic, M., Gossler, J., and Bialas, J., 2008. Centroid depth and mechanism of trench-outer rise earthquakes. *Geophys. J. Int.*, 172:240–251.
- Long, M. D. and Silver, P. G., 2008. The subduction zone flow field from seismic anisotropy: A global view. *Science*, 319:315–318.
- Long, M. D. and van der Hilst, R. D., 2006. Shear wave splitting from local events beneath the Ryukyu arc: Trench-parallel anisotropy in the mantle wedge. *Phys. Earth and Planet. Inter.*, 155:300–312.
- Mann, P., Rogers, R. D., and Gahagan, L., 2007. Overview of plate tectonic history and its unresolved tectonic problems. In Bunddchuh, J. and Alvarado, G., editors, *Central America: Geology, Resources and Hazards*, pp. 267–274. Taylor & Francis.

- Marshall, J. S. and Anderson, R. S., 1995. Quaternary uplift and seismic cycle deformation, Peninsula de Nicoya, Costa Rica. *GSA Bulletin*, 107:463–473.
- McIntosh, K. D., Silver, E. A., Ahmed, I., Berhorst, A., Ranero, C. R., Kelly, R. K., and Flueh, E. R., 2007. The nicaragua convergent margin: seismic reflection of the source of a tsunami earthquake. In Dixon, T. H. and Moore, C., editors, *Seismogenic zone of subduction thrust faults.*, pp. 257–287. Barnes & Noble.
- McKenzie, D., 1979. Finite deformation during fluid flow. *Geophys. J. R. Astron. Soc.*, 58:689–715.
- Mehl, L., Hacker, B. R., Hirth, G., and Kelemen, P. B., 2003. Arc-parallel flow within the mantle wedge: Evidence from the accreted Talkeetna arc, south central Alaska. *J. Geophys. Res.*, 108:2375–+.
- Nakajima, J. and Hasegawa, A., 2004. Shear-wave polarization anisotropy and subduction induced flow in the mantle wedge of northeastern Japan. *Earth and Planetary Science Letters*, 225:365–377.
- Newman, A. V., Schwartz, S. Y., Gonzalez, V., DeShon, H. R., Protti, J. M., and Dorman, L. M., 2002. Along-strike variability in the seismogenic zone below Nicoya Peninsula, Costa Rica. *Geophys. Res. Lett.*, 29:38–1.
- Noll, Jr., P. D., Newsom, H. E., Leeman, W. P., and Ryan, J. G., 1996. The role of hydrothermal fluids in the production of subduction zone magmas: Evidence from siderophile and chalcophile trace elements and boron. *GCA*, 60:587–611.
- Norabuena, E., Dixon, T. H., Schwartz, S., DeShon, H., Newman, A., Protti, M., Gonzalez, V., Dorman, L., Flueh, E. R., Lundgren, P., Pollitz, F., and Sampson, D., 2004. Geodetic and seismic constraints on some seismogenic zone processes in Costa Rica. *J. Geophys. Res.*, 109:11403–+.
- Okada, T., Matsuzawa, T., and Hasegawa, A., 1995. Shear-wave polarization anisotropy beneath the north-eastern part of Honshu, Japan. *Geophys.J.Int*, 123:781–797.
- Oleskevich, D. A., Hyndman, R. D., and Wang, K., 1999. The updip and downdip limits to great subduction earthquakes: Thermal and structural models of Cascadia, south Alaska, SW Japan, and Chile. *J. Geophys. Res.*, 104:14965–14992.
- Ozalaybey, S. and Savage, M. K., 1995. Shear-wave splitting beneath western United States in relation to plate tectonics. *J. Geophys. Res.*, 100:18135–18150.
- Paige, C. C. and Saunders, M. A., 1982. LSQR, An algorithm for sparse linear equations and sparse least squares. *ACM Trans. Math. Software*, Volume 8, p. 43-71, 8:43–71.

- Patino, L. C., Carr, M. J., and Feigenson, M. D., 2000. Local and regional variations in Central American arc lavas controlled by variations in subducted sediment input. *Contributions to Mineralogy and Petrology*, 138:265–283.
- Peacock, S. M. and Hyndman, R. D., 1999. Hydrous minerals in the mantle wedge and the maximum depth of subduction thrust earthquakes. *Geophys. Res. Lett.*, 26:2517–2520.
- Peacock, S. M., Van Keken, P. E., Holloway, S. D., Hacker, B. R., Abers, G. A., and Ferguson, R. L., 2005. Thermal structure of the Costa Rica Nicaragua subduction zone. *Phys. Earth and Planet. Inter.*, 149:187–200.
- Polet, J., Silver, P. G., Beck, S., Wallace, T., Zandt, G., Ruppert, S., Kind, R., and Rudloff, A., 2000. Shear wave anisotropy beneath the Andes from the BANJO, SEDA, and PISCO experiments. *J. Geophys. Res.*, 105:6287–6304.
- Protti, M., Guendel, F., and McNally, K., 1994. The geometry of the Wadati-Benioff zone under southern Central America and its tectonic significance: results from a high-resolution local seismographic network. *Phys. Earth and Planet. Inter.*, 84:271–287.
- Protti, M., Guendel, F., and McNally, K., 1995. Correlation between the age of the subducting Cocos plate and geometry of the Wadati-Benioff zone under Nicaragua and Costa Rica. *Geol. Soc. Am. Spec. Paper*, 295:309–326.
- Protti, M., Schwartz, S. Y., and Zandt, G., 1999. Simultaneous inversion for earthquake location and velocity structure beneath central Costa Rica. *Bull. Seism. Soc. Am.*, 86:19–31.
- Quintero, R. and Kissling, E., 2001. An improved P-wave velocity reference model for Costa Rica. *Geofis. Int.*, 40:3–19.
- Ranero, C. R., Phipps, M. J., McIntosh, K., and Reichert, C., 2003. Bending-related faulting and mantle serpentinitization at the Middle America trench. *Nature*, 425:367–373.
- Ranero, C. R., von Huene, R., Flueh, E., Duarte, M., Baca, D., and McIntosh, K., 2000. A cross section of the convergent Pacific margin of Nicaragua. *Tectonics*, 19:335–357.
- Ribe, N. M., 1992. On the relation between seismic anisotropy and finite strain. *J. Geophys. Res.*, 97:8737–8747.
- Ribe, N. M. and Yu, Y., 1991. A theory for plastic deformation and textural evolution of olivine polycrystals. *J. Geophys. Res.*, 96:8325–8335.

- Rüpke, L. H., Phipps Morgan, J., Hort, M., and Connolly, J. A. D., 2002. Are the regional variations in Central American arc lavas due to differing basaltic versus peridotitic slab sources of fluids? *Geology*, 30:1035–+.
- Russo, R. M. and Silver, P. G., 1994. Trench-Parallel Flow Beneath the Nazca Plate from Seismic Anisotropy. *Science*, 263:1105–1111.
- Sallares, V. and Charvis, P., 2003. Crustal thickness constraints on the geodynamic evolution of the Galapagos Volcanic Province. *Earth and Planetary Science Letters*, 214:545–559.
- Sallares, V., Charvis, P., Flueh, E. R., and Bialas, J., 2005. Seismic structure of the Carnegie ridge and the nature of the Galapagos hotspot. *Geophys. J. Int.*, 161:763–788.
- Sallares, V., Danobeitia, J. J., and Flueh, E. R., 2000. Seismic tomography with local earthquakes in Costa Rica. *Tectonophysics*, 296:61–78.
- Sallares, V., Danobeitia, J. J., and Flueh, E. R., 2001. Litospheric structure of the Costa Rica Isthmus: Effects of subduction zone magmatism on an oceanic plateau. *J. Geophys. Res.*, 106:621–643.
- Savage, M. K., 1999. Seismic anisotropy and mantle deformation: What have we learned from shear wave splitting? *Reviews of Geophysics*, 37:65–106.
- Seno, T., 2005. Variation of downdip limit of the seismogenic zone near the Japanese islands: implications for the serpentinization mechanism of the forearc mantle wedge. *Earth and Planetary Science Letters*, 231:249–262.
- Smith, G. P., Wiens, D. A., Fischer, K. M., Dorman, L. M., Webb, S. C., and Hildebrand, J. A., 2001. A complex pattern of mantle flow in the Lau back arc. *Science*, 292:713–716.
- Stavenhagen, A. U., 1998. Refraktionsseismische Untersuchungen on-und offshore Costa Rica. PhD thesis, Universität zu Kiel, Germany.
- Thurber, C. H., 1993. Local earthquake tomography: velocities and vp/vs theory. In Iyer, H. M. and Hirahara, K., editors, *Seismic Tomography: Theory and Practice*, pp. 563–580. Capman & Hall.
- Turner, H. L., LaFemina, P., Saballos, A., Mattioli, S. G., Jansma, P. E., and Dixon, T., 2007. Kinematics of the Nicaraguan forearc from GPS geodesy. *Geophys. Res. Lett.*, 34:1–5.

- Ulmer, P. and Trommsdorff, V., 1995. Serpentine Stability to Mantle Depths and Subduction-Related Magmatism. *Science*, 268:858–861.
- Um, J. and Thurber, C., 1987. A fast algorithm for two point seismic ray tracing. *Bull. Seism. Soc. Am.*, 77:972–986.
- Van der Sluis, A. and van der Vorst, H. A., 1987. Numerical solution of large, sparse linear algebraic systems arising from tomographic problems. In Nolet, editor, *Seismic Tomography*, pp. 49–83. D.Reidel.
- van Keken, P. E., 2003. The structure and dynamics of the mantle wedge. *Earth and Planetary Science Letters*, 215:323–338.
- von Huene, R., Ranero, C. R., Weinrebe, W., and Hinz, K., 2000. Quaternary convergent margin tectonics of Costa Rica, segmentation of the Cocos Plate, and central American volcanism. *Tectonics*, 19:314–334.
- von Huene, R. e. a., 1995. Morphotectonics of the Pacific convergent margin of Costa Rica. *Geol. Soc. Am. Spec. Paper*, 295:291–307.
- Walther, C. and Flueh, E. R., 2002. Remnant of the ancient Farallon Plate breakup: A low-velocity body in the lower oceanic crust off Nicoya Peninsula, Costa Rica - evidence from wide-angle seismics. *Geophys. Res. Lett.*, 29:45–1.
- Walther, C. H. E., 2003. The crustal structure of the Cocos ridge off Costa Rica. *J. Geophys. Res.*, 108:2136–+.
- Walther, C. H. E., Flueh, E. R., Ranero, C. R., von Huene, R., and Strauch, W., 2000. Crustal structure across the Pacific margin of Nicaragua:evidence for ophiolitic basement and a shallow mantle sliver. *Geophys. J. Int.*, 141:759–777.
- Werner, R., Hoernle, K., van den Bogaard, P., Ranero, C., von Huene, R., and Korich, D., 1999. Drowned 14-m.y.-old Galapagos archipelago off the coast of Costa Rica: Implications for tectonic and evolutionary models. *Geology*, 27:499–+.
- Wiemer, S.and Tytgat, G., Wyss, M., and Duenkel, U., 1999. The crustal structure of the Cocos ridge off Costa Rica. *Bull. Seismol. Soc. Am.*, 89:1313–1322.
- Wilson, D. S., Teagle, D. A., and Acton, G. D., 2003. First Results From Hole 1256D - a New Ocean-Crust Reference Hole Drilled in Fast-Spread Crust During ODP Leg 206. *AGU Fall Meeting Abstracts*, pp. A2+.
- Yang, X., Fischer, K. M., and Abers, G. A., 1995. Seismic anisotropy beneath the Shumagin Island segment of the Aleutian-Alaska subduction zone. *J. Geophys. Res.*, 100:18615–18677.

- Yao, Z. S., Quintero, R., and Roberts, R. G., 1999. Tomographic imaging of P- and S-wave velocity structure beneath Costa Rica. *J. of Seism.*, 3:177–190.
- Ye, S., Bialas, J., Flueh, E. R., Stavenhagen, A., von Huene, R., Leandro, G., and Hinz, K., 1996. Crustal structure of the Middle American Trench off Costa Rica from wide-angle seismic data. *Tectonics*, 15:1006–1021.
- Zandt, G., 2002. The slippery slope. *Nature*, 417:497–498.
- Zhang, H. and Kayal, J. R., 2000. Impact of seismic tomography. *Science*, 79:1208–1214.
- Zhang, H., Thurber, C. H., Shelly, D., Ide, S., Beroza, G. C., and Hasegawa, A., 2004. High-resolution subducting-slab structure beneath northern Honshu, Japan, revealed by double-difference tomography. *Geology*, 32:361–+.

List of Figures

1.1	Material transport and transformation in subduction zones.	10
1.2	Seismological stations in Central America.	12
2.1	Tectonic settings of Costa Rica and Nicaragua.	14
3.1	Block scheme of the LOTOS algorithm.	22
3.2	Sketch for definition of the anisotropic model.	24
3.3	Block scheme of the ANITA algorithm.	25
4.1	Example of a record section.	31
4.2	Example recording of an event at a land station.	32
4.3	Example recording of an event at a sea station.	32
4.4	Distribution of seismicity.	33
4.5	Statistical approach for calculating the standard deviation of the events.	34
4.6	Inversion of odd, even number of events and all data set.	35
4.7	A checkerboard sensitivity test.	36
4.8	Simon Bolivar test.	37
4.9	Resolution of realistic velocity anomalies.	38
4.10	Seismicity distribution after 3D inversion.	39
4.11	Cross-sections of P-wave velocity perturbations.	41
4.12	Cross-sections of absolute P-wave velocities.	43
4.13	A tentative schematic tectonic interpretation based on the seismic distribution.	44
4.14	Flying carpet showing the lateral structural changes.	47

4.15	Cross-sections through V_p/V_s ratios.	48
4.16	Horizontal depth sections of V_p perturbations and V_p/V_s ratios.	49
5.1	Example of a record section.	53
5.2	Example recording of an event at a land station.	54
5.3	Example recording of an event at a sea station	54
5.4	Distribution of seismicity.	55
5.5	Inversion of odd, even number of events and all data set.	57
5.6	A checkerboard sensitivity test.	58
5.7	Synthetic test to check the vertical resolution with real anomalies.	59
5.8	Distribution of the events used for Local Earthquake Tomography.	60
5.9	Cross-sections through V_p perturbations.	62
5.10	Cross-sections through absolute V_p/V_s ratios.	63
5.11	Horizontal depth sections for V_p perturbations and absolute V_p/V_s ratios.	64
5.12	Schematic interpretation of the proposed transition.	67
6.1	Pole figures of crystallographic orientation of deformed olivine aggregates.	70
6.2	Schematic diagram of 2D and 3D flow fields in the mantle wedge.	71
6.3	Sketch model showing regions for B-type fabric.	72
6.4	A fabric diagram for olivine on a stress-water content plane at higher temperature conditions.	72
6.5	Horizontal anomaly test for central Costa Rica.	75
6.6	Horizontal anomaly test for S Nicaragua/N Costa Rica.	76
6.7	Checkerboard test for central Costa Rica.	77
6.8	Checkerboard test for S Nicaragua/N Costa Rica.	78
6.9	Test with different grid and smoothing parameters for central Costa Rica.	79
6.10	Test with different grid and smoothing parameters for S Nicaragua/N Costa Rica.	80
6.11	Anisotropy in central Costa Rica.	82
6.12	Anisotropy in S Nicaragua/N Costa Rica.	83

6.13 Comparison of the anisotropy between S Nicaragua/N Costa Rica and
central Costa Rica. 86

List of Tables

4.1	Background model of V_p and V_s applied in the tomographic inversion. . .	33
4.2	Reduction of travel time residuals during 5 iterations of inversion procedure.	39
5.1	Background model of V_p and V_s applied in the tomographic inversion. . .	55
5.2	Reduction of travel time residuals during 5 iterations of inversion procedure.	59
6.1	Parameters of horizontal synthetic models	74
6.2	Parameters of checkerboard synthetic models.	74
6.3	RMS of travel time residuals and reductions for central Costa Rica. . . .	81
6.4	RMS of travel time residuals and reductions for S Nicaragua/N Costa Rica.	84
A.1	List of QUEPOS stations	107
A.2	List of JACO stations	109
A.3	List of RSN stations	111
A.4	List of TOMO stations	112

Appendix A

Station Lists

A.1 QUEPOS Station List

Table A.1: List of QUEPOS stations

Station	Latitude	Longitude	Altitude
con	-84.05334	9.585333	1350
cts	-84.10333	9.506000	66
dom	-83.85917	9.265667	44
gua	-83.83867	9.341166	168
man	-84.14283	9.381500	41
mat	-83.93867	9.334167	156
nar	-83.94133	9.588667	1622
pro	-83.86083	9.556167	1828
rse	-84.21716	9.577333	156
sav	-83.97617	9.458000	193
scy	-84.12867	9.618167	1471
sva	-83.84666	9.441833	736
sbl	-84.05933	9.430500	65
vue	-84.27950	9.531167	34
301	-84.50050	9.259334	-311
302	-84.35800	9.261833	-326
303	-84.38583	9.139334	-656
304	-84.41350	9.030167	-1156
305s	-84.50667	9.083500	-1038
306	-84.71650	9.117666	-1157

Continued on next page

Table A.1 – continued from previous page

Station	Latitude	Longitude	Altitude (m)
307s	-84.83266	8.833834	-3488
308	-84.54633	8.653334	-2167
309s	-84.37984	8.580000	-2840
310	-84.38600	8.763500	-1849
311	-84.51000	8.771000	-2550
312	-84.58017	8.880167	-2613
313	-84.47150	8.884167	-1993
314	-84.46400	8.961000	-1617
315	-84.34333	8.875834	-1312
316s	-84.31734	8.964666	-909
317	-84.28000	9.060000	-519
318	-84.25450	9.175500	-354
319	-84.19566	9.052667	-283
320	-84.18150	9.001333	-220
321	-84.20333	8.894834	-284
322	-84.26000	8.790167	-796
323	-84.16483	8.795333	-206

A.2 JACO Station List

Table A.2: List of JACO stations

Station	Latitude	Longitude	Altitude
agc	-84.35000	9.634334	363
aph	-84.58800	9.601334	205
bij	-84.57950	9.719334	595
cal	-84.67067	9.661000	89
eso	-84.50833	9.526500	46
int	-84.60883	9.814667	125
pin	-84.39783	9.670500	363
que	-84.16217	9.426333	740
rse	-84.21716	9.577333	158
sga	-84.49800	9.693666	375
sni	-84.49150	9.606334	160
tiv	-84.70500	9.882167	70
tuf	-84.38400	9.754167	904
tur	-84.46684	9.811500	911
vma	-84.42733	9.598166	234
sbl	-84.05933	9.430500	560
vue	-84.27950	9.531167	340
139	-84.55850	9.217000	-3790
140	-84.63316	9.167000	-939
141	-84.68317	9.216333	-351
193	-85.10100	9.333167	-1880
194	-84.87500	9.467000	-560
195	-84.75000	9.466666	-324
196	-84.75100	9.357833	-413
197s	-84.88300	9.333333	-1745
198	-84.73333	9.249666	-291
199	-84.78284	9.199000	-734
200	-84.82667	9.157000	-824
201s	-84.93433	9.165500	-2080
202	-84.93400	9.032000	-2237
203	-85.08334	8.966166	-3561
204	-84.83334	8.833333	-3474
205	-84.83334	9.000000	-2210

Continued on next page

Table A.2 – continued from previous page

Station	Latitude	Longitude	Altitude (m)
206s	-84.71684	9.033334	-1726
207	-84.71550	9.115334	-1159
208	-84.56983	9.088333	-1155
209	-84.65234	9.037333	-1615
210	-84.63184	8.993000	-1202
211	-84.57433	9.016666	-1411
212	-84.60217	9.038333	-1326

A.3 RSN Station List

Table A.3: List of RSN stations

Station	Latitude °	Longitude °	Altitude (m)
ACR	-83.16800	8.653833	471
BAR1	-83.30700	9.232000	530
BARC	-83.33450	9.166000	378
BUS	-83.75833	9.555333	3487
CGA2	-84.46550	10.01617	1200
CRZC	-85.59666	10.95333	325
ICR	-83.83117	9.980000	3302
JCR	-85.11183	9.849833	575
LCH0	-84.69683	11.07417	54
LCR2	-84.00300	9.742167	1730
PRS1	-84.36400	9.879500	1120
QCR	-84.16217	9.426333	74
SJS	-84.05417	9.939167	1196
TRTC	-83.71350	10.57533	105
URSC	-83.77817	9.835000	1500
VPS2	-84.23534	10.19017	2570
MARE	-83.70467	8.687333	60
TIG2	-83.29700	9.029000	763
OCM	-83.95734	9.889667	1595
LAR	-84.02350	9.705167	2107
PALO	-83.82034	9.785000	1440
IRZ2	-83.89750	9.968833	2950

A.4 TOMO Station List

Table A.4: List of TOMO stations

Station	Latitude	Longitude	Altitude
MES	-85.19633	10.74217	631
GPS1	-85.34917	10.77283	800
GPS2	-85.35133	10.75433	640
GPS3	-85.36517	10.75367	580
GB1A	-85.39850	10.81867	740
BUEV	-85.40700	10.79817	720
GBS2	-85.45250	10.83583	400
GBS3	-85.45550	10.78183	300
NYA7	-85.68217	10.93783	100
NYA9	-85.36667	10.53333	100
NY11	-85.72533	10.49983	150
NY12	-85.79750	10.30200	50
NY13	-85.75667	10.10033	50
NY14	-85.53384	10.64483	100
NY17	-85.61800	10.83867	300
ny08	-85.35500	11.00800	361
ny10	-85.55600	11.07400	330
ny15	-85.59800	10.43700	0
ny16	-85.71400	10.36100	0
nc01	-85.50800	11.18700	30
nc02	-85.51000	11.48200	154
nc03	-85.67700	11.28900	15
nc04	-85.62500	11.56500	200
nc05	-85.71750	11.11617	37
nc06	-85.80100	11.16000	60
nc08	-85.81500	11.48200	60
nc09	-85.87900	11.28300	90
nc10	-85.87100	11.66800	0
nc11	-85.92500	11.43800	130
nc12	-86.01000	11.38900	30
nc13	-86.00500	11.72000	0
nc15	-86.12100	11.48000	10
nc16	-86.10400	11.69700	210

Continued on next page

Table A.4 – continued from previous page

Station	Latitude	Longitude	Altitude (m)
nc18	-86.19800	11.73600	80
nc19	-86.35800	11.65300	0
nc20	-86.35900	11.76200	127
o095	-86.80900	11.14000	-188
o096	-86.67900	10.92900	-405
o097	-86.90000	10.82900	-2344
o098	-86.68500	10.70900	-1309
o099	-86.48300	10.76000	-209
o100	-86.18100	10.78900	-193
o101	-86.26000	10.57000	-255
o102	-86.47000	10.57000	-924
o104	-86.90100	10.49900	-4919
o106	-86.48100	10.20900	-3435
o107	-86.48100	10.38900	-2175
o108	-86.26000	10.38900	-904
o109	-86.25900	10.21000	-1668
o110	-86.07900	10.27600	-212
o111	-86.93000	10.12000	-248
o113	-85.95000	9.821000	-1762
o114	-85.82000	9.940000	-316

Aysun Nilay Dinc

- Personal** Nationality: Turkish
Date of Birth: 28 - 07 - 1978
Gender: Female
- Education**
- PhD (2005 – 2008), Department of Geophysics, Institute of Earthsciences, Christian-Albrechts University, Otto-Hahn-Platz 1, 24103, Kiel, Germany.
 - PhD (2003 – 2005), **GPA: 3.88/4.0**, Istanbul Technical University, Department of Geophysics, Maslak 34390, Istanbul, Turkey.
 - MSc in Geophysics (2001 – 2003), **GPA:3.72/4**, Istanbul Technical University, Department of Geophysics, Maslak 80626, Istanbul, Turkey. (Thesis: Determination of 3-D P-wave velocity structure beneath Sultandağı region by local earthquake tomography. Advisor: Abdullah Karaman)
 - BSc in Geophysics with a honor (1997 – 2001), **GPA:3.49/4**, University of Istanbul, Department of Geophysics, Avcilar 34850, Istanbul, Turkey. (Thesis: Evaluation of seismic refraction data of Gebze, Kocaeli region. Advisor: Ali Pinar)
 - Kabatas High School, 1993 - 1997, **GPA:4/5**, Ortakoy 80840, Istanbul, Turkey.
- Fields of Special Competence**
- Matlab Programming
 - Inversion of Geophysical Data
 - Tomography
 - Numerical Modelling
 - Geophysical Data Acquisition and Processing
 - Signal Processing
 - Hydrogeology
 - Seismology
- Language**
- Advance Level of English
 - Intermediate Level of German
- Work Experiences**
- Researcher, SFB574 project, Department of Geophysics, Faculty of Earth Sciences, Christian-Albrechts University, Otto-Hahn-Platz 1, 24118, Kiel, Germany. **August 2005 – present.**
 - Engineer, MOE Geophysical Engineering Co., Caferaga mah. Sarraf Ali sok. Saracoglu ishani No:36/21, Kadikoy 81300, Istanbul, Turkey. **2000 – 2001.**
 - Student Project Assistant, TUBITAK (The Scientific And Technical Research Council of Turkey), Marmara Research Center, Institute of Earth Sciences, **1999 - 2001.**
 - Traniee, Kandilli Observatory And Earthquake Research Institute, Department of Seismology, **August 1999.**
- Onshore-Offshore Field Experiences**
- Short period and broadband seismometer installation in Costa Rica and Nicaragua (01.11.2005-21.11.2005).
 - Seismology on M66-4a cruise offshore Nicaragua (21.11.2005 - 12.12.2005).
 - Seismology on Salvador cruise in Marmara Sea, Turkey (27.06.2006-30.06.2006).
 - Seismology on Salvador cruise in Marmara Sea, Turkey (29.10.2006-01.11.2006).
- Computer Skills**
- Operating Systems: Windows, Linux, Unix
 - Microsoft Office Packages
 - Matlab
 - Programming Languages: Fortran, Shell scripting
 - General purpose plotting packages: GMT (Generic Mapping Tool), Coral Draw, Surfer, Grapher, Autocad, Photoshop.
 - Seismology packages: SAC, Seisan, Simul2000, TOMO2GMT, Winsism.
 - Fluid Flow Modelling Packages: VS2DI package, Boss GMS (Ground water modelling system), Basin2.

Ich erkläre hiermit an Eides Statt, dass ich die vorliegende Arbeit selbständig und ohne Benutzung anderer als der angegebenen Hilfsmittel angefertigt habe. Die aus fremden Quellen direkt übernommenen Gedanken sind kenntlich gemacht.

Diese Arbeit wurde in gleicher oder ähnlicher Form keiner anderen Prüfungsbehörde vorgelegt oder veröffentlicht.

Aysun Nilay Dinc